Cosmogenic nuclide dating of the sediments of Bulmer Cavern: implications for the uplift history of southern Northwest Nelson, South Island New Zealand

Gavin Holden

A thesis submitted to Victoria University of Wellington in partial fulfilment of the requirements for the degree of Master of Science in Geology

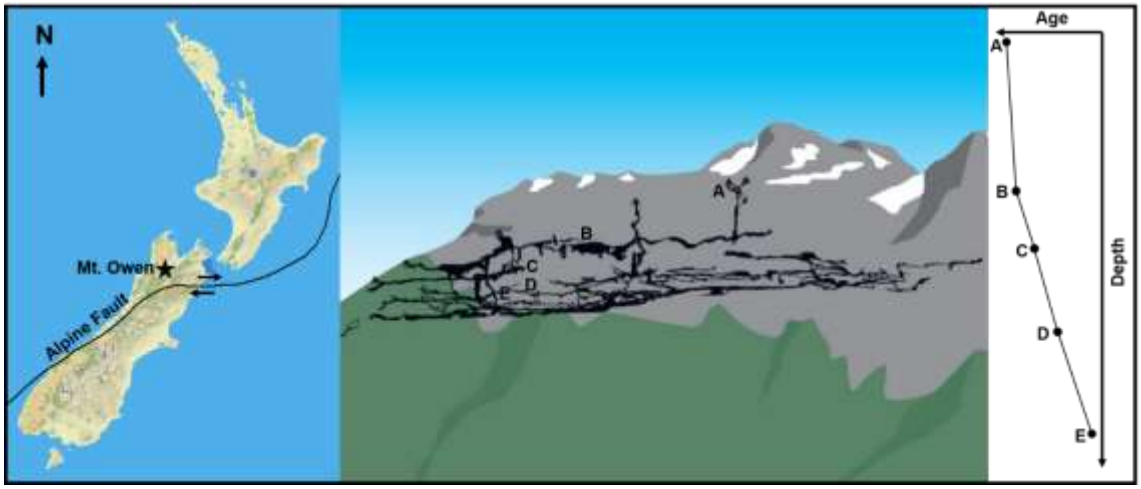

School of Geography, Environment and Earth Sciences

Victoria University of Wellington

November 2018

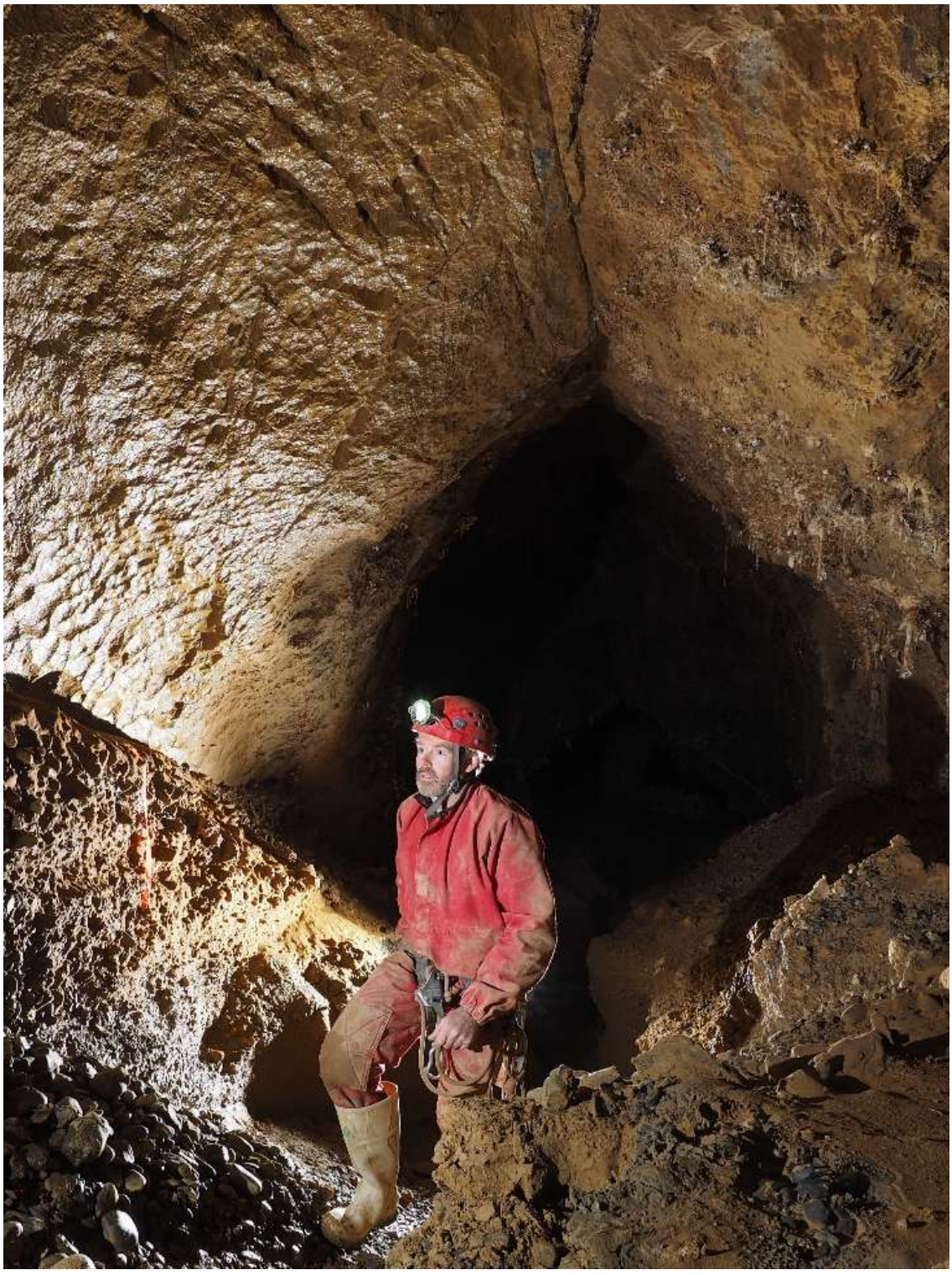

Frontispiece: A caver in the Wildcat Series, lower levels of Bulmer cavern.

Abstract

The landscape of Northwest Nelson shows evidence of significant tectonic activity since the inception of the Austro-Pacific plate boundary in the Eocene. Evidence of subsidence followed by rapid uplift from the Eocene to the late Miocene is preserved in the sedimentary basins of Northwest Nelson. However, the effects of erosion mean there is very little evidence of post-Miocene tectonic activity preserved in the Northwest Nelson area. This is a period of particular interest, because it coincides with the onset of rapid uplift along the Alpine Fault, which is located to the south, and the very sparse published data for this period suggest very low uplift rates compared to other areas close to the Alpine Fault.

Cosmogenic nuclide burial dating of sediments preserved in Bulmer Cavern, indicate an uplift rate of 0.13mm/a from the mid-Pliocene to the start of the Pleistocene and 0.067mm/a since the start of the Pleistocene.

The Pleistocene uplift rate is similar to other published uplift rates for this period from the northern parts of Northwest Nelson, suggesting that the whole of Northwest Nelson has experienced relative tectonic stability compared to other areas close to the Alpine Fault during this period. The mid-Pliocene uplift rate is possibly the first precisely constrained uplift rate in the area for this period, and suggests that there has been a progressive decrease in uplift rates from much higher rates in the late Miocene.

Acknowledgements

First and foremost, I would like to say a big thank you to my supervisor, Kevin Norton for making available the opportunity to pursue this topic, and for all of the assistance with the lab work and data processing.

I would also like to say a big thank you to the SGEES technical staff for all of their help and assistance with this project. In particular, I would like to acknowledge Bruce Charlier and Luisa Ashworth for their assistance with the ICP-MS analysis, Ian Schipper for his assistance with the microprobe analysis, and Jane Chewings for all of her assistance with various aspects of this project. Thanks also goes to Dianne Seward for making the theromchronology data available.

I would also like to acknowledge the generous support of the team at PRIME Lab for both funding and carrying out the AMS analysis.

Special thanks also goes to Lindsay Main and Marcus Thomas for making the maps of Bulmer Cavern available, and for their assistance with choosing the sampling sites and for their help and feedback in the writing of this thesis.

I would also like to acknowledge Lindsay Main, Alice Shanks and Mike Allen for organising the expeditions to Mt Owen, and the various expedition members who assisted with the collection of the samples.

I also wish to acknowledge the Department of Conservation for granting the permits needed to collect the samples.

Finally, I would like to acknowledge my parents for all of their help and support during this project.

Table of contents

List of figures

List of tables

Research Aims

The existing knowledge of the tectonic uplift history of the Northwest Nelson area is characterised by small, widely dispersed datasets that are located in areas distal to the Alpine Fault. Locating a site that can provide new data that is proximal to the Alpine Fault may make a significant contribution to the understanding of the tectonic uplift history of the Northwest Nelson area.

The primary aim of this project is to extend the knowledge of the tectonic uplift history of the Northwest Nelson area since the Pliocene by applying cosmogenic nuclide burial dating to sediments preserved in the passages of Bulmer Cavern, which is a multi-level cave system located approximately 30 km north of the Alpine Fault.

I propose to achieve this by identifying sites at different levels of Bulmer Cavern that contain sediments that can be reliably dated using cosmogenic aluminium-26 (^{26}Al)/beryllium-10 (^{10}Be) burial dating, and to use these dates to reconstruct the rate of lowering of hydrologic base level by stream incision and hence tectonic uplift in the area. This project may show when uplift began and whether uplift rates in the Northwest Nelson area have been constant, or if there has been spatial or temporal variation in uplift since the inception of the Austro-Pacific plate boundary.

A secondary aim of this project is to collect data which could be used to extend the knowledge of the paleoclimate history, or the evolution of the landscape of Northwest Nelson during the time period covered by the life of Bulmer Cavern.

I propose to do this by collecting information from within the cave system that could be used to infer the paleohydrology of Bulmer Cavern, and to recover material from the sediments in Bulmer Cavern that can be used as paleoenvironmental proxies.

These data may be a significant addition to the knowledge of the climate and landscape history of the Northwest Nelson area, especially for the pre and early Quaternary period. This period is of particular interest because it was the last time in the Earth's history when atmospheric CO_2 levels were similar to the present.

Chapter 1: Introduction to cosmogenic nuclides and their application to exposure and burial dating

1.1 Production of terrestrial cosmogenic nuclides

Primary cosmic rays are charged particles, mainly protons (~87%) and alpha particles (~12%) that can be sourced from the Sun (solar cosmic rays) or from supernovae (galactic cosmic rays). Solar cosmic rays have relatively low energies (typically 1-50MeV) and galactic cosmic rays have relatively high energies in the order of 0.1-100GeV (Gosse & Phillips, 2001; Cerling & Craig, 1994b). Primary cosmic rays can interact with atoms in the Earth's upper atmosphere and in surface materials to produce terrestrial cosmogenic nuclides.

When a primary cosmic ray with sufficient energy strikes an atom in the upper atmosphere the atom spalls, releasing a cascade of secondary particles which can include a cosmogenic daughter nuclide, alpha particles, low and high energy protons and neutrons, pions and gamma radiation (figure 1.1). The pions decay into muons, which can reach the Earth's surface. If the incoming primary cosmic ray has sufficient energy, some of the protons and neutrons released in the primary spallation will have enough energy to trigger further spallation reactions, and they are called secondary cosmic rays. Solar cosmic rays generally only have enough energy to trigger 1 primary spallation, whereas the primary spallations produced by galactic cosmic rays can produce secondary cosmic rays with enough energy to trigger multiple secondary spallation reactions. This chain of secondary spallation reactions allows a small number of high energy neutrons to reach the Earth's surface (Gosse & Phillips, 2001). Because solar cosmic rays cannot produce a chain of secondary spallation reactions, they do not contribute to the neutron flux at the Earth's surface.

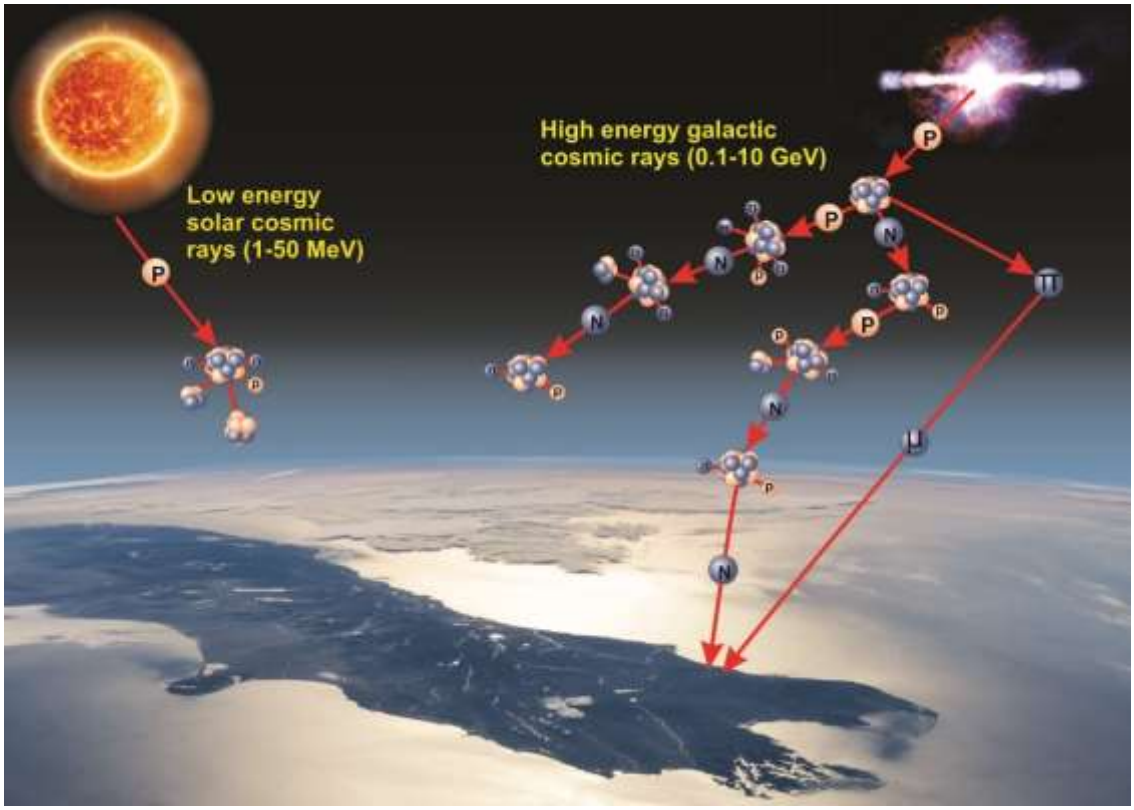

Figure 1.1. How primary cosmic rays interact with the atmosphere to produce secondary cosmic rays at the Earth's surface. Adapted from Dunai, (2010)

Cosmogenic nuclides that are produced in the atmosphere are called meteoric terrestrial cosmogenic nuclides, and they are produced by the spallation of nitrogen and oxygen to produce helium-3 (^{3}He), ^{10}Be and carbon-14 (^{14}C). Cosmogenic nuclides that are produced in minerals that are at, or near the Earth's surface are called in-situ terrestrial cosmogenic nuclides. They are produced by neutron spallation or particle capture reactions in minerals such as quartz, feldspars, pyroxenes, olivine, calcite and garnet. In-situ cosmogenic nuclides can be stable (^{3}He, ^{21}Ne) or radioactive. The radioactive isotopes most commonly used for cosmogenic nuclide dating are ^{14}C, chlorine-36 (^{36}Cl), ^{26}Al, and ^{10}Be, with half-lives ranging from 5.7ka to 1.3Ma (Gosse & Phillips, 2001). A more recent addition to the list of isotopes that can be used for cosmogenic nuclide dating is manganese-53 (^{53}Mn), with a half-life of 3.7Ma (Dunai, 2010). Most in-situ cosmogenic nuclides are produced from secondary cosmic rays that are derived from galactic primary cosmic rays because solar primary cosmic rays do not have sufficient energy to produce secondary cosmic rays that can reach the Earth's surface (Masarik & Reedy, 1995).

Secondary cosmic ray flux, and hence production rates of in-situ cosmogenic nuclides at the Earth's surface is ultimately controlled by the flux of primary cosmic rays at the top of the Earth's atmosphere. Because the Earth is considered to be evenly irradiated with primary cosmic radiation (Leya et al, 2000), the interaction of primary cosmic rays with the Earth's magnetic field is the first order control on secondary cosmic ray flux and distribution. This interaction is a function of the incident angle of the incoming radiation with respect to the Earth's magnetic field and a property of the incoming radiation called rigidity, which describes the resistance of cosmic rays to deflection by a magnetic field. The rigidity of the incoming radiation is a function of the energy of the incoming radiation where higher energy rays are less likely to be deflected by a magnetic field compared to lower energy rays (figure 1.2).

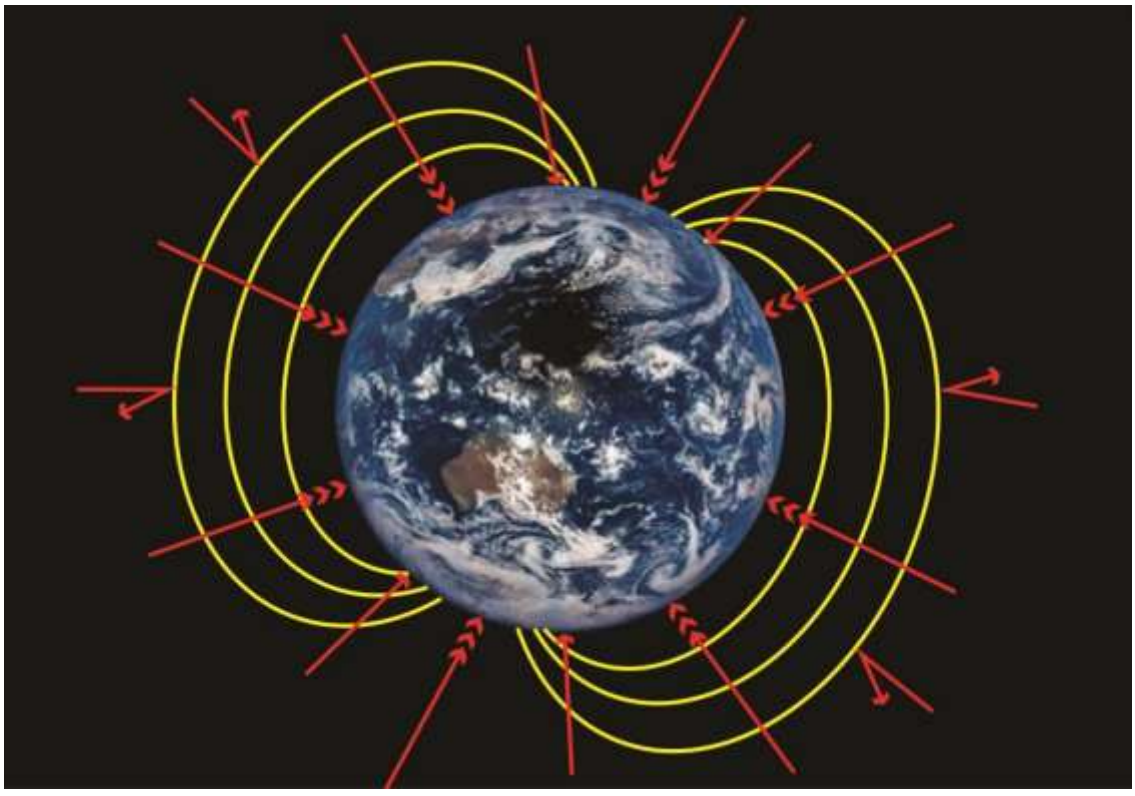

Figure1.2. How the Earth's magnetic field affects cosmic ray flux into the atmosphere. Low energy cosmic rays (single head arrows) intersect the earth's magnetic field at high angles close to the equator and are deflected whereas high energy cosmic rays (triple head arrows) can penetrate into the atmosphere. At high latitudes, low energy cosmic rays can penetrate the earth's magnetic field, resulting in increased cosmic ray flux at high latitudes compared to at the equator.

This results in a meridional gradient in secondary cosmic ray flux at the Earth's surface with higher fluxes at high latitudes and lower fluxes at low latitudes (Figure 1.3). The first order effects of the Earth's magnetic field on primary cosmic ray flux are

modulated by long term (10^3-10^5 year) variations in the Earth's magnetic field. Short term (10^1-10^2 year) changes in solar activity can also influence primary cosmic ray flux through their influence on the Earth's magnetic field. However the effects are only significant over geologically short (<10^3 year) timescales (Cerling & Craig, 1994b; Gosse & Phillips, 2001; Bierman, 1994).

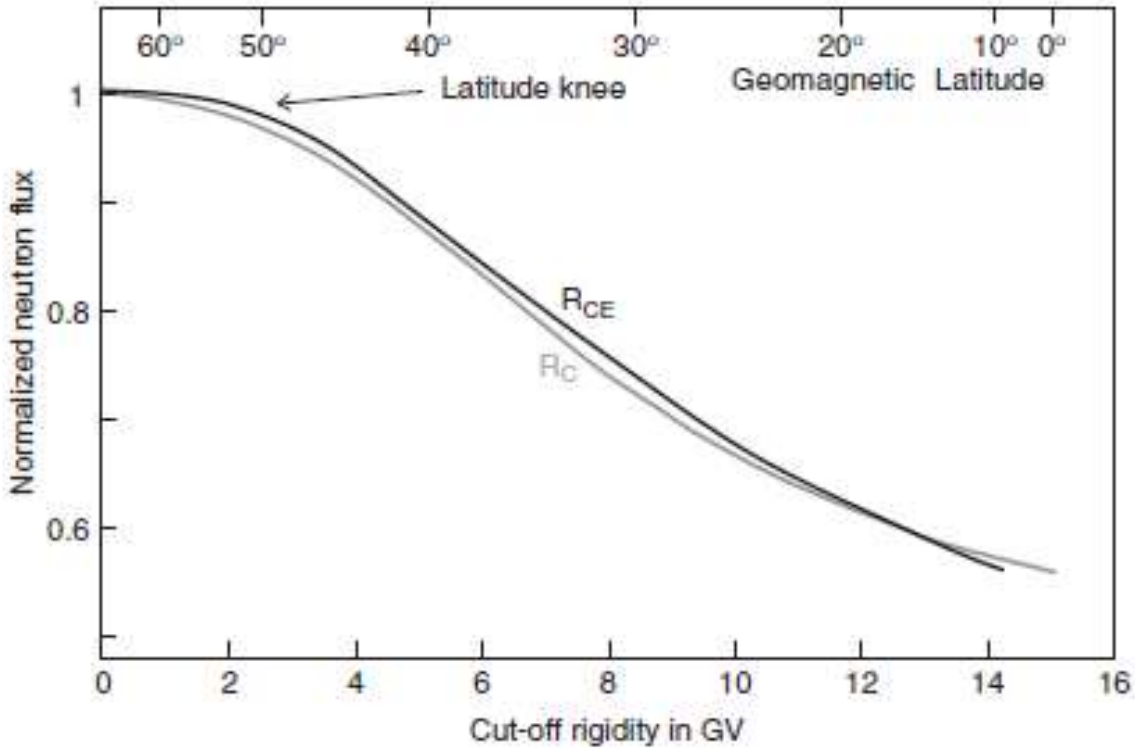

Figure 1.3. The effect of geomagnetic latitude on the ability of primary cosmic rays to penetrate the Earth's atmosphere. The curves R_c and R_{ce} show the effect of increasing cutoff rigidity, which is a function of latitude on neutron flux at sea level. Cutoff rigidity refers to the minimum rigidity required for a primary cosmic ray to penetrate the Earth's atmosphere at a particular latitude. (Dunai, 2010)

Secondary cosmic ray flux at the Earth's surface is also related to the distance between the Earth's surface and the top of the atmosphere, where secondary cosmic ray flux decreases exponentially with increasing atmospheric depth. This means that elevation exerts a second order control on secondary cosmic ray flux at that site, where sites at higher elevation receive higher fluxes than sites at lower elevation. Global-scale features of atmospheric circulation such as stationary high and low pressure systems can locally affect the distance between the Earth's surface and the top of the atmosphere (Staiger et al, 2007; Dunai, 2010).

Secondary cosmic ray flux is also related to the energy of the incoming primary cosmic rays. The attenuation path length of a cosmic ray flux is the thickness of the medium

that it is travelling through that is required to reduce the intensity of that flux by a factor of 1/e, and it varies in proportion to the energy of the cosmic ray flux. Because only high energy primary cosmic rays can penetrate the Earth's magnetic field at low latitudes, secondary cosmic rays produced at low latitudes have higher energies and hence longer attenuation path lengths than secondary cosmic rays produced at high latitudes. This means that secondary cosmic rays produced at low latitudes have more energy when they reach the Earth's surface than secondary cosmic rays produced at high latitudes. Therefore latitude has a second order control on the efficiency and hence rate of production of in-situ cosmogenic nuclides, where production is more efficient at low latitudes compared to high latitudes (Gosse & Phillips, 2001).

Other factors that can influence secondary cosmic ray flux at the Earth's surface include shielding of a particular site from a full view of the horizon by surrounding topography, hillslope aspect or small-scale local rock formations (Gosse et al, 1995; Dunne et al, 1999). This means that local topography has a second order control on secondary cosmic ray flux at a point on the Earth's surface (figure 1.4).

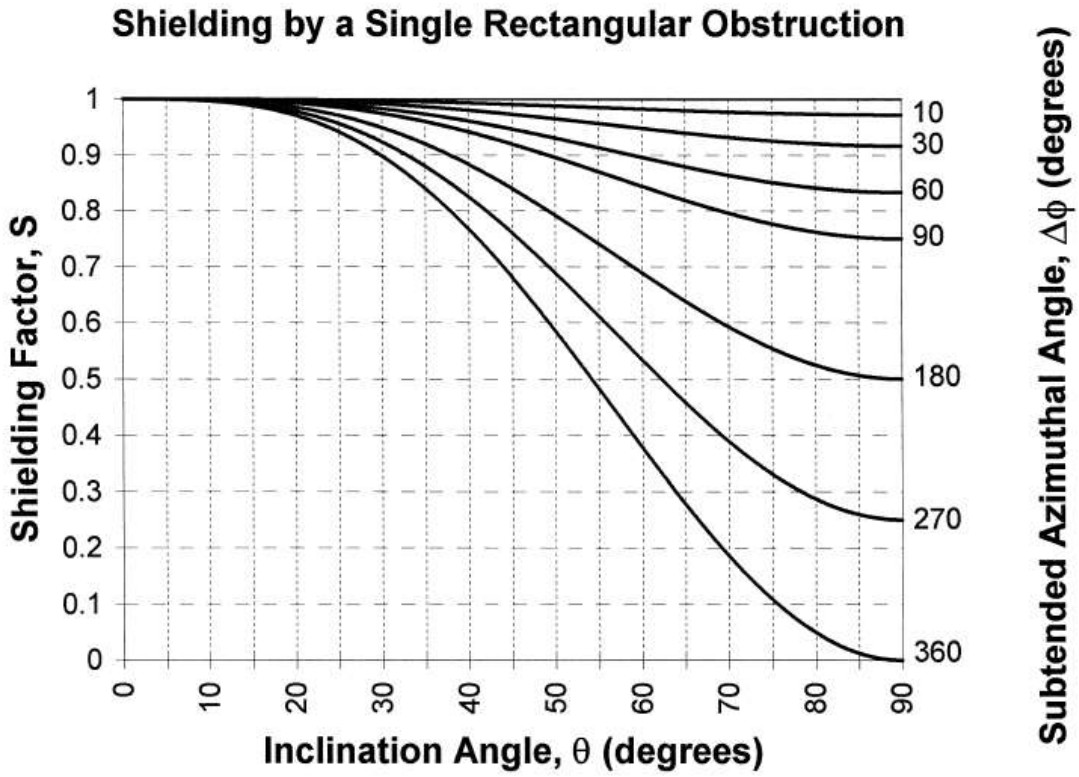

Figure 1.4. An example of the effect of topographic shielding on secondary cosmic ray flux and hence cosmogenic nuclide production. Inclination angle refers to the angle between the site and the horizon relative to horizontal. (Dunne et al, 1999)

Shielding of the Earth's surface from secondary cosmic rays can also be caused by seasonal to semi-permanent changes in snow, regolith or vegetation cover (Darvill, 2013). The amount of shielding is related to the depth and density of the covering material and the amount of time that the covering material is present. Figure 1.5 shows the effect of changes in the duration and density of snow cover on secondary cosmic ray flux at the Earth's surface.

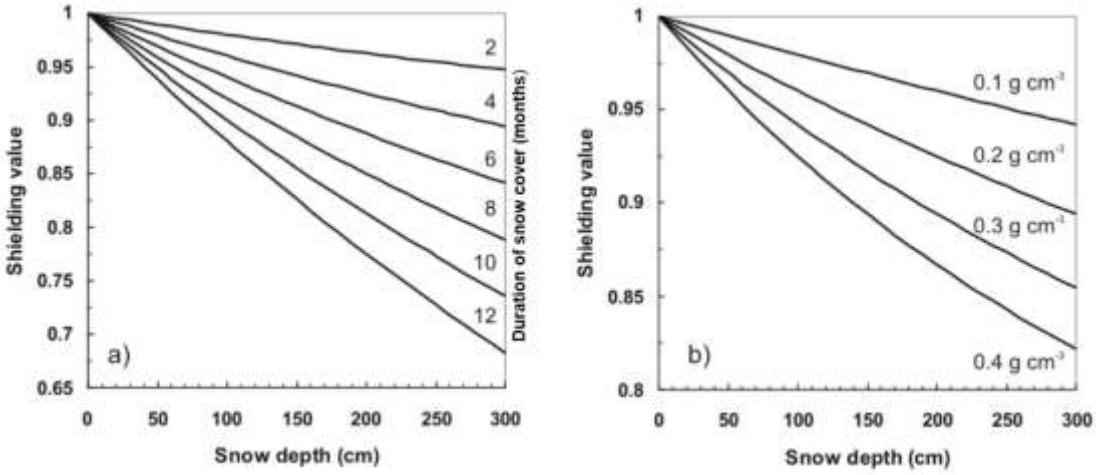

Figure 1.5. An example of the effect of snow cover on secondary cosmic ray flux and hence cosmogenic nuclide production. 1.5a shows the effect of duration of snow cover of constant density on production rates. 1.5b shows the effect of changes in density of snow cover on production rates (Norton, 2008)

1.2 In-situ production of cosmogenic ^{10}Be and ^{26}Al

About 50% of the secondary cosmic rays that reach the Earth's surface are high energy neutrons. If they have sufficient energy (>~10 MeV) they can spall atoms in minerals that are located at, or just below the Earth's surface. The products of these spallation reactions have a bimodal mass distribution with one particle having a mass that is slightly less than the parent atom, and a shower of much lighter particles (typically 1-3 atomic mass units). If oxygen and silicon are the parent atoms in the spallation reaction, then cosmogenic ^{10}Be and ^{26}Al are commonly produced. Both ^{10}Be and ^{26}Al are radioactive, with currently accepted half-lives of 1.39±0.16Ma (Chemeleff et al, 2009; Korschinek et al, 2009) and 708±17ka (Nishiizumi, 2004) respectively. The rate of cosmogenic nuclide production by spallation is controlled by the secondary neutron flux to the host mineral. Similarly to the atmosphere, this flux attenuates approximately exponentially with depth below the Earth's surface (figure 1.6), and

below about 5m production by spallation becomes negligible (~10^{-3} atoms per gram per year, Gosse & Phillips, 2001).

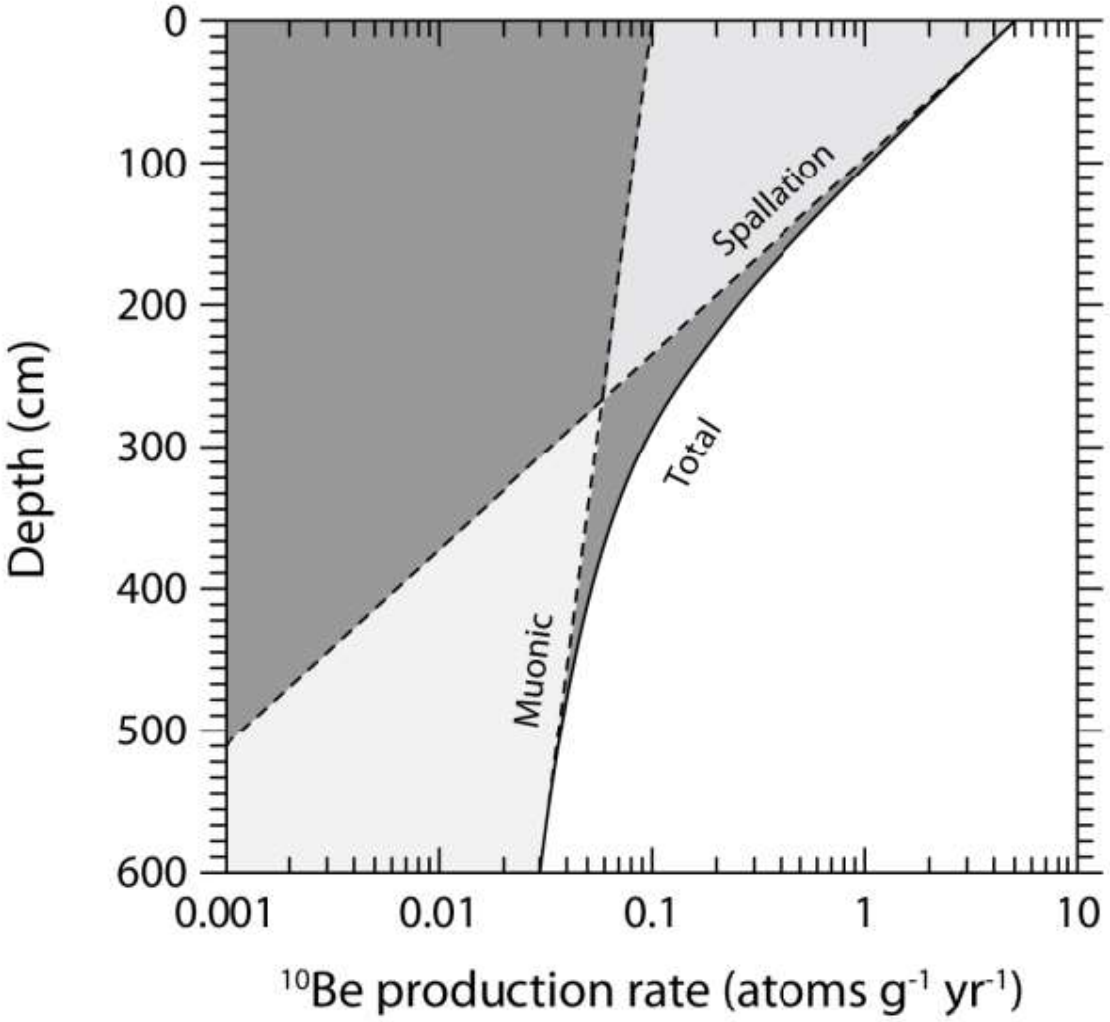

Figure 1.6. How the production rate of in-situ cosmogenic nuclides changes with depth. At shallow depths, spallation is the dominant production mechanism. Below about 3m muon capture becomes the dominant mechanism. (Gosse & Phillips, 2001)

Because muons, which make up about 50% of the secondary cosmic ray flux at the Earth's surface, only weakly interact with atoms in the Earth's crust they can penetrate further into the Earth's surface than neutrons (figure 1.6). The average energy of the muon flux at the earth's surface is about 4GeV, and muons of this energy can penetrate the Earth's surface to a depth of about 8m. The highest energy muons (~100 GeV) can penetrate the Earth's surface up to about 150m. At depths greater than 3m below the surface muonic processes become the dominant cosmogenic nuclide production mechanism. Both oxygen and silicon can capture low energy slow moving negative muons to produce cosmogenic ^{10}Be and ^{26}Al respectively. High energy or fast

muons can interact with atoms in the Earth's crust to produce secondary neutrons with enough energy to spall oxygen and silicon atoms to produce cosmogenic ^{10}Be and ^{26}Al (Gosse & Phillips, 2001; Heisinger et al, 2002a, b).

In-situ cosmogenic nuclides can also be produced when the nucleus of an atom in the Earth's crust captures a low energy (0.025eV-~10 keV) neutron. Low energy neutrons are called thermal neutrons, and are produced in spallation reactions triggered by primary or secondary cosmic rays or from the decay of radioactive isotopes. Very small amounts of ^{10}Be can be produced from beryllium-9 (^{9}Be) by this process (Gosse & Phillips, 2001; Dunai, 2010).

Very small amounts of some in-situ cosmogenic nuclides can also be produced via non-cosmogenic processes. For example, ^{10}Be can be produced when an atom of lithium-7 captures an α particle and ^{26}Al can be produced when an atom of sodium-23 captures an α particle (Sharma & Middleton, 1989; Placzek et al, 2007)

1.3 In-situ cosmogenic nuclide production rates

In order to use in-situ cosmogenic nuclides as a dating method it is necessary to know the rate at which they are produced. This can be estimated by using numerical models (e.g. Masarick & Ready, 1994, 1995, 1996; Masarick & Beer, 1999). However, these models have large uncertainties (~25%) which limits their usefulness for high-precision dating (Masarick & Beer, 1999; Leya et al, 2000; Sisterson, 2005).

Production rates can also be estimated by exposing target minerals to beams of neutrons or muons in a particle accelerator or to natural secondary cosmic rays. Particle accelerator experiments have made a significant contribution to the understanding of the muonic contribution to cosmogenic nuclide production rates. However, because these experiments have very short timescales relative to geological processes, experimental-derived production rates have to be scaled using estimates of long term solar activity to be useful (Leya et al, 1998; Heisinger et al, 2002 a, b; Sisterson, 2005; Yokoyama et al, 1977; Nishiizumi et al, 1996; Brown et al, 2000; Vermeesch et al, 2008).

The most common way of estimating production rates is to measure the concentrations of in-situ produced cosmogenic nuclides in geological surfaces that are stable and can be reliably dated by other methods such as radiocarbon, luminescence, Ar/Ar, Dendrochronology or varve chronology (e.g. Kurz et al, 1990; Cerling & Craig, 1994a; Kubik et al, 1998; Dunai & Wijbrans, 2000; Balco & Schaefer 2006). In the case of stable cosmogenic nuclides, the production rate can be calculated by dividing the measured concentration of the nuclide by the age of the surface and then applying a correction factor that accounts for the effects of sample location and thickness, atmospheric and topographic shielding and erosion on the measured cosmogenic nuclide concentration. In-situ cosmogenic nuclide concentrations are usually reported as atoms of nuclide per gram of host mineral. If the cosmogenic nuclides are radioactive, then the amount of nuclide lost to radioactive decay over the time period being considered has to be accounted for in the production rate calculation.

In order to allow direct comparison of production rates from different geographic locations, local production rates are normalised to production rates at sea level and high latitude (SLHL). This is done by applying a scaling factor to local production rates that accounts for the local variations in secondary cosmic ray flux at the Earth's surface. These scaling factors can be derived from published literature (e.g. Lal, 1991; Dunai, 2000; Stone, 2000; Dunai, 2001a; Desilets & Zreda, 2003; Lifton et al, 2005), and they account for spatial and temporal variations in the Earth's magnetic field and atmospheric pressure, and for changes in solar activity. Different scaling systems will produce different scaling factors for a particular locality, therefore the scaling system used must be clearly stated when normalising production rates to SLHL.

Because of the difficulties associated with accurately predicting cosmic ray flux at any given point on the Earth's surface, these scaling systems need to be calibrated using local production rates from reference sites that have robust independent age control and exposure history.

There are web-based tools for calculating production rates such as the CRONUS-Earth Web Calculators (Marrero et al, 2016) or The Online Calculators Formerly Known as the CRONUS-Earth Online Calculators (Balco et al, 2008). These tools can be used to

calculate production rates, exposure ages and erosion rates at sites for which there are no calibrated production rate data.

However, production rates calculated using web-based calculators for sites that are located close to reference sites are not always in agreement with the measured production rates at these sites. The web-based calculators tend to overestimate production rates, and there is a lot of scatter in the predicted values. Furthermore, most of the data used for calibrating scaling systems and web-based calculators is from the northern hemisphere (Balco et al, 2008; Borchers et al, 2016). This suggests that that the models and calibrations underpinning online calculators are still not perfect, and the outputs of these calculators need to be interpreted with care, especially for areas where there are no reference sites.

^{10}Be production rates measured at two sites at mid-latitudes in the southern hemisphere (Macaulay Glacier, New Zealand, latitude 44^{o}S and Lago Agentino, Argentina, latitude 50^{o}S) suggest that web-based calculators overestimate ^{10}Be production in the southern hemisphere by 10-14% (Putnam et al, 2010; Kaplan et al, 2011). Furthermore, when Kaplan et al (2011) used the production rate from Macaulay Glacier to calculate ^{10}Be exposure ages at Lago Argentino, the exposure ages were in agreement with the ^{14}C chronology for Lago Argentino. This suggests that the ^{10}Be production rate at Macaulay Glacier can be used as a reliable estimate of ^{10}Be for southern hemisphere mid-latitudes. There are currently no ^{26}Al production rate calibration sites in the southern hemisphere (Borchers et al, 2016).

If quartz is the host mineral for the production of cosmogenic ^{10}Be and ^{26}Al, then using the currently accepted values of the half-lives of ^{10}Be and ^{26}Al, the total ^{10}Be production rate is about 4.5 atoms/gram of quartz/year (atoms/g/a) normalised to SLHL and the total ^{26}Al production rate is about 30 atoms/g/a normalised to SLHL (Balco et al, 2008), giving a production ratio of 6.75. At the Earth's surface, spallation accounts for 96.4% of ^{10}Be production and 95.5% of the production of ^{26}Al in quartz, with the remainder accounted for by muonic processes (Heisinger et al, 2002a, b).

1.4 Measuring in-situ produced cosmogenic nuclide concentrations

Because the concentrations of most in-situ produced cosmogenic nuclides are so low (typically less than a million atoms/g of host mineral) conventional geochemical methods such as x-ray fluorescence or mass spectrometry on whole rock samples cannot usually be used. However, because ^{36}Cl is produced in calcium bearing rocks at relatively high rates compared to other cosmogenic nuclides and most carbonate rocks contain about 30% calcium, whole rock dissolution can be used on limestones (Dunai, 2010).

In-situ cosmogenic nuclides have to be extracted from the host mineral then concentrated and purified before measurement. This is usually done by separating the host mineral from a sample then extracting the nuclides of interest by acid digestion and purification by ion-exchange chromatography and selective precipitation. Furthermore, the meteoric production of some cosmogenic nuclides is much greater than the in-situ production rate, and some of the meteoric produced cosmogenic nuclides may be adsorbed onto the surface of host mineral grains. This meteoric component will add to the in-situ concentration if it is not removed prior to digestion of the host mineral. A typical process for extracting ^{10}Be and ^{26}Al from quartz is described by Kohl & Nishiizumi (1992).

The stable in-situ cosmogenic nuclides that are routinely measured are noble gases (helium, neon, argon), and this is done by crushing or heating up to about 1g of clean host mineral and analysing the released gases using a noble gas mass spectrometer (Dunai, 2010).

Radioactive cosmogenic nuclides tend to be less abundant in their host minerals than stable cosmogenic nuclides. Typical sample sizes range from about 10g of clean host mineral to about 100g. Because it is much easier to precisely measure isotope ratios than absolute concentrations of nuclides with very low abundances, samples are spiked with a known amount of a common stable isotope of the nuclide of interest before digestion and purification. The purified sample is then loaded into a target and the ratio of the stable isotope to radioactive cosmogenic nuclide is measured using an accelerator mass spectrometer (AMS) (figure 1.7), which is capable of precisely

measuring ratios as small as 10^{-16} (Dunai, 2010). AMS achieves this level of sensitivity because the ionised sample is accelerated to very high energies (up to 60MeV) compared to conventional mass spectrometry. Acceleration to such high energies allows the resolution of very small differences in mass to charge ratio due to very efficient molecular disintegration and charge stripping, which allows for efficient suppression of isobaric interference between the nuclide of interest and other species with very similar mass to charge ratios. Furthermore, because AMS only requires 1-3mg of processed sample for precise measurements, required sample sizes are greatly reduced compared to other methods of measuring cosmogenic nuclide concentration, such as decay counting (Elmore and Phillips, 1987). For samples with relatively high (>10^{-9}) $^{10}Be/^{9}Be$ ratios, the ratio can be measured using thermal ionisation mass spectrometry (TIMS) or secondary ionisation mass spectrometry (SIMS) (e.g. von Blankenburg et al, 1995). In either case, the isotope ratio and the amount of stable isotope added can then be used to calculate the amount of cosmogenic nuclide present.

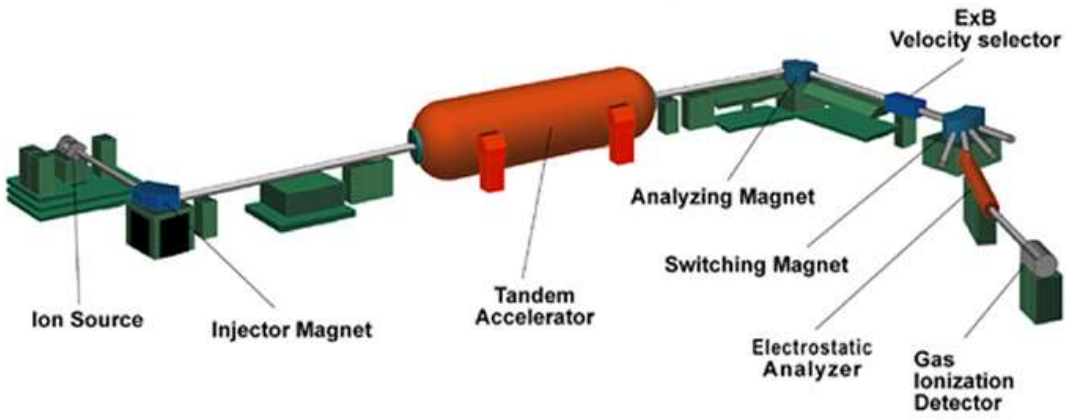

Figure 1.7. A schematic layout of a typical accelerator mass spectrometer. The sample is loaded into the ion source. The ionised sample is then directed through the tandem accelerator to the analyser and detector by the magnets where the isotope ratio is measured. Image: PRIME Lab.

1.5 Cosmogenic nuclide exposure dating

Any geologically stable (i.e. non-eroding) surface that contains suitable host minerals can be dated using in-situ cosmogenic nuclides as long as it can be assumed that there

are no inherited cosmogenic nuclides in the surface and that the surface has not been reburied after initial exposure. When the surface is exposed to secondary cosmic rays, the concentration of in-situ produced cosmogenic nuclides increases over time. In the case of stable nuclides, the concentration increases in direct proportion to the time that the surface is exposed. If the nuclide is radioactive, it will start to decay as soon as production starts. The rate of decay is related to the decay constant of the nuclide and concentration in the host mineral. Over time, the increasing cosmogenic nuclide concentration results in a decay rate that equals the rate of production (figure 1.8) and the concentration of the cosmogenic nuclide reaches saturation or secular equilibrium (Dunai, 2010).

The amount of material required for cosmogenic nuclide dating means it is not usually possible to collect very thin samples from geological surfaces. Therefore, measured in-situ cosmogenic nuclide concentrations have to be corrected for the thickness of the sample. This is because the mass of the sample partially shields the bottom of the sample from the local secondary cosmic ray flux. The amount of shielding is related to the thickness and density of the sample and the attenuation coefficient for spallation reactions in the sample. Typical values for the attenuation coefficient in the Earth's crust are 150-170g/cm^2 (Dunai, 2010). This equates to a depth of 0.6-0.7m in typical crustal rocks. It is also necessary to correct measured in-situ cosmogenic nuclide concentrations for the effects of local topographic shielding as described previously under production of in-situ terrestrial cosmogenic nuclides.

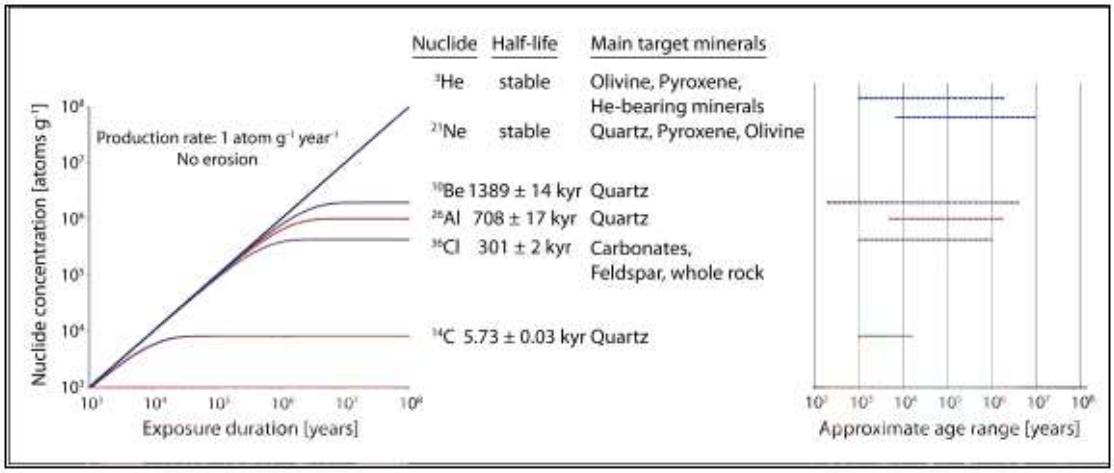

Figure 1.8. How the concentration of cosmogenic nuclides changes with increasing exposure time in a non-eroding surface and the useable age ranges for the most commonly used cosmogenic nuclides. (Darville, 2013)

In theory there is no upper limit on the useable age range for stable cosmogenic nuclides. However, most geological surfaces that are exposed to secondary cosmic rays will be subject to erosion, which acts to reduce the concentration of in-situ cosmogenic nuclides in the uppermost layers. This means that the concentration of stable cosmogenic nuclides will reach saturation in an eroding surface, and the time to reach saturation is related to the rate of erosion.

For radioactive cosmogenic nuclides, the upper limit is related to the half-life of the nuclide. In practice, the upper limit of the useable age range is of the order of 2-3 half-lives of the nuclide. The lower limit on the useable age range for a particular nuclide is related to the production rate of that nuclide and the ability to accurately measure the concentration of that nuclide in the host mineral. The useable age ranges for ^{10}Be and ^{26}Al in quartz are ~0.2ka-~5Ma and ~5ka-~2Ma respectively (Darville, 2013).

For radioactive cosmogenic nuclides, the time to reach saturation is further reduced in an eroding surface. Figure 1.9 shows the effect of erosion on the time it takes for the concentration of in-situ cosmogenic nuclides to reach saturation.

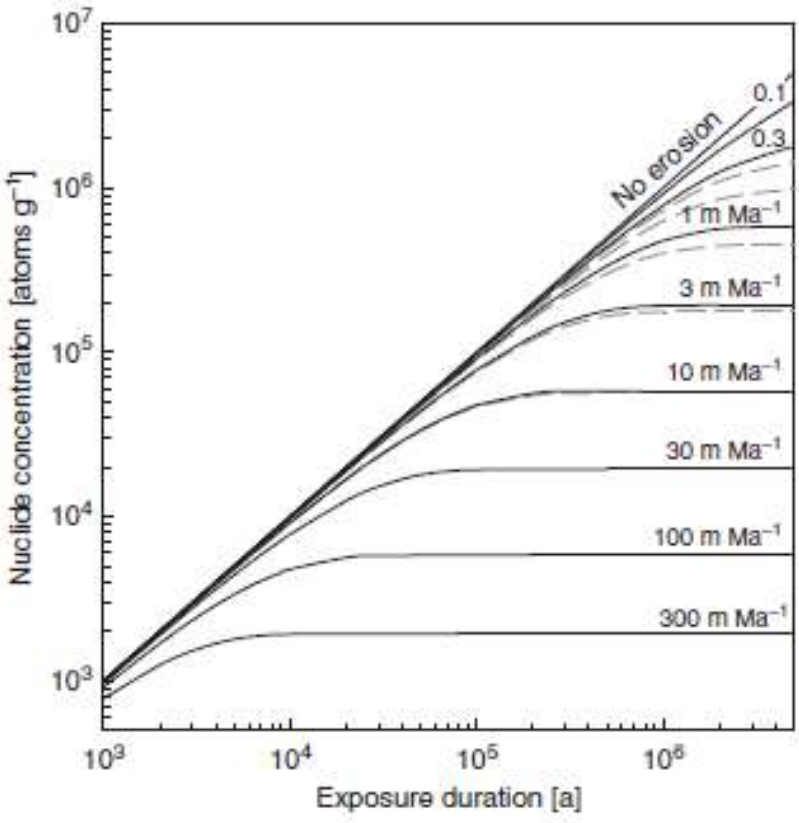

Figure 1.9. The effect of erosion on in-situ cosmogenic nuclide concentrations in an eroding surface. Solid lines are for stable nuclides. Dashed lines are for ^{10}Be produced at a rate of 1 atom/g/a. (Dunai, 2010)

If the rate of erosion of the surface being dated can be independently quantified and assumed to be constant, it is possible to correct the exposure age of the surface for the effects of erosion (Lal, 1991; Niedermann, 2002). If it is not possible to independently quantify the erosion rate then the exposure age of a surface can be estimated by using the concentrations of 2 cosmogenic nuclides (Lal & Arnold, 1985; Lal, 1991; Gosse & Phillips, 2001). The use of 2 (or more) in-situ cosmogenic nuclides can also allow the testing of the validity of any assumptions about inheritance, erosion rates or reburial history. Figure 1.10 shows how the concentration of ^{10}Be and the ratio of ^{10}Be to ^{26}Al in quartz can be used to test assumptions about the exposure/burial history of a site.

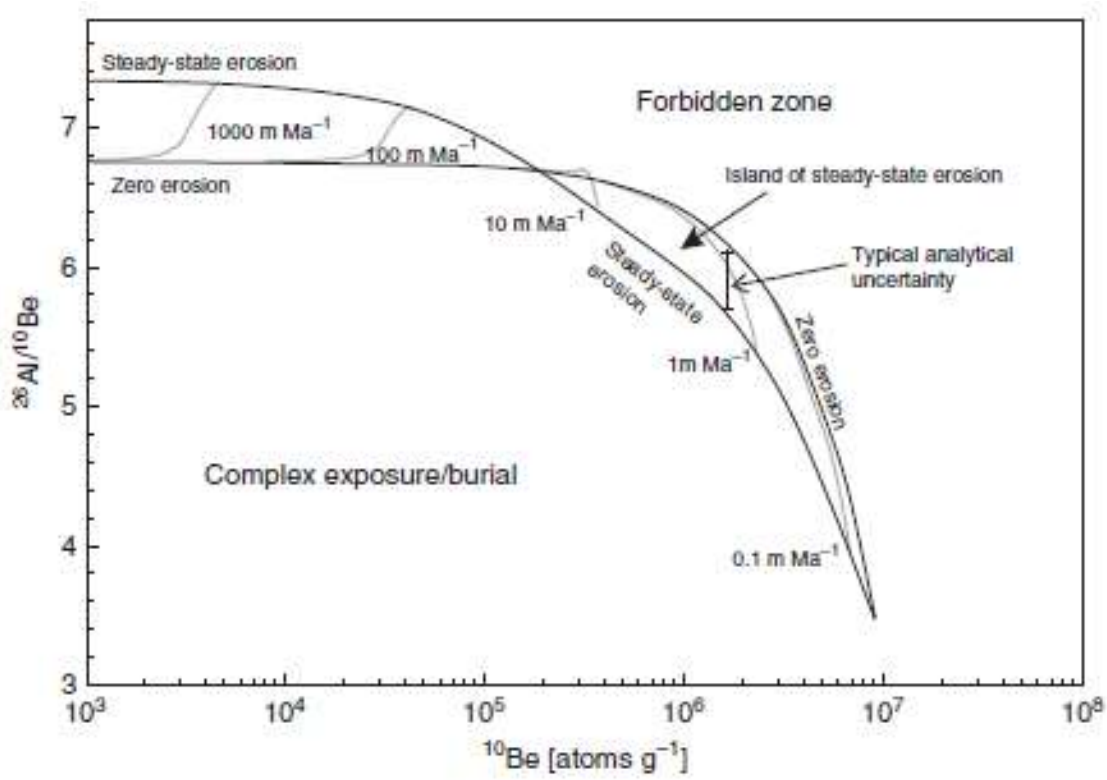

Figure 1.10. A plot of the ^{26}Al/ ^{10}Be ratio vs ^{10}Be concentration. If the cosmogenic nuclide measurements from a sample plot inside the island of steady-state erosion, then the sample has a simple erosion/burial history and the erosion rate contours can be used to estimate the erosion rate. If the sample measurements plot below the island, then at least one of the assumptions about inheritance, reburial or erosion history is suspect. The forbidden zone refers to measurements that cannot be produced by any natural exposure scenario. (Dunai, 2010; Lal, 1991)

1.6 Using in-situ cosmogenic nuclides to infer erosion rates

In sediments that have been buried, it is possible to infer the rate at which the sediment was eroded from its source prior to burial by measuring the present-day concentrations of 2 cosmogenic nuclides (Lal, 1991; Dunai, 2010). If at least one of the cosmogenic nuclides measured is radioactive, then concentration of the radioactive nuclide and the ratio of the cosmogenic nuclides in the sediment will decrease over time once the sediment is buried. Figure 1.11 shows how the concentration of ^{10}Be and the ratio of ^{26}Al to ^{10}Be in quartz can be used to infer pre-burial erosion rates.

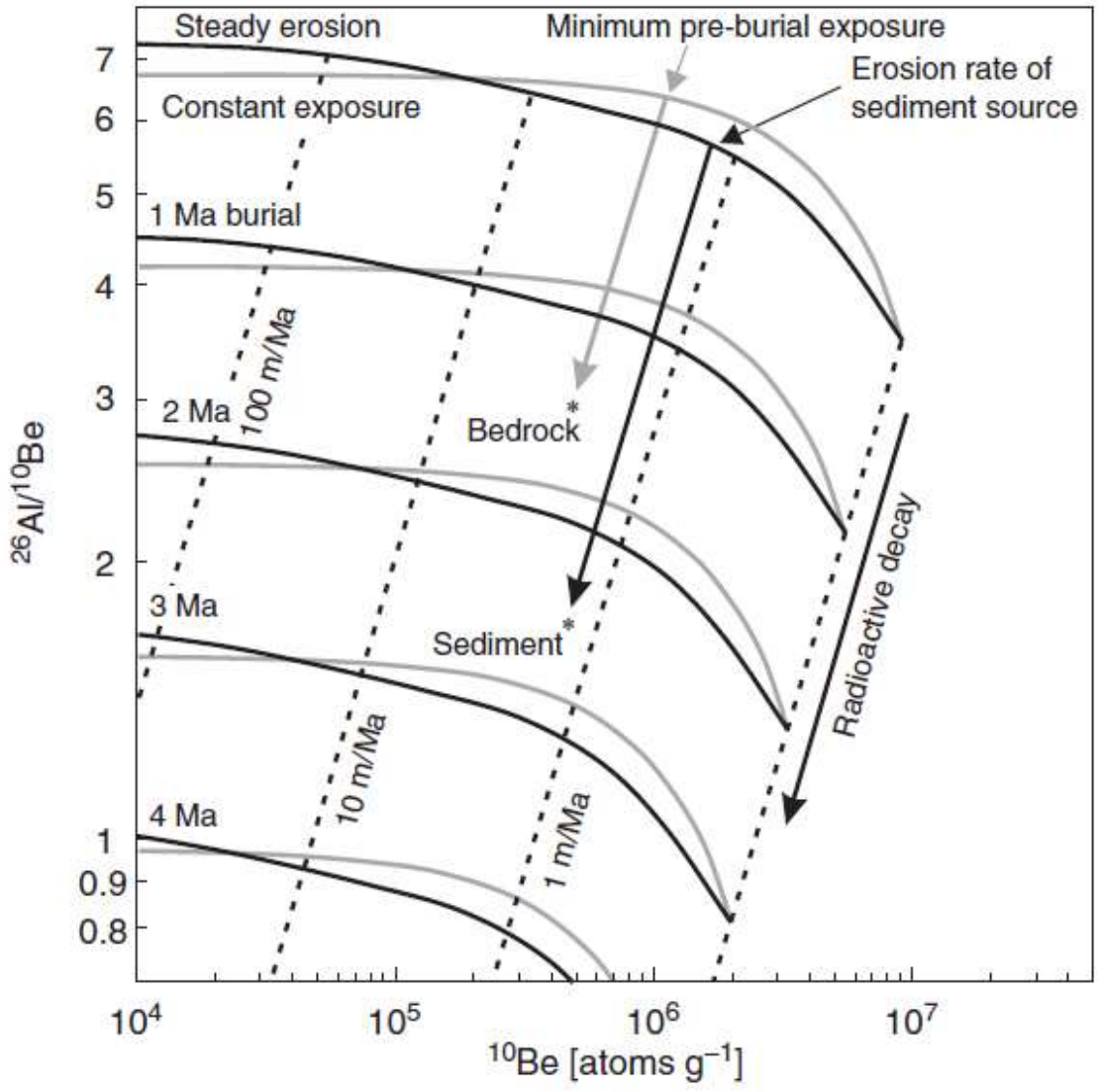

Figure 1.11. Plot of the ^{26}Al/ ^{10}Be ratio vs ^{10}Be concentration. When the sediment is exposed on the surface the ^{10}Be concentration and the ^{26}Al/ ^{10}Be ratio evolve along the steady erosion curve. After burial, the ^{10}Be concentration and ^{26}Al/ ^{10}Be ratio evolves along the arrowed path that parallels the erosion rate isoclines to the present-day measured values. The intersection of the steady erosion curve and the arrowed path gives the erosion rate at the time that the sediment was buried. (Dunai, 2010)

1.7 Cosmogenic nuclide burial dating

Burial dating using in-situ cosmogenic nuclides utilises the principle that when a suitable host mineral, that has been exposed to secondary cosmic rays for long enough to accumulate significant quantities of radioactive cosmogenic nuclides that have different decay rates, is rapidly and completely shielded from incoming cosmic radiation then the ratio of cosmogenic nuclides will vary from the initial production ratio over time (Klein et al, 1986; Lal, 1991; Granger & Muzikar, 2001; Balco & Rovey, 2008). Ideally, the nuclides used for burial dating should be produced in the same host mineral and the initial production ratio, which is ~6.75: 1 in the case of $^{26}Al/^{10}Be$ (Balco & Rovey, 2008) should be unaffected by altitude, latitude and depth of production in the host mineral (Brown et al, 1992).

^{10}Be and ^{26}Al are a good choice of in-situ cosmogenic nuclides for burial dating because they can both be measured in quartz. The initial production ratio is also minimally affected by the pre-burial location of the quartz, and the simple chemical makeup of quartz ensures that there is no significant non-cosmogenic production of ^{10}Be or ^{26}Al (Dehnert & Schluchter, 2008). Furthermore, quartz is relatively abundant on the Earth's surface, and is physically and chemically robust enough to survive weathering and long-distance transport. ^{10}Be and ^{26}Al also have half-lives that are sufficiently different that post burial ratios will differ from initial production ratios over geologically useful timescales (Figure 1.12).

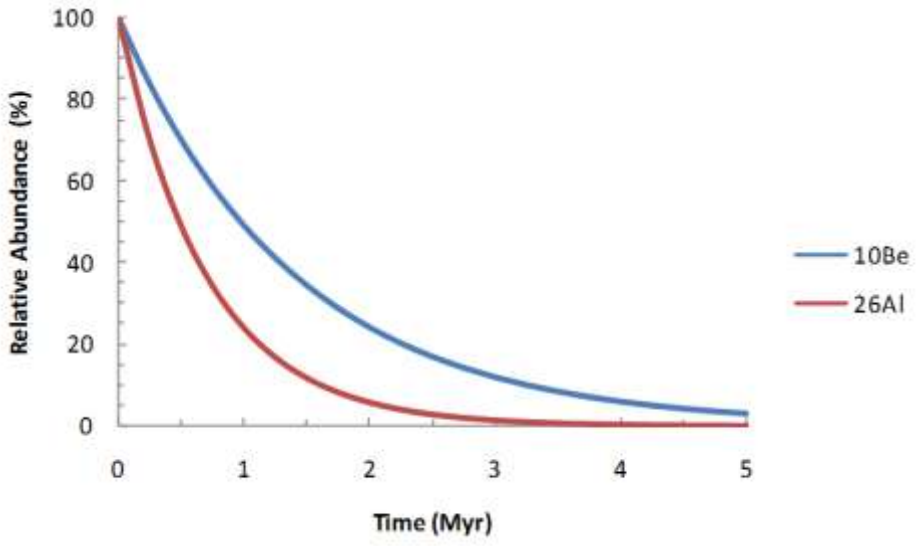

Figure 1.12. How the relative abundances of ^{10}Be and ^{26}Al change over time.

$^{26}Al/^{10}Be$ burial dating is useable over a theoretical age range of ~100ka to ~5Ma. The lower limit is defined by the uncertainties in the measurement of post burial nuclide ratios, pre burial production rates and estimates of nuclide half-lives. The upper limit is defined by the ability to precisely measure low nuclide concentrations, in particular, ^{26}Al. In practice, the upper limit is often limited by the amount of time a sample has been exposed on the surface prior to burial because it takes thousands to tens of thousands of years to accumulate sufficient concentrations of cosmogenic nuclides to still be measurable after millions of years of burial. Under ideal conditions, the uncertainty in burial ages is about 5%. (Granger & Muzikar, 2001).

The accuracy of a burial age is dependent on the assumptions of rapid and complete shielding of the buried material from secondary cosmic rays, and that the ratio of cosmogenic nuclides in the material at the time of burial is the same as the production ratio. In very slowly eroding landscapes (>0.001mm/a) the concentrations of ^{10}Be and ^{26}Al in the host mineral start to approach saturation, driving the pre-burial $^{26}Al/^{10}Be$ ratio in the host mineral away from the production ratio. Varying erosion rates can also drive the pre-burial ratio away from the production ratio (Granger & Muzikar, 2001). However, if the average erosion rate is sufficiently large (>0.01mm/a) then the pre-burial ratio will not differ significantly from the production ratio (Granger & Muzikar, 2001). Pre-burial cosmogenic nuclide ratios can also differ from production ratios in cases where burial is not deep enough to prevent post-burial production by muonic processes, or the sample may have a complex burial history where there are periods of partial or complete burial and hence shielding from secondary cosmic rays followed by periods of re-exposure (Granger & Muzikar, 2001; Dunai, 2010).

It is possible to use a third in-situ cosmogenic nuclide to infer the pre-burial history of the host mineral. The concentration of a stable cosmogenic nuclide only changes during periods of exposure, whereas the concentrations of cosmogenic radionuclides changes with both exposure and burial. If it can be assumed that there was only one period of exposure and burial prior to final burial, the measurement of the concentration of a stable nuclide such as ^{21}Ne can be used to calculate the pre-burial exposure time and allow for the determination of the pre-burial ratio of the concentrations of radionuclides. The measurement of a stable cosmogenic nuclide as

well as ^{10}Be and ^{26}Al can also extend the useable age range and increase the accuracy of the burial ages (figure 1.13). The increase in useable age range is because it is possible to use the ^{10}Be/^{21}Ne ratio to calculate the burial age. The increase in accuracy is because it is easier to precisely measure low concentrations of ^{10}Be compared to ^{26}Al, and the longer half-life of ^{10}Be means that there is more ^{10}Be in the sample after a long period of burial. Furthermore, the use of a stable isotope paired with a radioactive isotope reduces the effects of the uncertainties in the decay constants of the radioactive isotopes on the overall uncertainty of the burial age (Granger & Muzikar, 2001; Balco & Shuster, 2009).

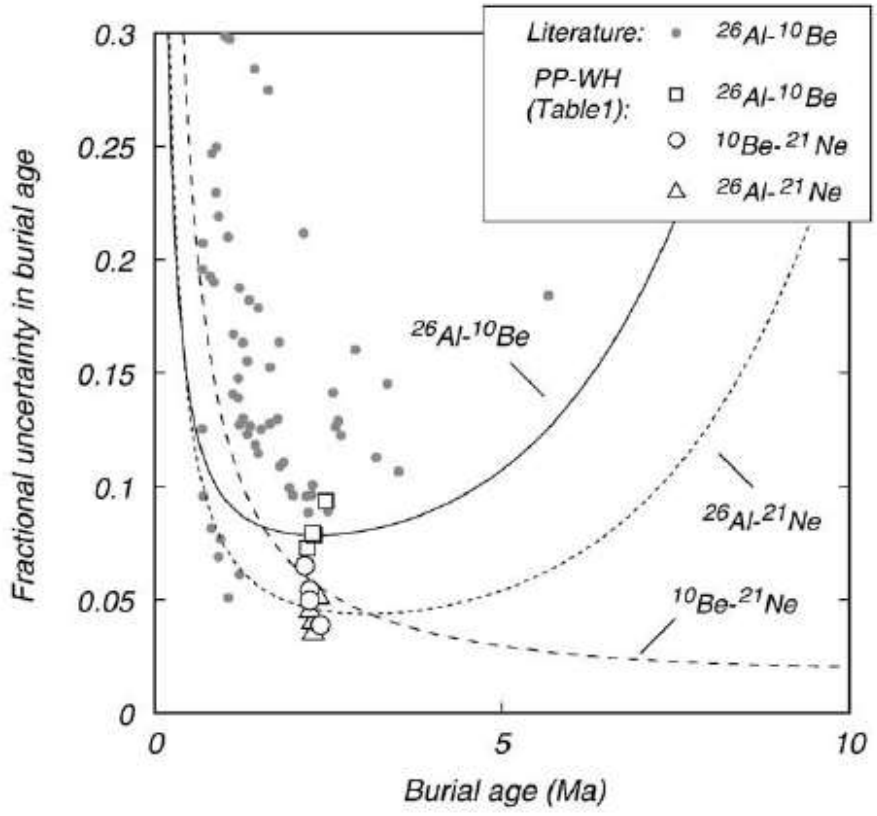

Figure 1.13. The effect of measuring a stable cosmogenic nuclide as well as ^{10}Be and ^{26}Al on the accuracy and useable age range of burial dating. (Balco & Shuster, 2009)

The accuracy of a burial age also depends on the accuracy of the decay constants and hence half-lives of each radionuclide used. There is general agreement on the value of the decay constant for ^{26}Al, which has a value of 9.83±0.25 x10^{-7} /a (Nishiizumi, 2004). However, there are a number of values of the decay constant for ^{10}Be in use. Some are in close agreement (e.g. Nishiizumi et al, 2007; Chemeleff et al, 2009; Korschinek et al, 2009) with values of 5.097±0.099 x10^{-7} /a and 4.987±0.043 x10^{-7} /a respectively. Other

values differ significantly (e.g. 4.59±0.01 x10^{-7} /a, Hoffmann et al, 1987). At present, the values of the decay constant for ^{10}Be proposed by Chemeleff et al (2009) and Korschinek et al (2009) are considered to be the generally accepted value. When calculating and reporting burial ages it is necessary to both clearly state which values of the decay constants have been used, and to use those values consistently in the calculation of pre-burial production rates and the time elapsed since burial.

1.8 The application of cosmogenic nuclide burial dating to cave sediments

In eroding landscapes, physical and chemical processes break down bedrock into particles that can be mobilised by gravity, aeolian and fluvial processes, and a significant proportion of this material ends up in the waterways that drain the landscape. In karst landscapes, the waterways often sink underground into underlying cave systems (figure 1.14).

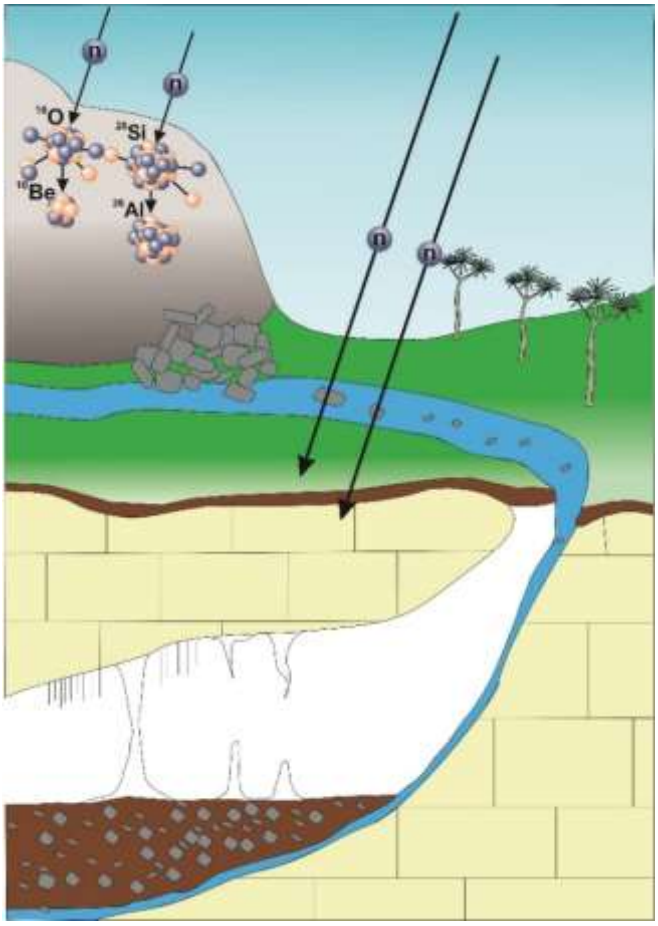

Figure 1.14. How in-situ produced cosmogenic nuclide bearing materials can be transported underground and preserved in karst landscapes.

When secondary cosmic rays interact with quartz exposed on the surface of a steadily eroding landscape, ^{26}Al and ^{10}Be are produced in a ratio of ~6.75:1 (Balco & Rovey, 2008). Once eroded material ends up in waterways, fluvial processes will generally rapidly transport and emplace this material deep enough into a cave system to ensure full shielding from secondary cosmic rays. The ^{26}Al to ^{10}Be ratio then decreases over time according to the equation

$$\frac{N_{26}}{N_{10}} = \left(\frac{N_{26}}{N_{10}}\right)_0 e^{\left(\frac{1}{\tau_{26}} - \frac{1}{\tau_{10}}\right)} \qquad \text{Equation 1.}$$

$(N_{26}/N_{10})_0$ is the pre burial $^{26}Al/^{10}Be$ ratio, N_{26}/N_{10} is the present-day measured ratio, t is the time since burial and τ_{26} and τ_{10} are the mean lives for ^{26}Al and ^{10}Be respectively (Lal & Arnold, 1985; Klein et al, 1986).

Because the timescale of transport and emplacement of material as sediments within a cave system is very short compared to the half-lives of ^{10}Be and ^{26}Al, the burial age is an accurate estimate of emplacement age. Once sediment is emplaced within a cave system, it becomes fixed relative to the surrounding bedrock. Subsequent incision of surface waterways will eventually lower local water tables, resulting in the draining and eventual abandonment of cave stream passages by the streams that formed them. The uppermost layer of sediment usually represents the last phase of sediment emplacement before abandonment of the passage so a cosmogenic nuclide burial age for the uppermost layer of sediment that infills a now dry cave passage can be used as an estimate of the minimum age of abandonment of the passage by the stream that emplaced the sediment. The age of abandonment can then be correlated with modern stream levels (figure 1.15) or in the case of multi-level cave systems, abandonment ages at different levels within the cave system to calculate stream incision rates (e.g. Granger et al, 1997; 2001).

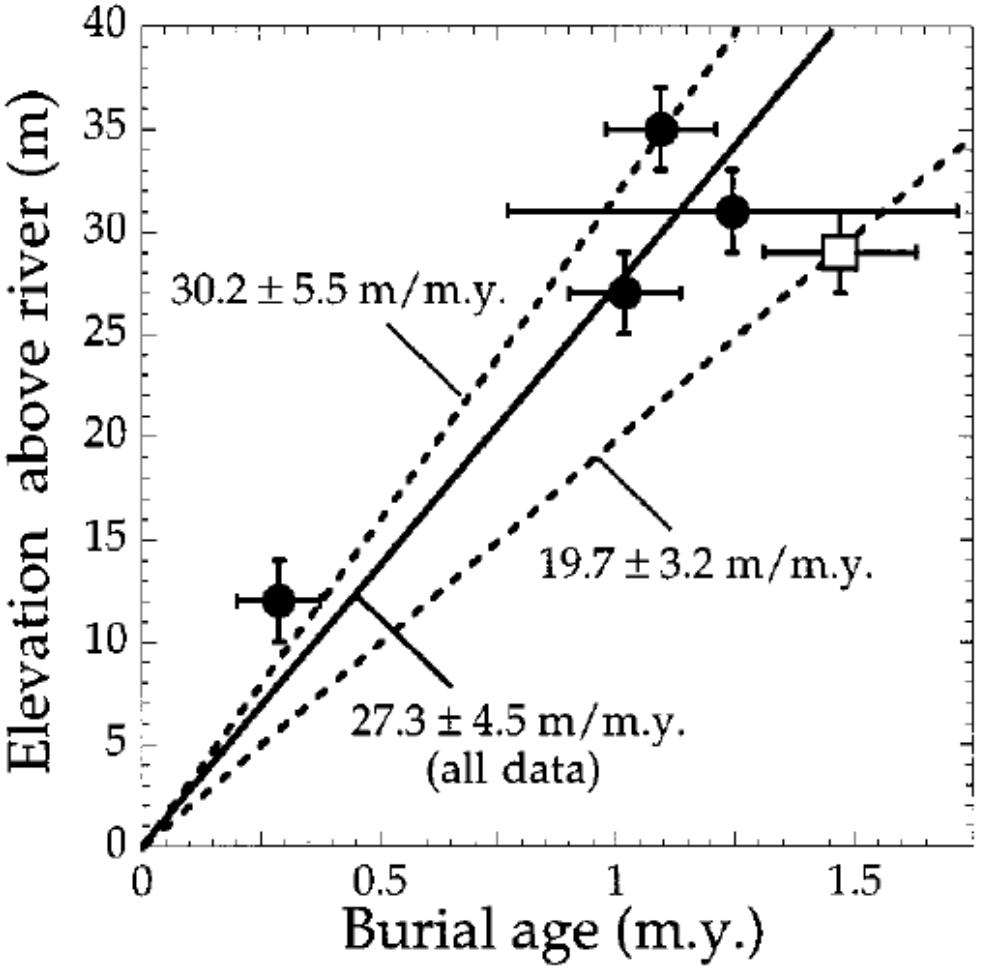

Figure 1.15. Incision rates of the New River, Virginia, USA calculated from cosmogenic $^{26}Al/^{10}Be$ burial ages of sediments in nearby caves. (Granger et al, 1997)

In landscapes where rates of tectonic uplift are in or close to equilibrium with rates of erosion, the rate of stream incision can be used as an estimate of tectonic uplift rate (Williams, 1991). This approach has been used to calculate uplift rates during the Pliocene in the European Alps (e.g. Hoblier et al, 2011).

To ensure that sediment burial dates represent the abandonment of a cave passage, samples should be collected from sites that are at least 30m below the land surface and at least 20m from any entrance to the cave (Granger et al, 2001; Hoblier et al, 2011) to ensure that there is complete shielding from secondary cosmic rays. Samples should also be collected from sites that contain clasts large enough to have been transported by a substantial stream because flood events can deposit fine grained material tens of metres above normal stream level (Granger et al, 2001). In order to minimise the possibility of sampling material that may have been remobilised from

elsewhere in a large or complex cave system, sample sites should not show signs of disturbance. Paleoflow indicators in the sediment such as clast size and imbrication should be consistent with paleoflow directions and velocities indicated by features such as scalloping of cave passage walls.

Depending on exposure duration and suspected burial age, between 50g and 100g of clean quartz is needed to be able to extract sufficient ^{10}Be and ^{26}Al for reliable burial dating. Because good sediment sampling sites are often remote and difficult to access, especially in large or complex cave systems, the sediments sampled need to contain sufficient amounts of quartz to allow sample sizes that are practical to carry out of the cave.

Cosmogenic nuclide burial ages can be corroborated by using other dating methods. Secondary carbonate deposits known as speleothems growing on sediment deposits can be dated using uranium-series or paleomagnetic dating (e.g. Richards & Dorale, 2003; Fairchild et al, 2006). However, this approach is limited by the useable age range for uranium-series dating, which is much less than the useable age range for cosmogenic nuclide burial dating and the lack of resolution of paleomagnetic dating, which only tells us that a speleothem started growing during a period of normal or reversed magnetic polarity. Another factor that needs to be considered when using this approach is that speleothems only start growing once a cave passage is abandoned by the stream that formed it, and there may have been a significant period of time between the abandonment of the passage and the onset of speleothem growth.

Volcanic ash is erupted and emplaced in landscapes over very short timescales. Furthermore, each volcanic eruption has a unique geochemical profile. This unique profile allows the correlation of widely dispersed ash deposits. Volcanic ash deposits can also be precisely dated using a variety of methods (Alloway et al, 2013). If volcanic ash can be recovered from sediment deposits in a cave and either dated directly or correlated on the basis of geochemistry with other known occurrences of that ash, the age of that ash is an independent estimate of the burial age. As an example, Douka et al (2014) used this approach to check the accuracy of a ^{14}C based age/depth model for a cave in Libya.

Finally, cave sediments can also contain fossils, so it is possible to use biostratigraphy or palynology as an independent check on the reliability of a cosmogenic nuclide burial age if macro or microfossils are present at the site sampled for burial dating, and there is a suitable age calibrated microfossil dataset available for comparison.

Chapter 2: Geological and Tectonic history of the Northwest Nelson Area

2.1 Location of Northwest Nelson

The Northwest Nelson area is located adjacent to the Austro-Pacific plate boundary on the eastern margin of the Australian Plate (figure 2.1). The plate boundary formed in the Eocene in response to the onset of anticlockwise rotation of the Pacific Plate relative to the Australian Plate, and has evolved into a transpressive boundary due to south-eastward migration of the pole of rotation of the Pacific Plate since the Oligocene (King, 2000; Sutherland, 1999).

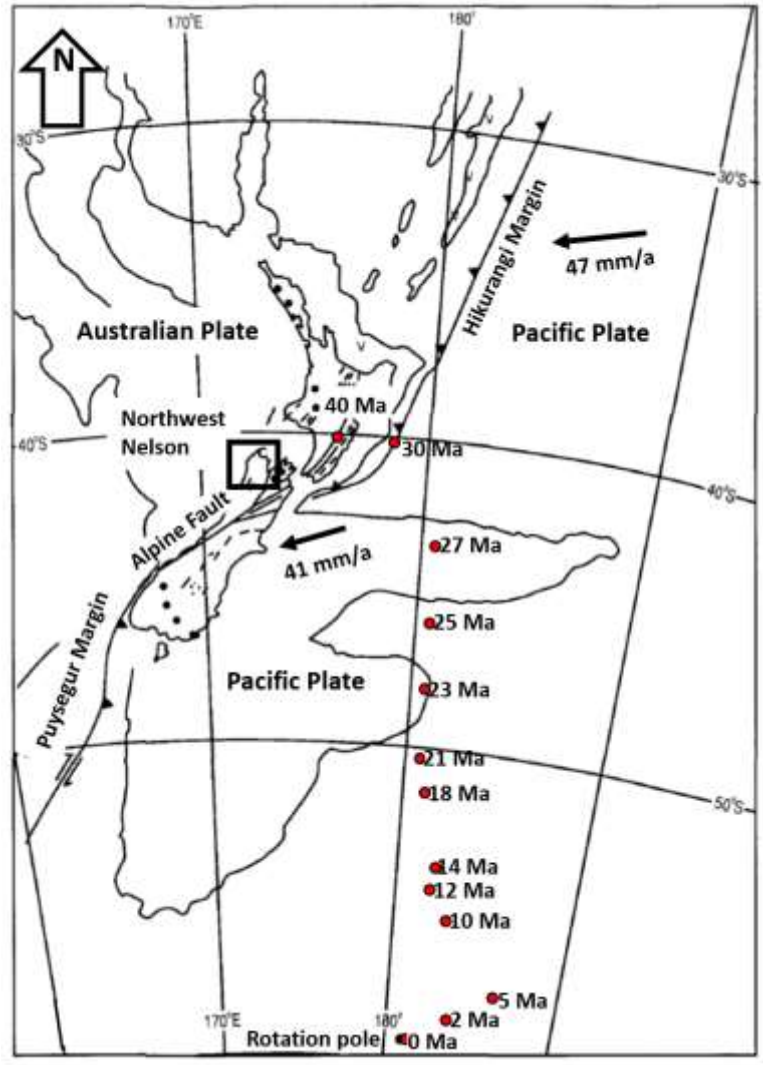

Figure 2.1. The location of the Northwest Nelson area relative to the present day Austro-Pacific plate boundary. The red dots show how the location of the pole of rotation of the Pacific Plate has moved since the inception of the plate boundary in the Eocene. Modified from King, (2000)

The New Zealand sector of the plate boundary is defined by subduction of the Pacific Plate under the Australian Plate off the east coast of the North Island and north-eastern South Island, and by subduction of the Australian Plate under the Pacific Plate off the south-western South Island. Between the two subduction zones lies the Alpine Fault. The Alpine Fault can be traced on land from the northern part of Fiordland northwards to the Marlborough coast. The southern section of the Alpine Fault is characterised by oblique convergence, and offsetting of basement terranes suggests that there has been at least 475km of dextral motion since the inception of the plate boundary (Rattenbury et al, 1998), with most of that motion taking place in the last ~23Ma (King, 2000). The southern part of the Alpine Fault is also the location of New Zealand's Southern Alps. The Southern Alps are on the upthrown side of the Alpine Fault, and have uplift rates ranging from 8-12mm/a depending on location (Norris & Cooper, 2001), among the highest observed rates in the world. The uplift rate on the Alpine Fault increased to its present-day value about 5Ma ago as the pole of rotation of the Pacific Plate approached its current latitude (King, 2000). The northern part of the Alpine Fault splits into a complex fault system known as the Marlborough Fault System, where relative plate motion of about 42mm/a is distributed across a number of strike-slip faults.

2.2 Model based reconstruction of the tectonic history of Northwest Nelson

Reconstructions of the history of the plate boundary suggest that the Eocene tectonic history of Northwest Nelson is characterised by regional extension and subsidence as a result of the anticlockwise rotation of the Pacific Plate about a pole of rotation located approximately 200km to the northeast (figure 2.1) in the mid-late Eocene (King, 2000). This regional extension resulted in the formation of fault bounded basins such as the Murchison Basin (Rattenbury et al, 1998).

During the Oligocene and early Miocene, the pole of rotation migrated southeast (figure 2.1). By the Middle Miocene, it was located about 1500km southeast of Northwest Nelson. This shift in the location of the pole of rotation resulted in the onset of convergence and uplift in Northwest Nelson. This change to a convergent

tectonic regime also resulted in the inversion of sedimentary basins and the reactivation of older normal faults as reverse or strike-slip faults (King, 2000; Rattenbury et al, 1998; 2006).

The pole of rotation continued to migrate south, and by the end of the Miocene it was located about 2200km southeast of Northwest Nelson. This southward migration of the pole resulted in the onset of rapid convergence along the southern part of the Alpine Fault and uplift of the Southern Alps. Along the northern part of the Alpine Fault, relative motion of the Pacific Plate evolved to become parallel with the plate boundary (King, 2000), and this motion was accommodated by distributed strike-slip faulting across the Marlborough Fault System (Rattenbury et al, 2006).

2.3 Overview of the sedimentary history of Northwest Nelson

The basement terranes in Northwest Nelson are some of the oldest rocks in New Zealand, and consist of sediments that were deposited off the margins of Gondwana from the Late Cambrian to the Early Cretaceous. They are subdivided into two provinces, the Western Province and the Eastern Province (figure 2.2). The Western Province is further subdivided into the Buller and Takaka Terranes, which were deposited between the Middle Cambrian to the Early Devonian (Rattenbury et al, 1998). These terranes were accreted onto the Gondwana margin during the Tuhua Orogeny in the Devonian. The Tuhua Orogeny also resulted in the emplacement of the Karamea Suite granites and the mafic Riwaka Complex (Grindley, 1980).

The Eastern Province consists of a suite of igneous and volcanic terranes that range in composition from felsic to ultramafic, as well as quartzofeldspathic sandstones of the Torlesse and Caples terranes (Rattenbury et al, 1998). The Eastern Province was deposited or emplaced off the Gondwana margin from the Carboniferous to the Early Cretaceous, and accreted onto the Gondwana margin during the Rangitata Orogeny in the later part of the early Cretaceous. The felsic Separation Point Batholith was also intruded into the basement terranes of Northwest Nelson during the Rangitata Orogeny (Grindley, 1980).

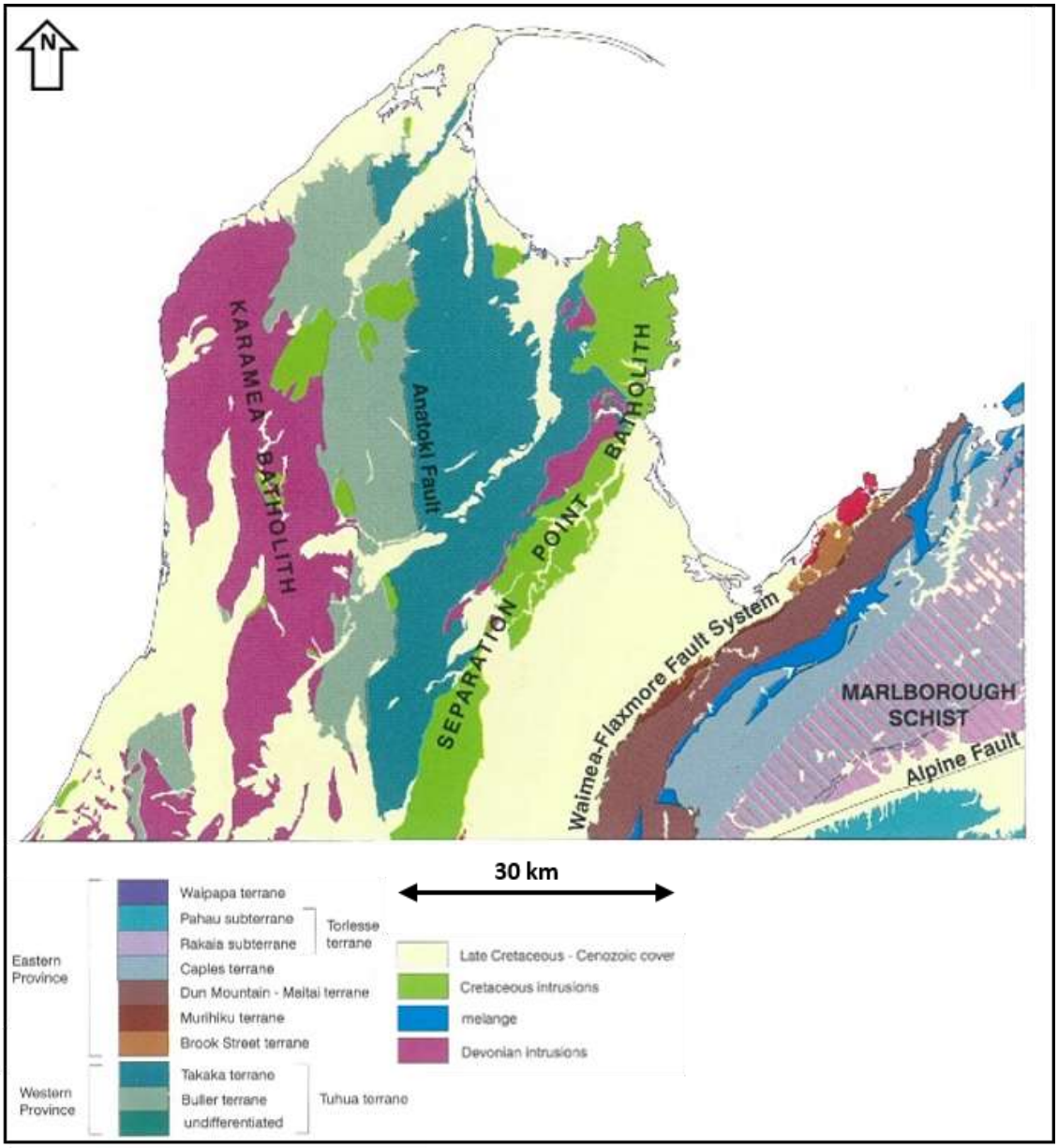

Figure 2.2. Simplified geological map of Northwest Nelson showing the locations of the Paleozoic-early Cretaceous basement rocks of the Eastern and Western Provinces, the Tuhua and Rangitata Intrusives and the late Cretaceous-Cenozoic cover rocks. Modified from Rattenbury et al (1998).

The basement terranes are separated from the Late Cretaceous-Cenozoic cover by a regional unconformity (Rattenbury et al, 1998). This erosion surface is known as the Northwest Nelson Peneplain, and is still preserved on the summits of the mountains of Northwest Nelson (Grindley, 1980). The lower part of the cover sequence is made up of terrestrial to shallow marine facies that were deposited in a passive continental margin setting from the Late Cretaceous to the Early Eocene. The middle part of the sequence consists of marginal marine to deep marine facies that were deposited from the Early Eocene to the Oligocene during a period of marine transgression following

the rifting of Zealandia from Gondwana. The upper part of the sequence is made up of marine facies that shallow upwards into marginal marine and terrestrial facies. The upper part was deposited during the transition from a passive continental margin setting to a convergent margin setting and the uplift of Zealandia at the start of the Kaikoura Orogeny.

The tectonic history of the eastern parts of New Zealand is well documented in the Cenozoic sedimentary rocks that are exposed on the east coast of the North Island and northeastern South Island. However, in the Northwest Nelson area, especially in areas close to the Alpine Fault, uplift and erosion have removed most of the Cenozoic strata and hence most of the record of the timing of the tectonic history of the area.

2.4 Existing knowledge of the tectonic history of Northwest Nelson

2.4.1 Paleomagnetic data

When sediments are deposited, magnetic minerals in the sediments can align themselves with the Earth's magnetic field. Lithification of the sediments can then lock these magnetic minerals in place, preserving a record of the Earth's magnetic field at the time the sediments were deposited. This record of the Earth's magnetic field at the time of deposition, which can be resolved into azimuth and inclination vectors can be measured and compared to the present day magnetic field to see if the sediments have been disturbed after they were deposited. If there is a discrepancy in the azimuth between the magnetic field preserved in the sediments and the present day magnetic field, then the sediments have undergone vertical axis rotation after deposition.

Paleomagnetic investigation of sediments that range in age from late Eocene to mid-late Miocene from a number of sites in the Northwest Nelson area (figure 2.3) show no significant vertical axis rotation since deposition (Turner et al, 2012). In contrast, latest Miocene sediments from areas to the east of the Northwest Nelson area on the opposite side of the Alpine Fault have undergone more than 100^{o} of clockwise vertical axis rotation since deposition (e.g. Little & Roberts, 1997).

The lack of rotation of the sites to the west of the Alpine Fault suggests that the Northwest Nelson area has always been part of the Australian plate, and also has been

an area of relative tectonic stability compared to other areas of New Zealand that are adjacent to the Alpine Fault.

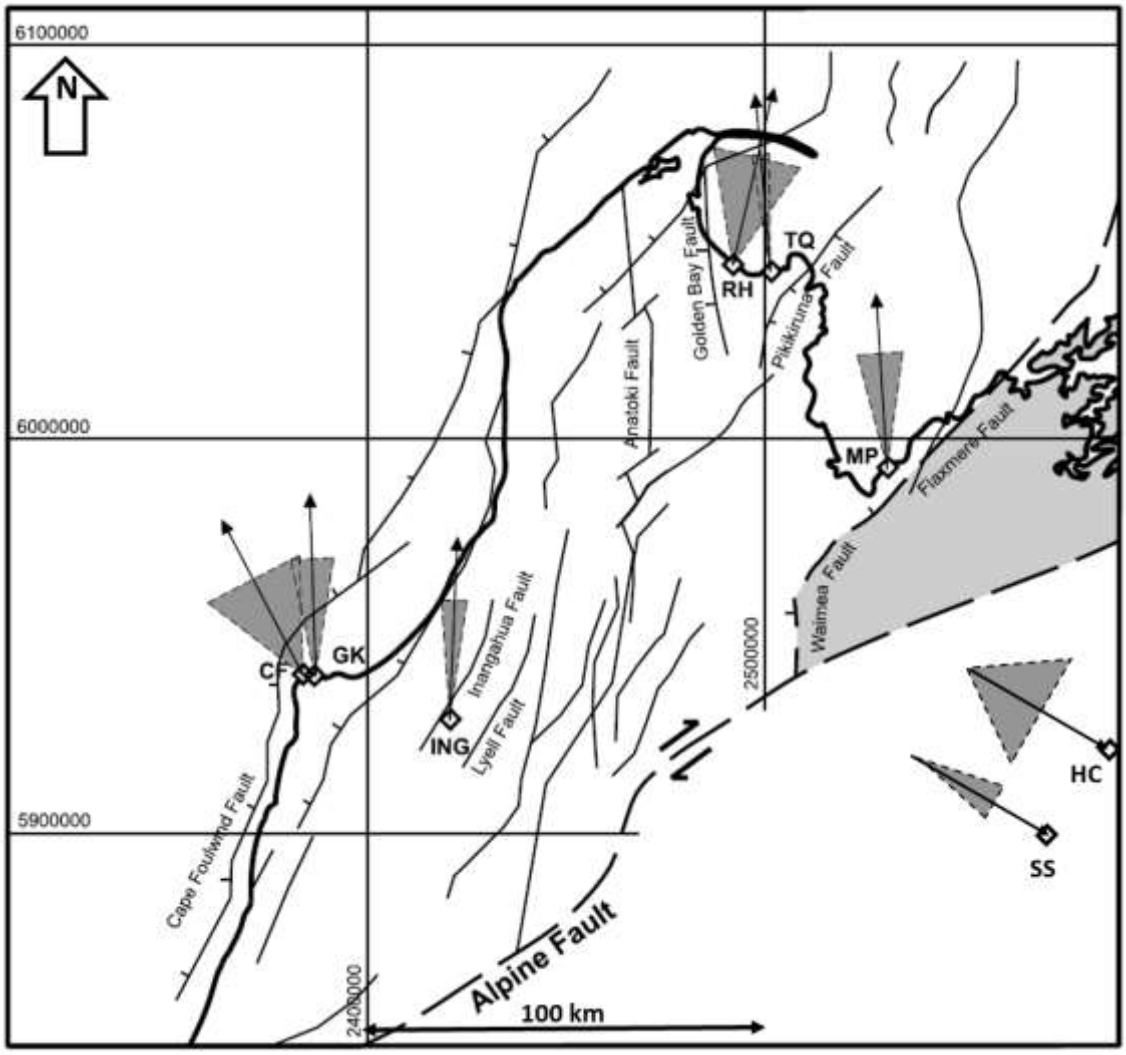

Figure 2.3. Paleomagnetic vertical axis rotation data for Northwest Nelson. Grey triangles are 95% confidence intervals for the magnetic vectors. CF, GK, ING, MP, RH and TQ are from Turner et al (2012). HC and SS are from Little & Roberts (1997)

2.4.2 Published uplift rate data for Northwest Nelson

There is very little published data on uplift rates in the Northwest Nelson area. An early uplift rate map (Wellman, 1979) suggests uplift rates of up to 1.5mm/a in parts of the Northwest Nelson area that are distal to the Alpine Fault. These uplift rates were based on estimates of the relative ages and elevations of the summits of the mountains of Northwest Nelson and a terrace in the Buller River Valley. Revised uplift rate maps (Williams, 1991; 2017) suggest very low (<0.1mm/a) uplift rates in areas

distal to the Alpine Fault and higher uplift rates (~1mm/a) in areas that are proximal to the Alpine Fault (figure 2.4).

Some of the very few measured uplift rates in Northwest Nelson come from the dating of speleothems from caves in the area (figure 2.4). Speleothem basal dates suggest that uplift rates since the Mid-Late Pliocene were in the order of 0.09-0.4mm/a (Williams, 1991).

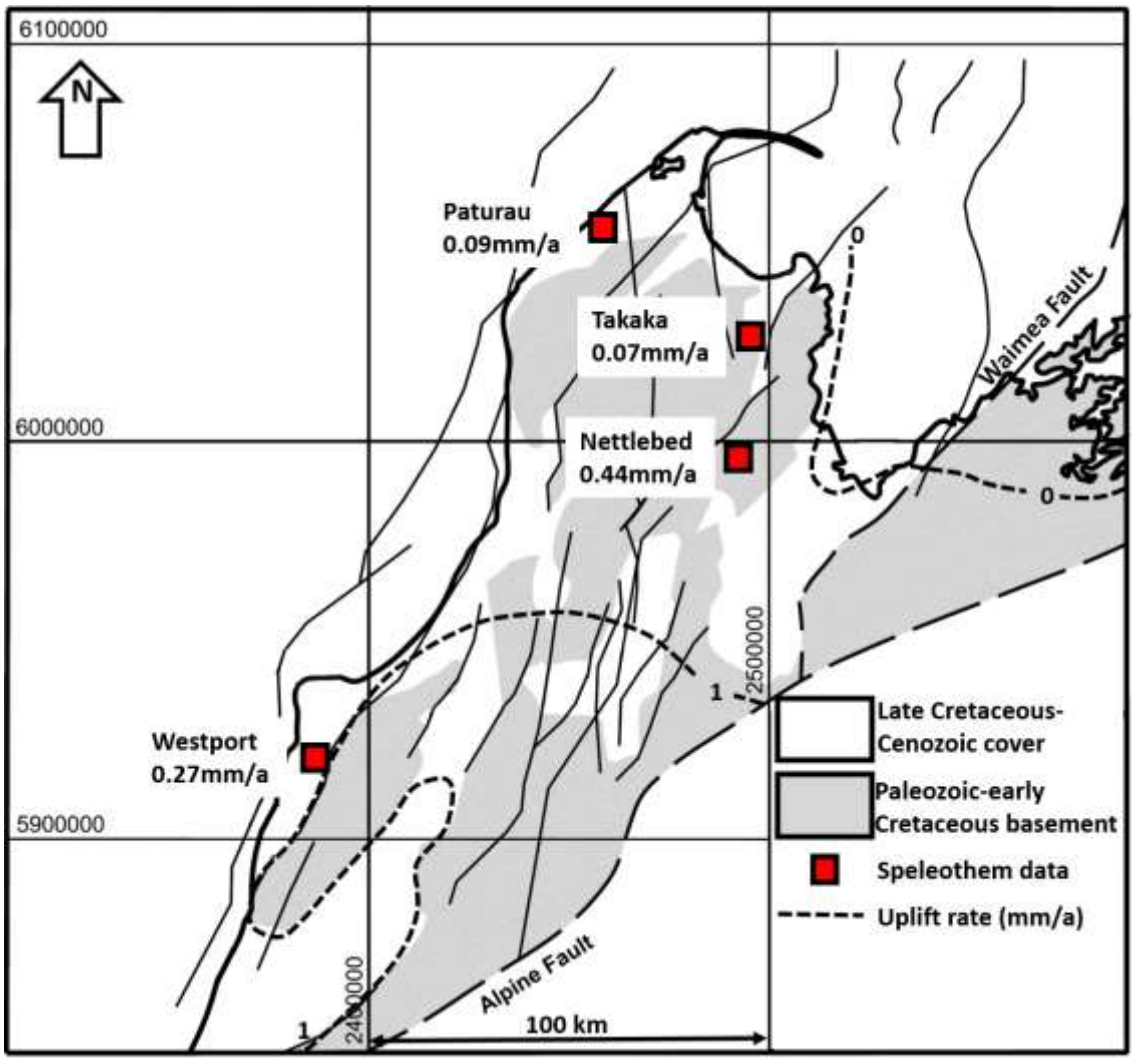

Figure 2.4. Locations of the sites in Northwest Nelson where uplift rates have been calculated using basal dates from speleothems. Speleothem data from Williams (1991). Uplift rate contours from Williams (2017)

These low uplift rates also suggest relative tectonic stability in Northwest Nelson. However, the speleothem-derived uplift rates for Nettlebed, Paturau and Takaka may overestimate the true uplift rate because the speleothems considered are older than the age limit for uranium-series dating, and were inferred to be older than 690ka on the basis that they started growing during a period of reversed geomagnetic polarity

(Lyons, 1983). Further uncertainty in the accuracy of the uplift rates is also due to the fact that speleothems can only start to grow after the cave passages that they occupy have been abandoned by the streams that formed the passages.

Further evidence of low uplift rates during the Quaternary comes from Wetneck Cave in Paturau, where beach gravels that have been washed into the cave have been dated at 1.247±0.427Ma using cosmogenic nuclide burial dating. These gravels are in a part of the cave that is now located about 60m above current sea level (Williams, 2017), suggesting a local uplift rate of 0.05mm/a.

Apatite fission-track ages from sites in Northwest Nelson (figure 2.5) range from 8.6 to 82.5Ma (Seward, 2016 personal communication), and there is a general trend of increasing age in areas distal to the Alpine Fault.

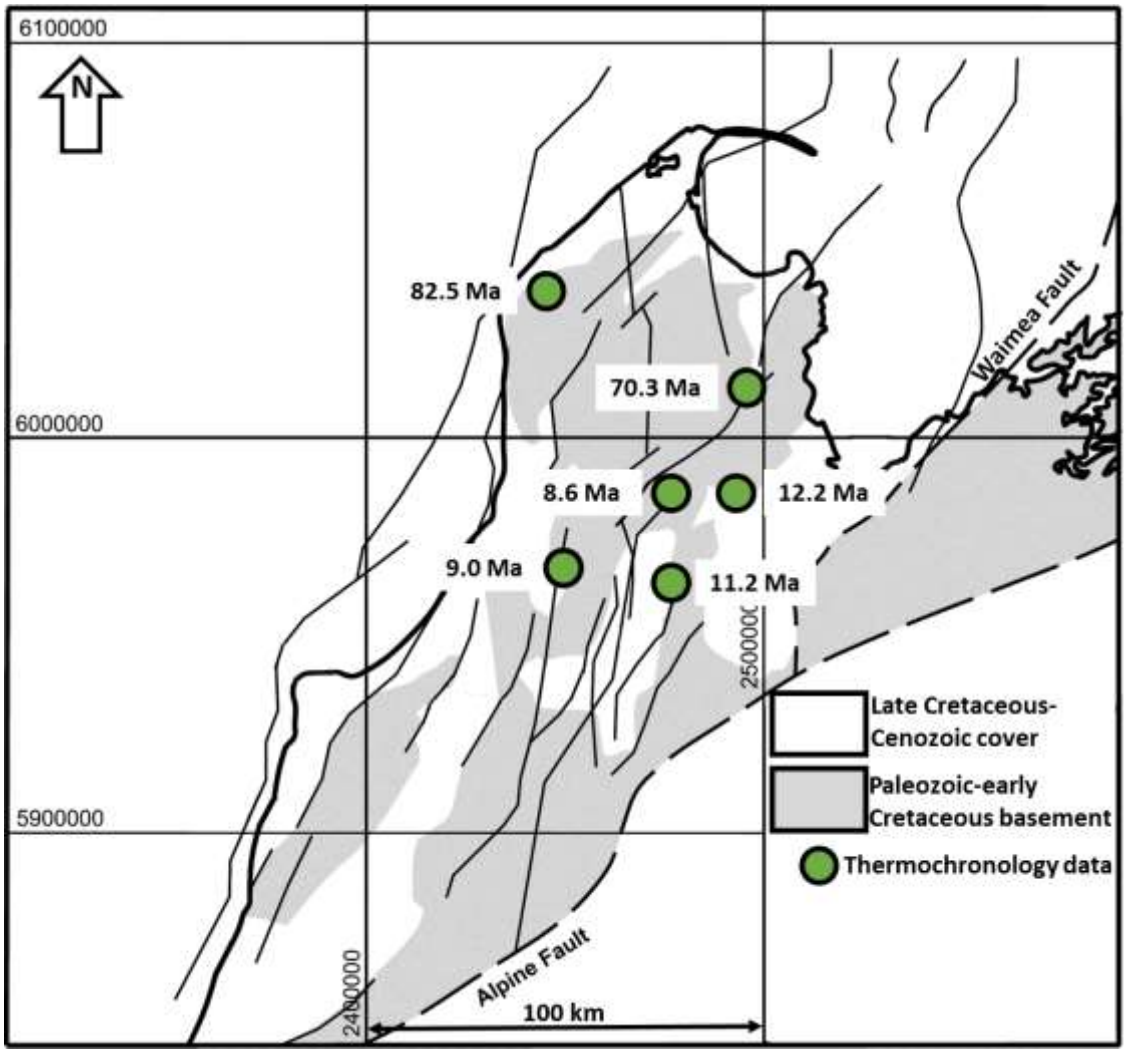

Figure 2.5. Apatite fission-track ages from sites in the Northwest nelson area. Data supplied by Dianne Seward (personal communication).

Apatite fission-track ages record the latest time that the sampled rock was at 120°C. Assuming a geothermal gradient of 25°C/km, which has been used in other studies of uplift in areas proximal to the Alpine Fault (e.g. Seward, 1989), this equates to a depth of approximately 5km. Apatite fission-track ages from sites proximal to the Alpine Fault suggest that uplift rates have not exceeded 0.6mm/a since the late Miocene

2.5 Analysis of the Cenozoic sedimentary basins of Northwest Nelson

The Northwest Nelson area is part of the basin and range province of the western South Island (Williams, 1991). In the southern part of Northwest Nelson, there are two Cenozoic sedimentary basins located north of the Alpine Fault: the Eocene-Miocene Murchison Basin and the Late Miocene-Pliocene Moutere Depression (figure 2.6).

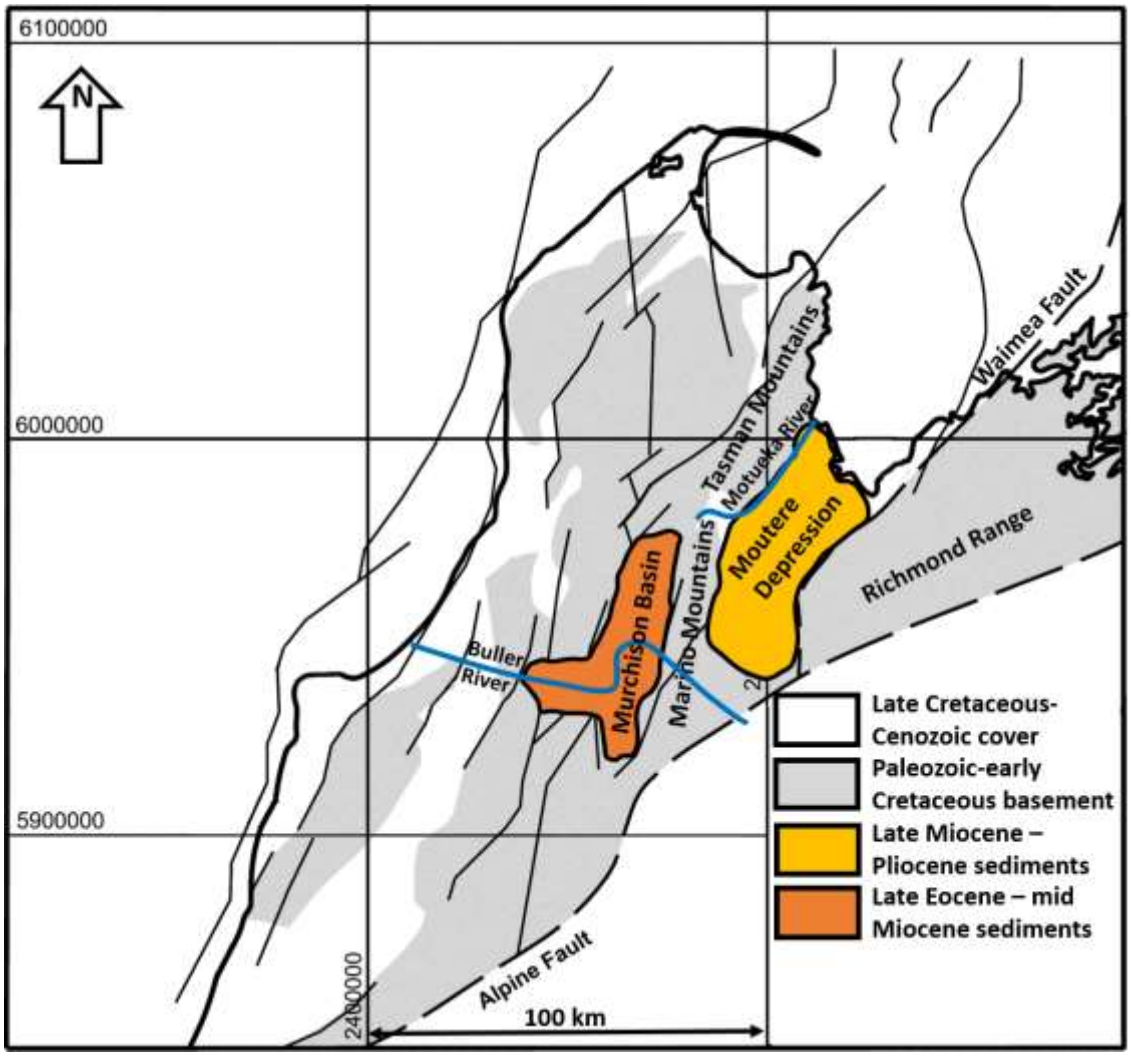

Figure 2.6. Location of the mountain ranges and Cenozoic sedimentary basins of Northwest Nelson.

The basins are separated by the Marino Mountains, which run northwards from the west-draining Buller River Valley to the north-draining Wangapeka-Motueka River Valley, and consist of uplifted rocks of the Western Province. The stratigraphy of the Murchison Basin and the Moutere Depression is summarised in figure 2.7. Analysis of the sedimentary and deformation histories of these basins may provide some insight into the tectonic history of the Northwest Nelson area.

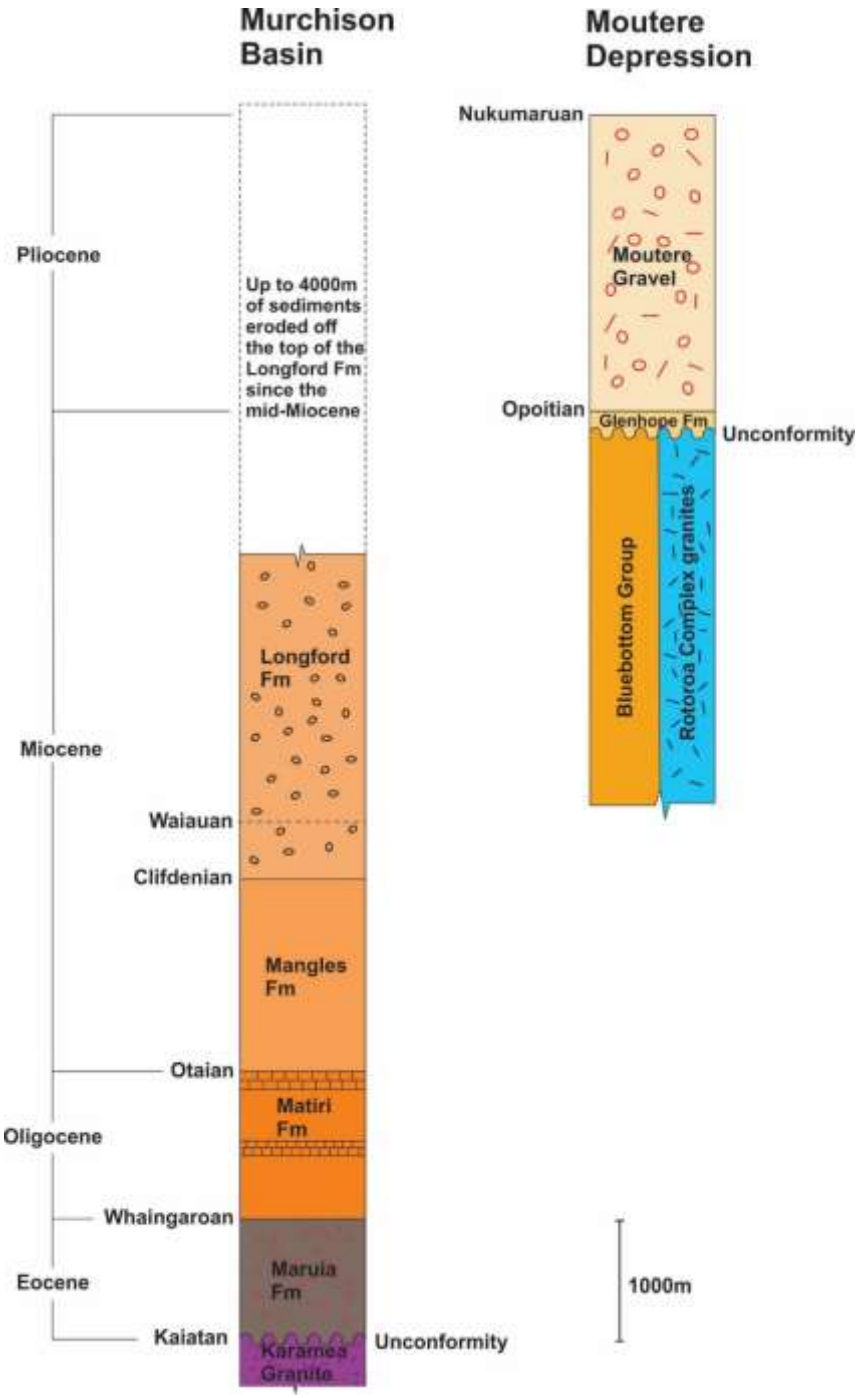

Figure 2.7. Summary stratigraphic columns for the Murchison Basin and Moutere Depression. Compiled from Rattenbury et al (1998, 2006); Suggate (1984); Mildenhall & Suggate (1981).

The Murchison Basin started to form in the Late Eocene, and the infilling sediments record a range of depositional settings ranging from terrestrial to deep marine (Rattenbury et al, 2006). The full sequence of the sediments that infill the Murchison Basin are exposed in the Longford Syncline, which is a south-southwest trending section of the upper Buller River Valley.

The oldest sediments infilling the Murchison Basin are of the Late Eocene to Early Oligocene Maruia Formation (Fyfe, 1968). The oldest units were deposited in terrestrial to marginal-marine settings, and the youngest units were deposited in estuarine to terrestrial settings (Suggate, 1984).

The Maruia Formation is conformably overlain by the 1200m thick Matiri Formation (Fyfe, 1968). The Matiri Formation was deposited from the Late Oligocene to the Early Miocene in a deep open sea setting (Rattenbury et al, 2006), and the presence of limestone members suggests periods of terrigenous sediment starvation.

Conformably overlying the Matiri Formation is the ~1600m thick Mangles Formation. The lowermost unit of the Mangles Formation is of Early Miocene age (Fyfe, 1968) and is made up of turbidite facies that were deposited in a deep water setting. The upper Mangles Formation is a coarsening upwards sequence of sand and mudstones and conglomerates that record a transition from a deep water to a marginal-marine depositional setting. Clast lithology suggests that the uppermost Mangles formation sediments were sourced from rocks of the Eastern Province, located to the east of the Murchison Basin (Suggate, 1984; Rattenbury et al, 2006).

On the eastern margin of the Murchison Basin are outcrops of the Oligocene-Early Miocene glauconitic sandstones and calcareous mudstones and limestones of the Sherry River Formation. An exposure of the Sherry River Formation in the Owen Valley contains a breccia that contains blocks of the Owen and Wangapeka Formations, and Arthur Marble, which are basement terrane rocks, below sediments that are of Otaian age (Coleman, 1981).

The youngest sediment still preserved in the Murchison Basin is the Middle Miocene Hudson Conglomerate, which is the uppermost member of the Longford Formation. The Longford Formation is a 2700m thick succession of conglomerates and

carbonaceous mud and sandstones (Fyfe, 1968). These sediments were derived from areas of Eastern Province rocks to the east of the basin (Suggate, 1984), and deposited in alluvial plain and estuarine settings (Rattenbury et al, 2006). Deposition of the Longford Formation started in the early part of the Middle Miocene during the Clifdenian stage (Suggate, 1984).

Analysis of the tectonic deformation of the sediments that infill the basin suggest that the basin has been shortened by about 50% along the east-west axis of the basin since the deposition of the Hudson Conglomerate during the Waiauan stage (Lihou, 1993), and up to 3000m of sediment may have been eroded off the top of the Longford Formation in this time (Suggate, 1974; 1978). This suggests local erosion rates of up to 0.27mm/a since the Middle Miocene.

The sedimentary record preserved in the Murchison Basin suggests that it started to form in the in the Late Eocene, and had reached maximum depth by the Early Miocene. The shallowing upwards facies succession from the Early Miocene and the presence of large volumes of sediment sourced from areas to the east suggest that the uplift of the southern Northwest Nelson area began sometime in the Early Miocene. However, the presence of coarse clastic material in the Sherry River Formation in the eastern margins of the basin suggest that some parts of Northwest Nelson were emergent during the Late Oligocene. The amount of tectonic shortening across the basin and the amount of material eroded from within the basin since the Middle Miocene suggest a period of rapid uplift in the Northwest Nelson area.

The other large tectonic basin in the southern Northwest Nelson area is the Moutere Depression (figure 2.6). It is also located north of the Alpine Fault, and is bounded to the east by the Richmond Range and to the west by the Tasman and Marino Mountains of Northwest Nelson. The Moutere depression is a half-graben structure that started forming in the Plio-Pleistocene in response to the onset of dextral reverse motion along the Waimea-Flaxmore fault system that makes up its eastern boundary (Rattenbury et al, 1998). Seismic and drill hole data indicate that the Moutere Depression is up to 2500m deep in places, and the basement rocks are dissected by a series of northeast trending reverse faults. Some of these faults appear to propagate up into the infilling sediments (Lihou, 1992). The Moutere Depression has an

antiformal surface topography, with a high central ridge at elevations of about 600m above sea level (asl) in the south, decreasing to about 400m asl in the north. The elevation of the western margins of the Moutere Depression range from about 400m asl in the south to about 300m asl in the north. The eastern margins are at a lower elevation compared to the west, with elevations of about 300m asl in the south and about 200m asl in the north.

Sediments that infill the Moutere Depression are sourced from the surrounding mountains, and were deposited in terrestrial and lacustrine settings (Coleman, 1981). The oldest sedimentary unit that infills the Moutere Depression is the Glenhope Formation. The Glenhope Formation is exposed at Glenhope in the southwestern part of the Moutere Depression, where it has a thickness of up to 150m (Coleman, 1981). It is also exposed in the northwestern part of the Moutere Depression, where the lowermost 20m is exposed at Ngatimoti (Grindley, 1980). The Glenhope Formation can be subdivided into two distinct members. The lower member is deposited unconformably on lower Tertiary and basement terranes, and consists of poorly sorted angular to sub-rounded river gravels. Clast lithology suggests that the sediments were derived from the mountains to the west (Coleman, 1981; Grindley, 1980). The upper member consists of granite-derived sands and silts, with an increasing component of Torlesse terrane derived sandstone towards the top (Coleman, 1981; Rattenbury et al, 2006). Plant microfossils suggest that the Glenhope Formation was deposited during the Late Miocene to Early Pliocene (Mildenhall & Suggate, 1981).

In the south of the Moutere Depression, the Glenhope Formation is conformably overlain by the Moutere Gravels. In northern parts of the Moutere Depression, the Moutere Gravels rest unconformably on basement rocks (Coleman, 1981). The Moutere Gravels consist of rounded large cobble to boulder sized clasts of Rakaia Terrane derived sandstone in a yellow to brown sandy mud matrix. Rakaia Terrane rocks are exposed in the Spenser Mountains, which are located to the south of the Moutere Depression on the southeastern side of the Alpine Fault (Coleman, 1981; Rattenbury et al, 2006). Plant microfossils suggest that the Moutere Gravels were deposited during the Pliocene (Mildenhall & Suggate, 1981).

In contrast to the Murchison Basin, the sediments that infill the Moutere Depression are only weakly deformed. The Moutere Gravels dip to the southeast towards the Waimea Fault by about 2^{o} (Lihou, 1992), and the underlying Glenhope Formation appears to be more strongly deformed (Coleman, 1981), and dip to the southeast by less than 20^{o} (Grindley, 1980). Interpretation of seismic reflection data suggest that there has been no more than 5% shortening across the Moutere Depression since the onset of deposition of the Glenhope Formation, and most of the shortening has taken place along the eastern margin (Lihou, 1992). This amount of shortening is not enough to explain the surface topography of the Moutere Depression. However, it has been suggested that the surface topography is the result of post-deposition deformation of the basement rocks into a structure called the Intra-Moutere Structural High (Ghisetti et al, 2017).

The sedimentary record preserved in the Moutere Depression suggests that the Marino and Tasman Mountains had been uplifted by the late Miocene, and the comparatively small volumes of material deposited imply that uplift rates in the area were lower than during the Early to Middle Miocene. The appearance of large volumes of Rakaia Terrane-derived sediments sourced from areas to the south of the Alpine Fault suggests that uplift rates in parts of Northwest Nelson that were south of the Alpine Fault increased during the Pliocene. However, the relatively weak deformation of the sediments infilling the Moutere Depression suggest a decrease in the rate of convergence in the Northwest Nelson area since the Late Miocene. The fact that the basement penetrating reverse faults in the Moutere Depression do not propagate all the way to the surface may suggest that convergence to the west of the Waimea-Flaxmore fault system ceased sometime in the Late Pliocene or the Pleistocene.

2.6 Timing of activity of the faults of Northwest Nelson

There are a number of northeast-southwest trending faults in Northwest Nelson that show evidence of activity since the inception of the Austro-Pacific plate boundary in the Eocene (Rattenbury et al, 1998). Analysis of the lithostratigraphic units that they crosscut may constrain the timing of activity in these faults.

The geological map of Northwest Nelson (figure 2.8) shows up to 7km of dextral motion along the Karamea and Skeet Faults, which are the major faults that cut across the western ranges of Northwest Nelson.

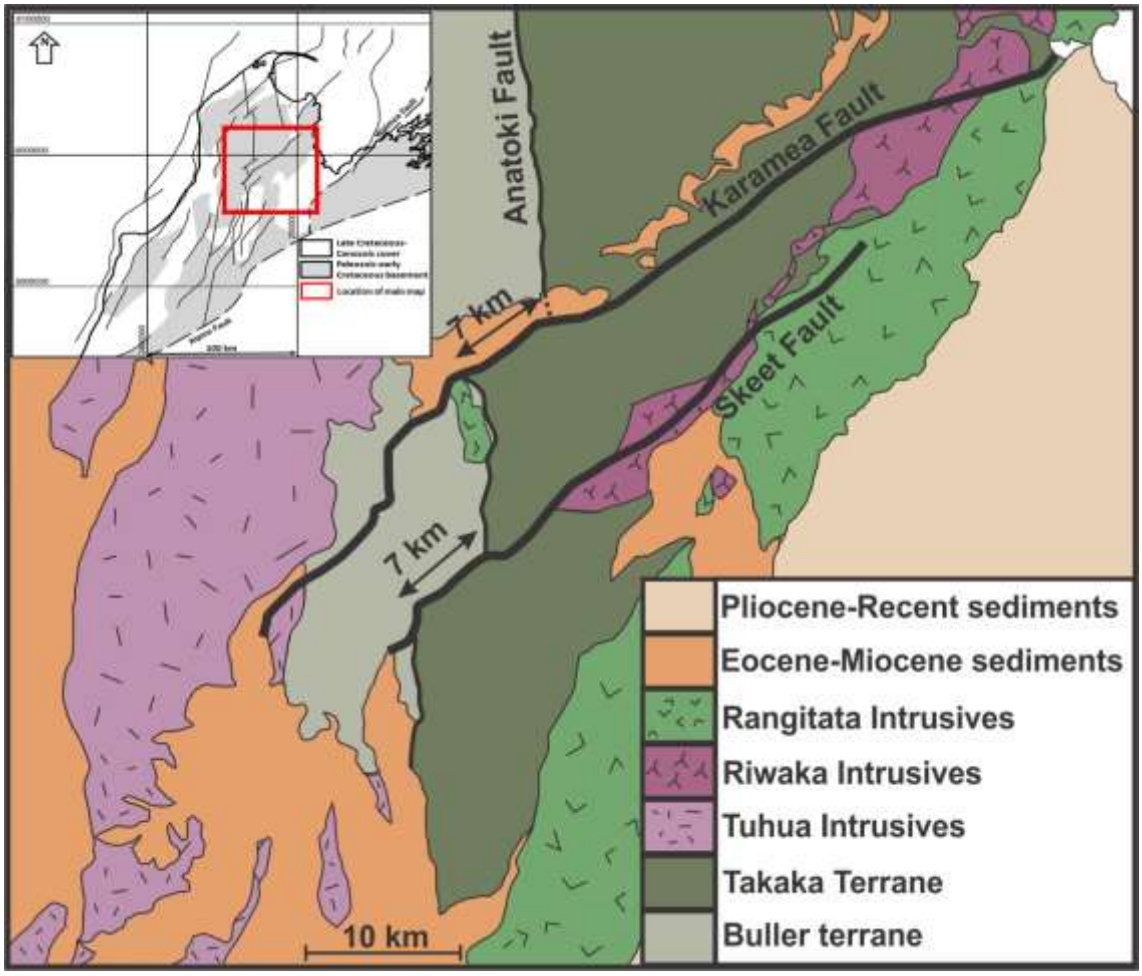

Figure 2.8. Simplified geological map of Northwest Nelson showing the locations of the main faults that crosscut the ranges of Northwest Nelson. Modified from Rattenbury et al (1998). Inset map shows the location of the main map.

The youngest stratigraphic unit that these faults crosscut is the Early to Middle Miocene Lower Bluebottom Group, and the oldest units that are not deformed by the faults are Marine Isotope Stage (MIS) 6 river gravels (Rattenbury et al, 1998), suggesting that most of the displacement has occurred from the Middle Miocene and ceased by the Late Pleistocene. However, microearthquakes, the presence of Late Quaternary fault traces on the Karamea Fault and the geomorphology of the Moutere Depression suggest that there is still some ongoing tectonic activity in the area (Grindley, 1980; Ghisetti et al, 2017).

The timing of the onset of motion on the Karamea and Skeet faults is consistent with the timing of deformation in the Murchison Basin. Because the Karamea and Skeet

faults do not crosscut the sediments in the Moutere Depression, they tell us very little about the timing of sedimentation or deformation in the Moutere depression.

2.7 Summary

All of the published uplift rates considered are averaged over long timescales and indicate relative tectonic stability in the Northwest Nelson area compared to other areas that are close to the Austro-Pacific plate boundary. However, the presence of large volumes of relatively young sediments in the basins of Northwest Nelson suggest that there were periods of rapid uplift in the area since the inception of the plate boundary in the Eocene.

Knowledge of the timing and rate of uplift in the Northwest Nelson area is significantly limited by the fact that the timing of sediment deposition and fault movement in the area are poorly constrained. Furthermore, the effects of erosion means there are lots of gaps in the record, and most of the very sparse uplift rate data are from areas that are distal to the Alpine Fault.

If sites with suitably preserved sediments such as cave systems could be identified in the Northwest Nelson area that are proximal to the Alpine Fault, then cosmogenic nuclide burial dating, which can give absolute and reasonably precise dates may offer a new way of quantifying the timing and rate of uplift in the area, especially for the time period between the onset of uplift and deformation of the Murchison Basin and the onset of sedimentation in the Moutere Depression.

Chapter 3: Introduction to the study area

3.1 Location of the study area

The study area is located on the Mt. Owen massif, which is located at the southern end of the Marino Mountains of southern Northwest Nelson. The Mt. Owen massif is approximately 30km northwest of the Alpine fault, which is closer to the fault than other sites in the Northwest Nelson area that have been used to reconstruct uplift rates (figure 3.1). The proximity of the study area to the Alpine fault may allow for the determination of whether uplift rates have been constant across the Northwest Nelson area or if there is a trend to increasing uplift rates with proximity to the Alpine Fault as suggested by the data published by Williams (1991; 2017).

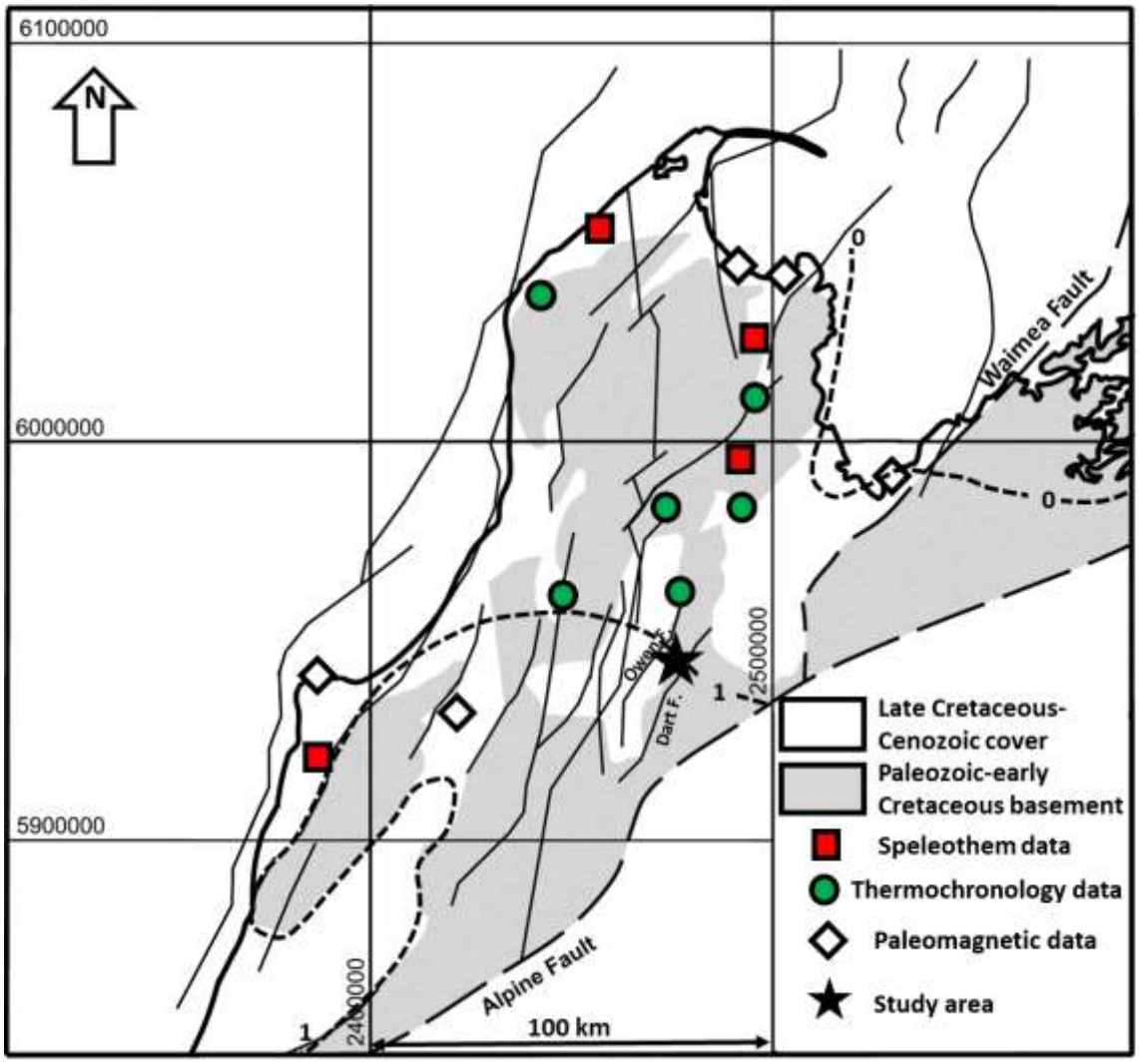

Figure 3.1. Location of sites in the Northwest Nelson area where data that provides information on the uplift history of the area has been collected and the location of the study area.

The Mt. Owen massif is a block of Takaka Terrane rocks that have been upthrust between the north-northeast trending Owen and Dart Faults (Coleman, 1981).The Mt. Owen massif has a total area of approximately 77km^2, of which approximately 35km^2 is above the tree line. It is bounded to the south by the Owen and Fyfe rivers, which are tributaries of the Buller River, and to the north by Nuggety and Granity creeks, which are tributaries of the Wangapeka River. The highest point of the massif is Mt. Owen, at 1875m asl, and there are a number of other peaks that are higher than 1500m asl. The higher parts of the massif show evidence of extensive glaciation since the late Quaternary, with cirque basins and u-shaped valleys radiating out from the summit area (Hyatt et al, 2007; Williams, 2017).

The geomorphology of the northern part of the Mt. Owen massif is characterised by a number of peaks surrounding a central basin area, which is drained by north flowing surface streams (figure 3.2).

Figure 3.2. View from the summit of Mt Owen looking north. The high point in the middle distance is Culliford Hill, which is the highest point of the northern part of the massif. The prominent high point in the left background is Mt. Patriarch, which is located to the north of the Wangapeka River.

Some of these streams flow along the surface into the head of Blue Creek while others sink underground. Dye tracing indicates that the sinking streams also are a part of the Blue Creek catchment (Williams, 2017). The southern part of the massif is characterised by expansive areas of bare karst, closed basins and overdeepened glacial valleys (figures 3.3 and 3.4), and there is no surface drainage.

Figure 3.3. View from the summit plateau looking southeast.

Figure 3.4. View looking south from the summit plateau down Castle Basin. The lowest point of the basin is about 50m lower than the southern wall. The floor of the basin is pocked with suffusion dolines and roche mountonees.

In addition to the surface drainage, there are 4 major resurgences that drain the Mt. Owen massif (figure 3.8). Two drain to the south, one is located at the head of Bulmer Creek, and the other is in an unnamed tributary of the Fyfe River. The resurgences that drain to the north are located in Nuggety and Blue creeks.

The Mt. Owen massif is considered to be the best example of glaciated karst in New Zealand (Williams, 1992), and is also the location of some of the longest and oldest caves known in New Zealand. The northern parts of Mt. Owen have been a focus of cave exploration since the 1960s, where a number of significant caves were discovered and explored. Due to its remoteness, there was very little exploration of the southern part of Mt. Owen until the mid-1980s (Patterson, 1988).

3.2 Geology of the Mt. Owen massif

The main lithology of the Mt. Owen massif is the early to middle Ordovician Arthur Marble (Ma, figure 3.5), which is part of the Takaka terrane, and consists of recrystallized micritic limestone that varies in colour from light grey to black. In places, there are bands or nodules of siliceous material. The Arthur marble is severely deformed, and outcrops to the northwest of Mt Owen show recumbent isoclinal folding. In the Mt Owen area, the Arthur Marble is thought to be about 1500m thick (Rattenbury et al, 1998; Coleman, 1981).

Conformably underlying the Arthur Marble is the latest Cambrian to early Ordovician limestones, mudstones and sandstones of the Owen Formation (Mn). The Owen Formation is exposed on the lower parts of the southeastern corner of the massif (Coleman, 1981; Rattenbury et al, 1998). There are also some isolated outcrops of the Owen Formation exposed on the high ridges on the southern part of the massif (L. Main, 2018, personal communication).

The Arthur Marble is overlain by the late Ordovician to early Silurian Wangapeka Formation (Mw). The Wangapeka Formation is only exposed on the Mt. Owen massif in the floors of the basins and on the true left of the Fyfe River, where it appears as weakly deformed thin-bedded grey to black carbonaceous silt and sandstones and occasional quartzite beds Coleman, 1981; Wopereis, 1988).

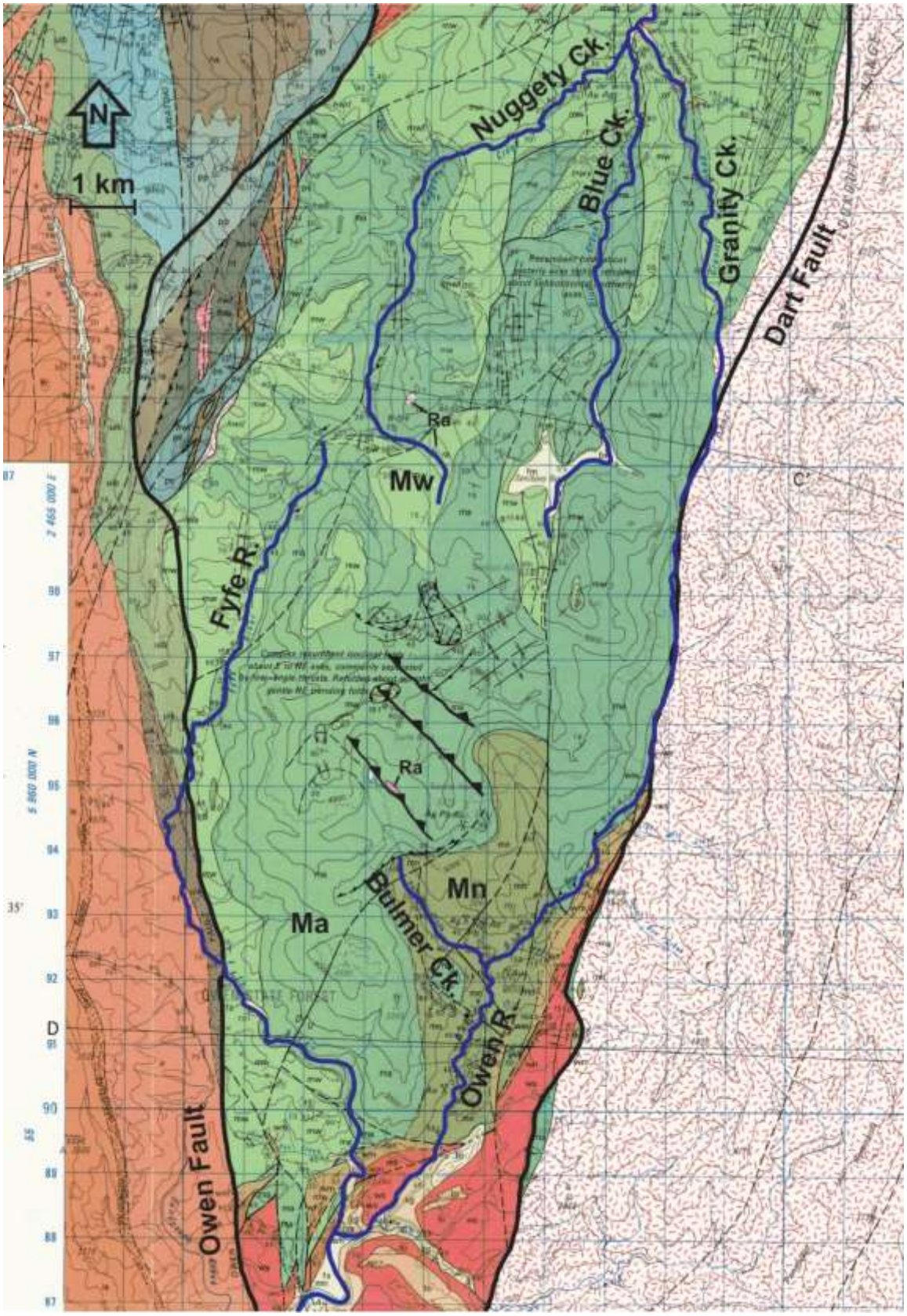

Figure 3.5. Geological map of the Mt.Owen massif showing the main faults and waterways that define the massif and the lithologies exposed on the massif. Modified from Coleman (1981). Mn = Owen Formation, Ma = Arthur Marble, Mw = Wangapeka Formation, Ra = Riwaka Intrusives.

There are also small outcrops of Riwaka Intrusives (Ra) on the Mt. Owen massif. Two outcrops of hornblende andesite are located on the north of the massif in the headwaters of Nuggety Creek, and a thin sill of green dolerite is exposed on the south side of Mt. Owen in the headwaters of Bulmer Creek (Coleman, 1981; Wopereis, 1988).

The southern part of the Mt Owen massif is dissected by a series of northwest-southeast trending thrust faults that dip to the northeast.

3.3 Vegetation and climate

Because of the remoteness of the area, there are very few formal climate records for the Mt. Owen area. Rainfall measurements in the Wangapeka valley for the period 1941 to 1970 indicate mean annual rainfall of 1771mm, slightly higher than for the town of Murchison, located 35km to the southwest which recorded 1558mm/a for the same period (NZMS, 1973). Rainfall measurements in the Wangapeka valley stopped when the recording station was decommissioned in the early 1970s. Computer modelling suggests mean annual rainfall of up to 2500mm on the massif (Burdis, 2014).

Informal temperature readings taken at Granity Pass hut in the northern part of the Mt. Owen massif indicate summer temperatures in the range of -1^{o}C to 26^{o}C and a winter temperature range of -5^{o}C to 10^{o}C (Bell, 1970). Measurements of air temperature in Bulmer Cavern over a number of years show that it is constant throughout the year at about 4^{o}C. Because cave air temperature is a good approximation of mean annual external air temperature (Ford & Williams, 2007), annual mean temperatures on the higher parts of the massif are likely to be around 4^{o}C.

At the southern end of the Mt. Owen massif, the tree line is at approximately 1200m asl, and it rises to about 1300m asl at the northern end. The vegetation above the treeline is predominantly sub-alpine scrub and alpine tussock grassland with occasional herbs and shrubs. Common species include *Chionochloa spp., Poa colensoi, Festuca novae-zelandiae, Veronica (Hebe) spp., Celmisia spp.* (Wardle, 1991). At the treeline, the vegetation is mostly open beech forest, with Silver Beech (*Lophozonia menziesii*)

being the dominant species. Trees become progressively more stunted as the tree line is approached.

In the Owen Valley and the lower parts of Bulmer Creek, the vegetation is beech forest, with Black Beech (*Fuscospora solandri*) being the dominant species that forms the canopy. The understory is made up of beech seedlings, shrubs (e.g. *Coprosma spp., Pseudopanax spp., Aristotelia serrata, Pseudopanax crassifolius)* and ferns (e.g. *Cyathea spp., Blechnum spp.*). Tall podocarp species (e.g. *Dacrydium cupressinum, Prumnopitys spp., Podocarpus spp.*), which are rare in the inland parts of Northwest Nelson, especially above altitudes of 640m asl (Wardle, 1991) are not present. However, occasional specimens of Thin-barked Totara (*Podocarpus laetus*) can be found in the area (A. Shanks, 2018, personal communication).

3.4 Introduction to speleogenesis

3.4.1 Sources of groundwater in karst terranes

Water that infiltrates karst-forming rocks eventually makes its way down to the water table. If the infiltrating water is sourced from rainfall that falls entirely on the surface of the karst terrane, then the system is autogenic, Autogenic karst-aquifer systems are characterised by diffuse recharge that is distributed across the surface of the karst (figure 3.6a). An autogenic system may also have multiple resurgences distributed in a radial pattern around a block of karst.

If the infiltrating water is sourced from runoff from surrounding non-karst terranes, the system is allogenic. Allogenic karst-aquifer systems are characterised by point recharge where surface streams flow onto a karst terrane and then sink (figure 3.6b). An allogenic system can have a much larger catchment compared to an autogenic system. This means that streams in an allogenic system are more likely to transport large volumes of coarse sediments deep into the system than the streams in autogenic systems (Ford & Williams, 2007).

Most real-world karst-aquifer systems have both an autogenic and an allogenic component (figure 3.6c), and are called mixed karst-aquifer systems. Bulmer cavern is an example of a mixed system.

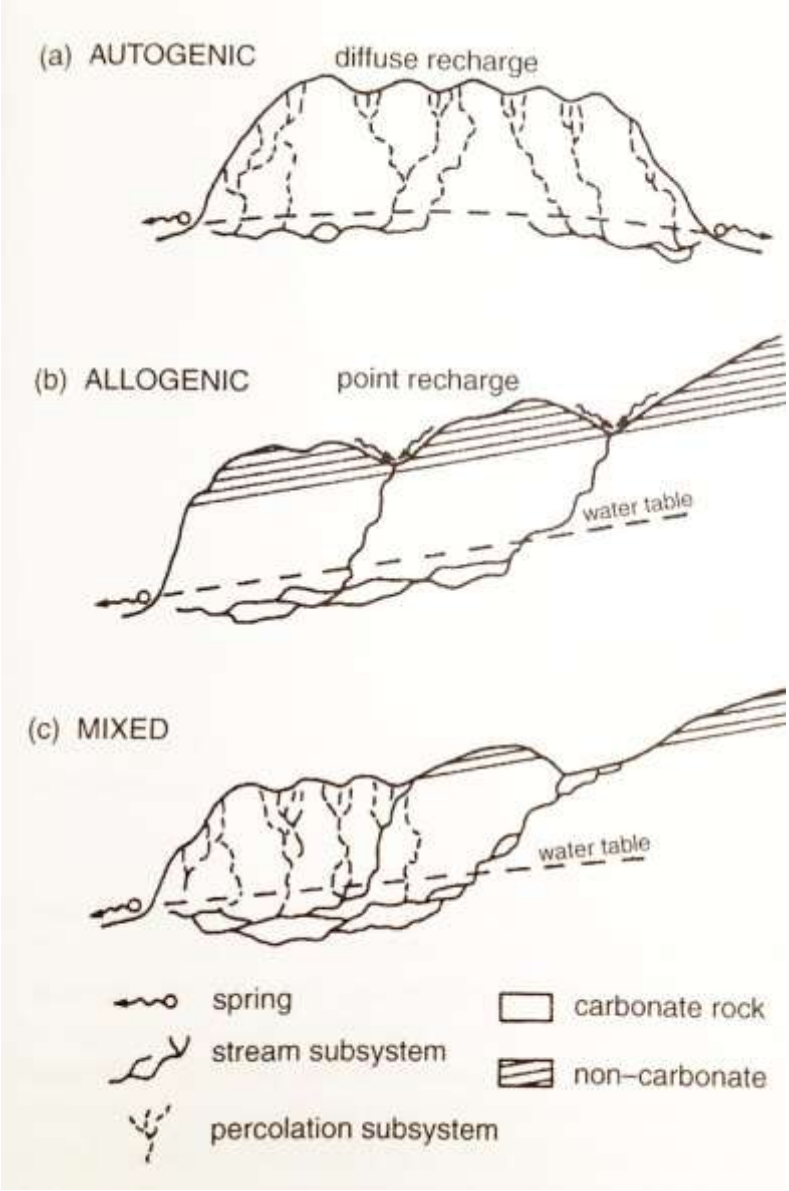

Figure 3.6. The three styles of karst-aquifer system. Ford & Williams (2007).

3.4.2 Development of cave passages

Because karst-forming rocks such as limestone and marble are slightly soluble in water (~60mg of rock/litre of water, Ford & Williams, 2007), fissures in the rock get widened by solution, and eventually link up to form cave passages.

There are two styles of cave passage development, phreatic development and vadose development. Phreatic development occurs by solution when cave passages are below the water table, and result in the formation of rounded tubes. Because phreatic development occurs below the water table, uphill development of cave passages is possible.

Vadose development occurs when cave passages are above the water table, resulting in the formation of canyons. Vadose development occurs in an open channel setting that is similar to the development of surface streams, so downward development by incision of the stream into the host rock is the dominant mechanism of development. Because physical erosion is a significant component of vadose development, cave passage development can continue down into underlying non-karst rocks. Vadose development can also occur by solutional processes such as condensation corrosion, which can enlarge passages at rates of up to 0.2mm/a (Dreybrodt, 2003) or by physical processes such as breakdown, where mechanical stress causes blocks of material to exfoliate off the walls or roof of the passage. Breakdown and condensation corrosion can continue until the passage daylights or becomes completely filled with rubble.

There are a number of stages in the development of a phreatic tube (figure 3.7). The first stage is inception, where ground water percolates along joints, faults or bedding planes. In karst forming rocks, this leads to the formation of small conduits up to 15mm wide over a timescale of 3-5ka during the initiation stage. During the inception and initiation stages, groundwater flow velocities are very low and the water is close to saturation with respect to calcium carbonate, resulting in low dissolution rates (Klimchouk, 2004; White, 1988).

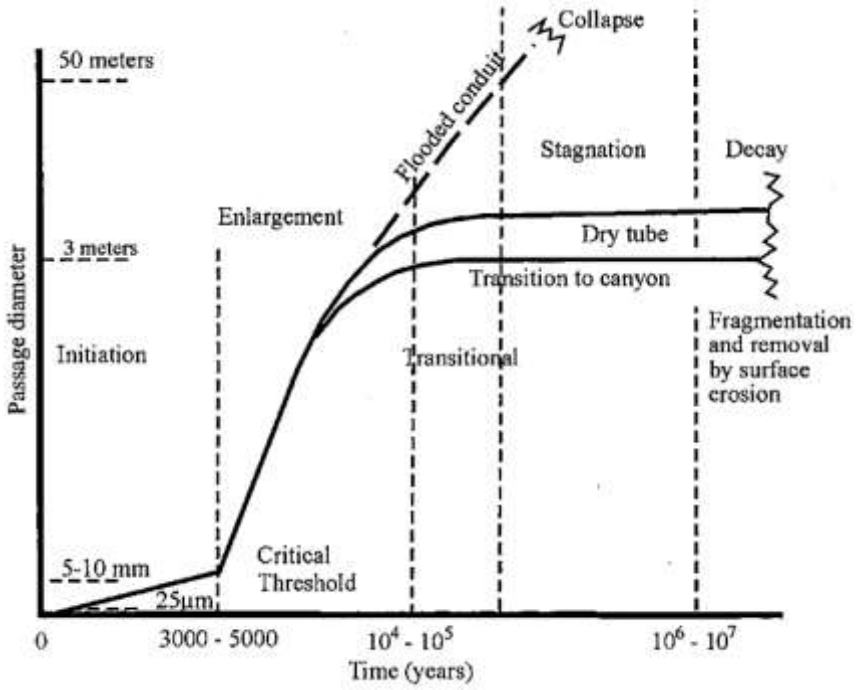

Figure 3.7. Stages in the evolution of a phreatic tube. White (1988).

When the tube reaches about 15mm in diameter, groundwater flow through the tube increases, and the water is less saturated with respect to calcium carbonate. This results in greatly increased dissolution rates, and the enlargement of the passage at rates of 0.1-1mm/a during the early development or enlargement stage. Depending on groundwater chemistry and flow regimes, it can take as little as 10ka or as much as 100ka for the tube to grow to about 3m in diameter (Klimchouk, 2004; White, 1988). The enlargement stage can continue until the passage encounters insoluble strata or the passage is drained, usually by the lowering of the water table in the karst-aquifer system.

Lowering of the water table can result in the partial or complete draining of the tube. Complete draining leaves a dry (fossil) tube, and partial draining (or draining and later partial reflooding) results in the transition from a tube to a canyon during the stagnation stage which can last anywhere between 100ka and 10Ma (Klimchouk, 2004; White, 1988). When a cave passage is drained, any sediment transported into the passage by the stream that formed the passage becomes fixed relative to the host rock in the karst-aquifer system, therefore allowing the use of burial dating to calculate rates of water table lowering.

The final stage in the development of a cave passage is the decay stage, where the passage becomes too big to support itself and collapses, or is removed by surface erosion (Klimchouk, 2004; White, 1988).

3.5 The caves of southern Mt. Owen

There are two major cave systems located in the southern part of the Mt. Owen massif (figure 3.8). Bohemia cave is currently New Zealand's 8th longest and 5th deepest cave (Main, 2017) and was discovered and explored in the 1990s (Tasler et al, 1991; Tasler, 1998). Bohemia Cave runs southwest from its entrance at the head of Bulmer Creek, and the streams in the cave are the probable source of the resurgence in the Fyfe River. Bohemia cave is currently not thought to be related to Bulmer cavern. The second major cave system in the southern part of the massif is Bulmer Cavern. Bulmer cavern was discovered in 1985 (Patterson, 1988), and has been a focus of ongoing exploration since.

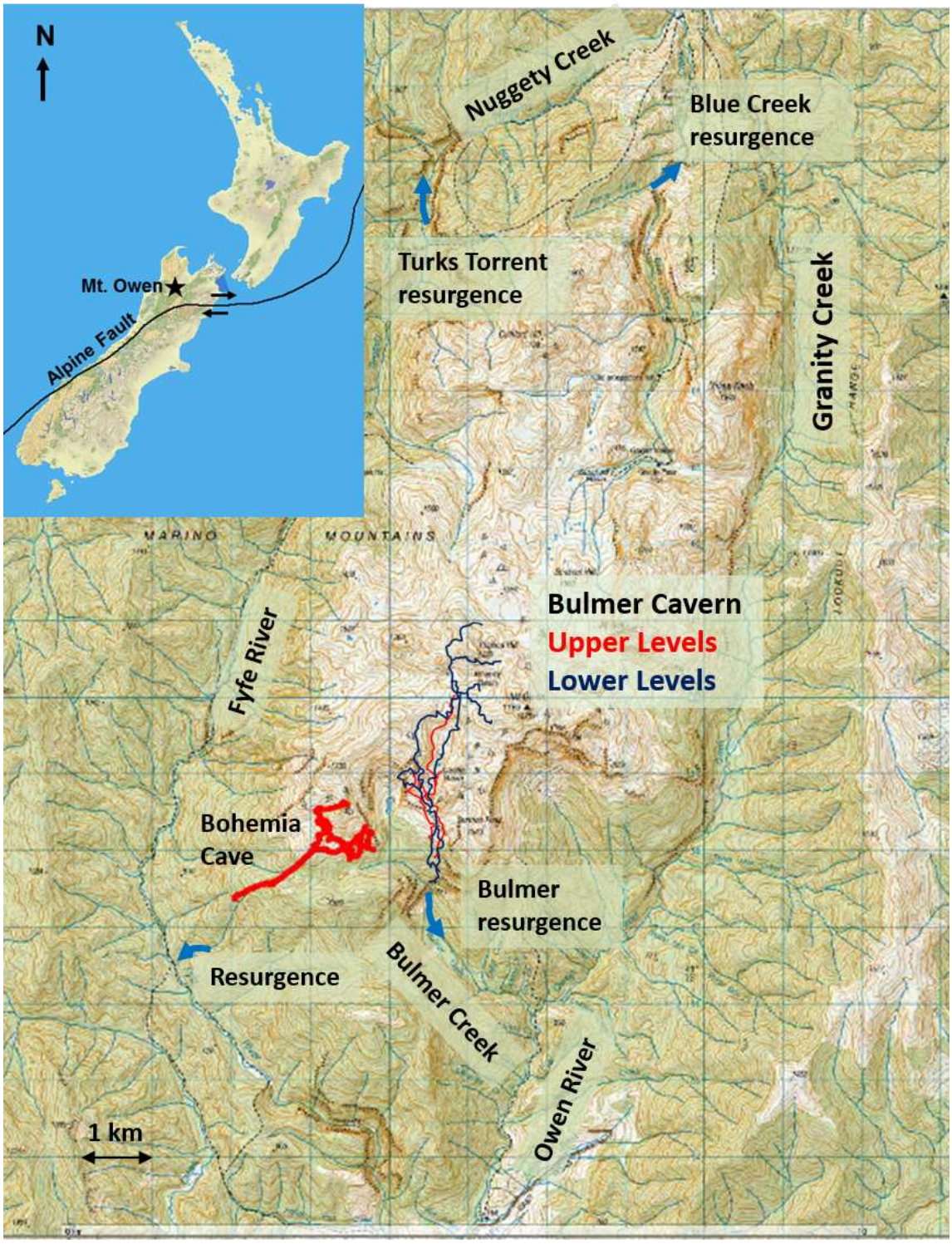

Figure 3.8. Location of the resurgences that drain the Mt. Owen massif. Also shown are the locations of the rivers that define the boundaries of the massif and the major cave systems of Mt. Owen. Basemap: LINZ Topo50

Bulmer cavern is currently New Zealand's longest (72km) and 3rd deepest (755m) cave (Main, 2017), and runs northwards from multiple entrances above the head of Bulmer Creek under the western flank of Mt. Owen (figure 3.9).

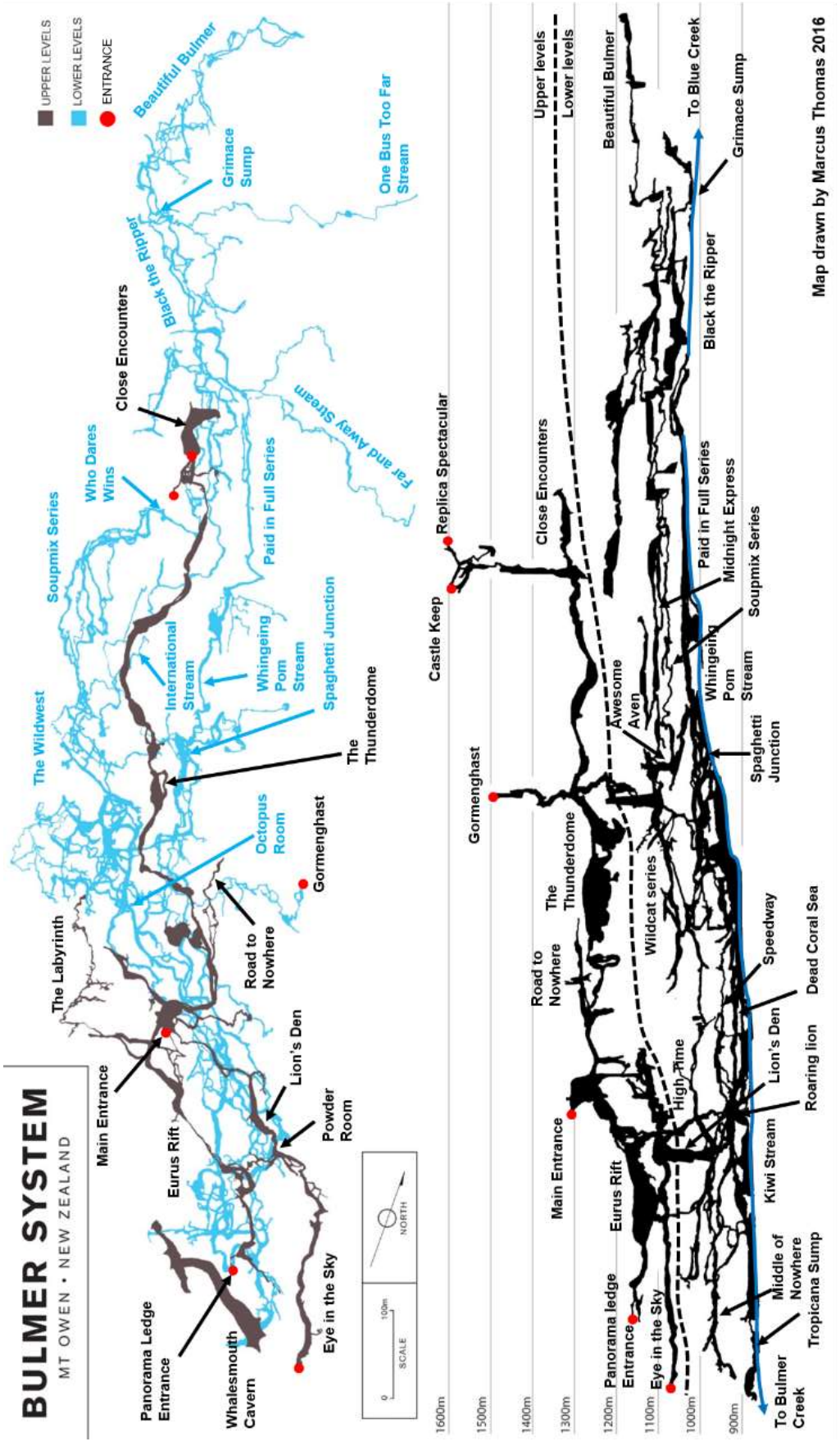

Figure 3.9. Overview map of Bulmer Cavern. Map supplied by Marcus Thomas (personal communication).

The highest known entrance is located on the saddle that separates Castle and Poverty basins at an elevation of 1620m asl, and the lowest part of the system is at about 850m asl. The cave system has developed over at least 6 different levels, and is subdivided into the upper levels and the lower levels. This subdivision was based on the order of discovery and perceived age of the passages that make up the upper and lower levels.

3.6 The Upper Levels of Bulmer Cavern

The highest part of the Upper Levels is the relatively short section of passage that connects the Castle Keep and Replica Spectacular entrances. The passage is round to oval in cross section, and is about 5m wide (figure 3.10).

Figure 3.10. The Castle Keep Passage.

In places there are deposits of rounded river gravels. The southern section of the Castle Keep Passage has developed along one of the prominent northeast dipping thrust faults that dissect the southern part of the massif, and can be followed northwards down dip for about 50m until it intersects a southwest dipping bedding

plane. The passage then continues up dip along this bedding plane for another 60m to the Replica Spectacular Entrance, which is located in the side of a doline on the saddle between Castle and Poverty Basins. From the lowest point of the passage, a series of small canyons lead down to the top of a 250m deep shaft series that connects the Castle Keep passage to the main Upper Levels Passage. The main Upper Levels Passage has a keyhole-like structure with a large (up to 20m diameter) roof-tube that has a deep canyon incised into the floor that is up to 100m deep in places. The Upper Levels Passage can be followed continuously from the Panorama Ledge Entrance northwards for about 2.5km to the Close Encounters Chamber, where it is truncated abruptly by a fault plane. The Panorama Ledge Entrance is located in the side of a bluff above the head of Bulmer Creek, and is accessed from inside the cave via a small side passage off the main passage (figure 3.11).

Figure 3.11. The Panorama Ledge Entrance to the main Upper Levels Passage of Bulmer Cavern.

The main Upper Levels Passage intersects the Main Entrance Chamber, which has also developed on one of the northeast dipping thrust faults that dissect Mt. Owen (figure 3.12).

Figure 3.12. Main Entrance of Bulmer Cavern. The thrust fault that the entrance has developed on can be seen on the right side of the picture

About 50m south of the Main Entrance, a series of steeply descending canyons lead down to a series of small stream passages called The Labyrinth and the Colonial Streamway, that were until very recently considered to be the deepest parts of the Bulmer system.

About 200m north of the Main Entrance, the passage splits. The right hand branch is considered to be a side passage, and can be followed for about 300m along a passage called the Road to Nowhere, until it ends in a sediment choke. The main passage continues northwards to a large chamber called The Thunderdome. The Thunderdome is about 70m long and 30m wide at its widest point, and can be divided into two levels. The lower level is canyon-like and has a rubble floor. The upper level is tube-like and the walls are well decorated with crystal flowers called anthodites (figure 3.13).

Figure 3.13. Small anthodites decorating the wall of a passage in the Upper Levels of Bulmer Cavern.

A side passage off the upper level called The Cobble Passage contains a deposit of well-rounded river gravels. From The Thunderdome, the main Upper Levels Passage continues northwards to the even larger Close Encounters Chamber, where it is terminated by a fault (figure 3.14).

Figure 3.14. The Close Encounters Chamber. The fault that terminates the passage is in the background.

The lowest part of the Upper Levels is the Eye in the Sky Passage, which runs northwards from the Eye in the Sky Entrance for about 1.4 km, where it ends in a sediment choke. The southern part of the passage is a large (up to 20m diameter) tube with a rubble strewn floor. The northern part has a keyhole structure, with a roof-tube up to 10m in diameter and a canyon that is up to 30m deep in places. Parts of the canyon are infilled with sediments that are up to 10m thick. At the northern end, the tube is about 10m in diameter (figure 3.15), tapering down to about 2m at the sediment choke.

Figure 3.15. The northern end of Eye in the Sky Passage.

The Eye in the Sky Passage can be accessed from the Eye in the Sky Entrance or by a series of small tubes and canyons that lead off the southern end of the main Upper Levels Passage, and join the Eye in the Sky Passage at the Powder Room. The Eye in the Sky Passage can also be accessed by abseiling down the canyon in the main Upper Levels Passage at a point about 100m north of the Main Entrance. About 50m north of the Powder Room is a 100m deep shaft series called The Lion's Den, which is the main connection between the Upper Levels of Bulmer Cavern and the Lower Levels.

All of the passages in the Upper Levels are either completely dry or have only small ephemeral streams that flow for short distances before disappearing into very small canyons.

The structure of the Upper Levels indicates alternating phases of phreatic and vadose development (Main, 1988). It has been suggested that the phreatic development occurred during periods of tectonic stability in the Northwest Nelson area, and the vadose development occurred during periods of uplift, and the alternating phases of development in the Upper Levels indicate that the uplift history of Northwest Nelson was episodic, with at least 3 distinct events since the formation of the cave (Main, 1988).

On the basis that all of the Upper Levels passages slope downhill to the south, the presumed paleodrainage direction was from north to south, and because the main Upper Levels Passage and the Eye in the Sky Passage tubes are of remarkably consistent size Main (1988) suggests the catchments that fed these passages were located several kilometres to the north. The size and linear layout of the large passages in the Upper Levels indicate that they were fed by a large catchment that entered the system at a single point, which is typical of an allogenic karst-aquifer system.

The sediments that infill the Cobble Passage and the Road to Nowhere contain clasts of dolerite (Wopereis, 1988) and do not contain any Torlesse Terrane-derived greywake (Main, 1988). This suggests that they are contemporaneous with the Glenhope Formation, and therefore the main Upper Levels passage is of at least Late Pliocene age.

Typical speleothems such as stalagmites, stalactites and flowstone are rare in the upper levels. The most common speleothems are cave coral and crystal flowers, which coat the walls in some parts of the upper levels. In the main Upper Levels Passage just north of the main entrance chamber there are some exceptionally large (up to 1m long) helictites. At the start of the Eurus Rift section of the main Upper Levels Passage, there are a number of partially decayed stalagmites growing on sediment deposits. X-ray diffraction analysis of samples of these stalagmites show that they are composed mostly of aragonite, which is unusual for caves in New Zealand (Main, 1988).

Paleomagnetic dating show that they started growing during a period of normal geomagnetic polarity, and uranium- series dating indicates that some are older than 350ka, which was the age limit for uranium-series dating at the time (Lyons, 1988). Because the sediments had to be deposited before the speleothems could start growing, and paleomagnetic dating indicates that speleothem growth did not start prior to 690ka, there is a time break of at least 2Ma between the abandonment of the main Upper Levels Passage by the stream that formed it and the onset of speleothem growth.

3.7 The Lower Levels of Bulmer Cavern

In contrast to the Upper Levels of Bulmer cavern, which have a relatively simple linear layout of north-south trending passages, the Lower Levels show much more complex development. The Lower Levels can be subdivided into two distinct series on the basis of direction of drainage of the base level streams. The Southern Series drains to the south, resurging at the head of Bulmer Creek, and the Northern Series drains to the north. The base level stream in the Northern Series has been dye traced to the Blue Creek Resurgence, which is located about 8km to the north of Bulmer Cavern (Thomas & Silverwood, 2016). Because this project is focused on the oldest parts of Bulmer Cavern, only the Southern Series will be considered in detail in this section, as the south draining passages are thought to represent the earliest phases of development of Bulmer Cavern (Main, 1988).

3.7.1 The Southern Series

The Southern Series of Bulmer Cavern can be divided into at least 4 levels on the basis of elevation above the lowest level of the cave. The lowermost level is a large active stream passage that is considered to be the base level stream, and is accessed from the Eye in the Sky Passage by descending the Lion's Den and a steeply descending narrow canyon called Castration Corridor. The stream, called the Kiwi Stream flows to the south and is up to 3m wide in places. The passage is keyhole shaped, with a roof-

tube up to 20m in diameter and a canyon that varies in width from 3m to 20m, and is up to 30m high in places (figure 3.16).

Figure 3.16. The Kiwi Stream Passage, lower levels of Bulmer Cavern. The photo was taken looking upstream and the stream is about 3m wide at this point.

The Kiwi Stream can be followed downstream from the intersection with Castration Corridor at a place called the Roaring Lion for about 1km before it disappears into the terminal sump at Tropicana. The Kiwi Stream is believed to be the source of the stream in the Bulmer Resurgence Cave (McKay, 1990). The Kiwi Stream can be followed for about 2km upstream from the Roaring Lion until it splits. The true left branch is called the Whingeing Pom Stream, and can be followed upstream for about 300m to a sump. The true right branch is called the International Stream, and can be followed upstream for about 700m to a sump.

The next level up from the base level stream passages is called the Dead Coral Sea. The Dead Coral Sea is accessed by climbing up from the Roaring Lion, and can be followed northwards for about 2km to a very complex part of the cave called Spaghetti Junction.

The Dead Coral Sea varies from tube-like, with a diameter of up to 10m to canyon-like, with widths ranging from about 1m to about 5m.

The third level in the Lower Levels is called The Speedway. The Speedway is a network of smaller (3-5m wide) tubes that can be followed south from Spaghetti Junction for about 3km to the Middle of Nowhere, where it splits into a number of branches that end in sediment chokes. The Speedway also has a number of side passages, and intersects the Dead Coral Sea in a number of places. At the northern end of Spaghetti Junction, a series of climbs lead to the Paid in Full series. The Paid in Full series is a keyhole shaped passage that can be followed northwards for about 1km until it ends in a perched sump. The roof-tube is up to 8m in diameter and the canyon is up to 30m deep. A permanent stream, which is the upstream continuation of the Whingeing Pom Stream flows along the southern part of the Paid in Full canyon. Under low flow conditions, the sump at the end of the Paid in Full Series is a static pool. Under high flow conditions, this pool overflows into the Paid in Full canyon, and the water flowing out of the sump has been dye traced to the base level stream in the Northern Series (Thomas, 2016).

The highest level in the Lower Levels is the Wildcat Series. The Wildcat Series can be followed south from where it begins in a section of the cave called the Wild West for about 1.5km to a place called High Time, where it splits into 2 branches. These branches can be followed for about 1km until they end in rockfalls. The passages in the Wildcat Series are tubes that vary in size from 5m to 10m in diameter. In places, such as the Wild West and High Time, there are deep narrow canyons incised into the floor (figure 3.17). The Wildcat Series also has numerous oxbows and side passages, and there are deposits of river gravels up to 2m thick in places. There are a number of small streams in the Wildcat Series. These streams flow in narrow steeply descending canyons that crosscut the older tubes.

The Wildcat Series can be accessed from the Speedway or via a narrow series of steeply descending dry canyons that drop out of the floor of the Eye in the Sky passage just south of the Lion's Den, and intersects the Wildcat Series at High Time.

Figure 3.17. The High Time passage in the Wildcat Series of the Lower Levels of Bulmer Cavern. At this point, the tube is about 8m in diameter and the canyon in the floor is about 1m wide and 10m deep.

From the northern end of the Wild West, a small side canyon can be followed until it intersects a 50m deep shaft called the Awesome Aven. The Awesome Aven bisects an approximately 6m diameter phreatic tube (figure 3.18), and this tube can be accessed by climbing up about 6m from the bottom of the Awesome Aven.

Figure 3.18. The Awesome Aven. The outline of the tube that the Awesome Aven bisects can be seen on the left of the picture. The northward continuation of the tube is in the background.

The southern part of the tube that is bisected by the Awesome Aven can be followed in an anticlockwise downward spiral for about 500m until it intersects the International Stream. The northern part of the tube is the start of the Soupmix Series. The Soupmix Series can be followed northwards for about 800m through a network of tubes that in places are filled almost to the roof with sediment. The Soupmix Series is also one of the most spectacularly decorated areas of the southern series, with abundant crystal flowers and hydromagnesite “snow” coating all surfaces of the passages (figure 3.19).

Figure 3.19. A small sediment filled tube in the Soupmix Series.

Partway along the Soupmix Series, a small tube leads off to a complex maze of passages that eventually intersect the International Stream, and can also be followed to Spaghetti Junction (figure 3.20).

Figure 3.20. One of the small tubes that links the Soupmix Series to the International Stream.

The Soupmix Series ends where it intersects a larger passage called the Midnight Express. The Midnight Express can be followed northwards for approximately 100m until it meets a fault controlled section of passage called Who Dares Wins. Who Dares Wins is considered to be the boundary between the Southern Series and the Northern Series. The northern section of the Midnight Express is a tube that varies from about 5m to about 8m in diameter. In places, the floor of the tube is covered with sandy sediment. The southern section of the Midnight Express can be followed for about 1km, and ends in a sediment choke.

The structure of the phreatic parts of the lower levels resembles a 3 dimensional anastomosing maze (Palmer, 1991) that extends over a vertical distance of about 200m, and the overall gradient of the Southern Series suggests southward drainage. The relatively large and consistent size of the tubes suggest that they were fed by a substantial catchment area located some distance to the north. Superimposed on the anastomosing maze is a branching network of shafts and small canyons that carry the currently active streams in the Lower Levels.

The limited vertical extent and anastomosing nature of the phreatic passages in the Lower Levels suggest that they developed during a period of prolonged tectonic stability in an allogenic karst-aquifer system with a large hydraulic gradient (Palmer, 1991). The network of shafts and canyons crosscut the tubes of the lower levels, suggesting that they formed after the tubes were drained, and the relatively small size of the canyons and the branching layout suggest that they were formed by surface runoff sinking into exposed karst in an autogenic karst-aquifer system (Ford & Williams, 2007; Palmer, 1991).

Unlike the Upper Levels, there has been no scientific investigation of the sediments or speleothems present. Therefore, it is not possible to estimate the age of the Lower Levels beyond the fact that they must be younger than the Upper Levels.

Chapter 4: Sampling strategy

4.1 Overview of the sediments that are found in Bulmer cavern

Sediments that infill the passages of Bulmer Cavern resemble river gravels, and contain a mix of silts, sands and small pebble to small boulder sized clasts of metamorphosed siltstone and sandstone. Grain size sorting ranges from well sorted sands and silts to very poorly sorted conglomerates, which vary in structure from clast supported to matrix supported. The range of clast sizes suggest a wide variation in stream flows. There is a general trend to smaller clast sizes from north to south, which is consistent with the presumed paleodrainage direction of the Upper Levels (Main, 1988). The sediments are also generally well consolidated, and in places the uppermost layer is covered by a thin crust of reprecipitated calcium carbonate, or have speleothems growing on them (figure 4.1). This suggests that they have not been disturbed since they were deposited.

Figure 4.1. Carbonate crust and small stalagmites growing on gravel infill in a small tube below the Soupmix Series, Lower Levels of Bulmer Cavern.

The degree of clast roundness suggests that some clasts have been transported tens of kilometres from their source (Boggs, 2011) and some sediment deposits contain imbricated clasts, which allow for the deduction of the flow direction of the stream that transported and deposited the sediment (Colinson & Thompson, 1989).

4.2 Scope for applying other dating methods

4.2.1 Speleothem dating

Because Bulmer cavern is located in an alpine area, speleothems such as stalagmites and flowstone that are suitable for uranium-series dating are not abundant. Furthermore, most of the stalagmites present in Bulmer cavern are composed of aragonite that has partially inverted to calcite (Main, 1988). This means that the assumption that the speleothem has always been a closed system with respect to uranium and its decay products is no longer valid, and therefore the speleothems cannot be reliably dated. Another problem with using speleothem basal ages in Bulmer Cavern is the fact that as discussed in chapter 3.6, a long period of time has elapsed between the abandonment of the main Upper Levels Passage and the onset of speleothem growth in the upper levels.

4.2.2 Tephrochronology

The ~26ka Kawakawa-Ouranui eruption in the Taupo Volcanic Zone deposited significant amounts of ash over the Northwest Nelson area (figure 4.2), and there have been a number of similar sized eruptions from the Taupo and Coromandel volcanic zones since the Miocene (Wilson, 2001; Leonard et al, 2010). If tephras could be identified in sediment deposits and correlated with known eruptions, this would provide a way of independently corroborating cosmogenic nuclide burial ages.

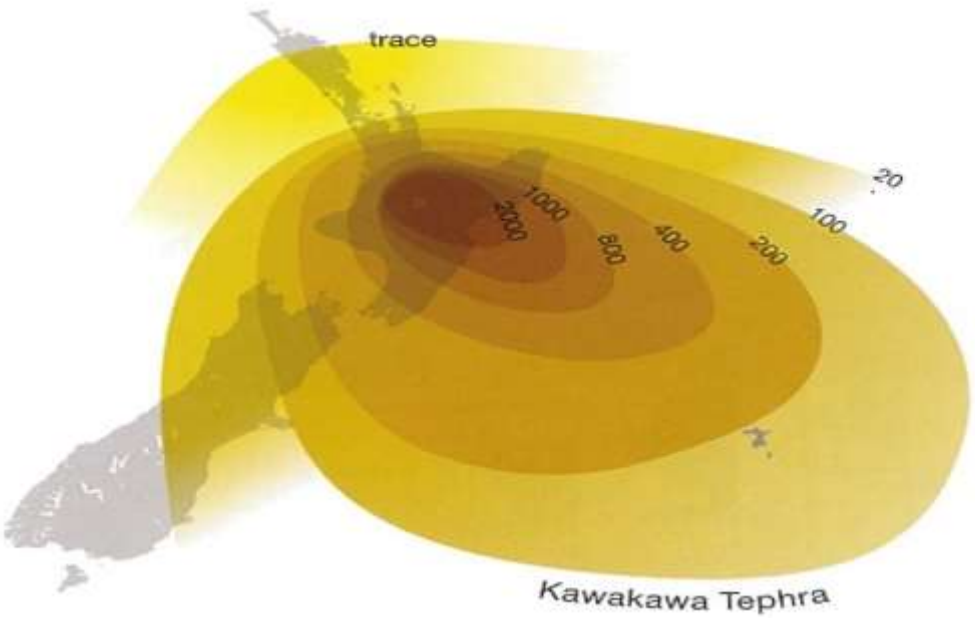

Figure 4.2. Isopach map showing the distribution of the 26 ka Kawakawa-Ouranui tephra. Contour intervals in mm. Image: D.Lowe.

4.2.3 Biostratigraphy/palynology

Even though there are no macrofossils present in the sediments of Bulmer Cavern, it may be possible to recover plant microfossils such as pollen, or insect microfossils such as chironomids from the fine fraction of the sediment deposits. Recovered microfossils could be compared with age calibrated datasets to give an independent corroboration of a cosmogenic nuclide burial age. Microfossils can also be used to infer information about paleoenvironmental conditions when the sediments were deposited.

Pollen preserved in cave sediments has also been used to link sediment deposits to potential surface source areas. Analysis of pollen recovered from modern (~150 calendar years before present) sediments in Mammoth Cave, Kentucky USA linked sediments deposited in the River Hall Passage to a potential source in the Green River floodplains, and sediments deposited in the Eyeless Fish Trail Passage to potential sources on the Mammoth Cave Plateau (Peterson, 1976).

4.2.4 Other paleoenvironmental proxies

Organisms build their cells out of complex organic (carbon containing) molecules. When they die, their cells break down into simpler molecules including amino acids, lipids, hydrocarbons, and cell membrane fragments called glycerol dialkyl glycerol

tetraethers (GDGTs) (Bianchi & Canuel, 2011). These molecules can then be mobilised by water, usually in flood events and transported into cave systems, where they can form films that can coat passage walls or speleothems, or be adsorbed onto sediment particles and preserved.

Amino acids can exist in 2 forms: the L-form, and its mirror image, the D-form.

The L-form is produced by living cells. When the cells die, the L-form inverts or racemises to the more stable D-form at a predictable rate (Williams & Smith, 1977). The ratio of L-form to D-form amino acids can be used as a dating method that in theory is useable for time periods up to ~1Ma (Ford & Williams, 2007).

Lipids are substances that are insoluble in water. The lipids that are most frequently used as paleoenvironmental proxies are hydrocarbons and fatty acids, which can be used to determine the origin (e.g. algae, bacteria, higher plants) of the lipids. The origin of the lipids can then be used to infer paleoenvironmental conditions. Furthermore, it is possible to measure the ratios of stable isotopes (δD, $\delta^{13}C$) in lipids, which can be used to infer information about vegetation type and aridity (Bianchi & Canuel, 2011 and references therein).

GDGTs are complex organic molecules produced by soil bacteria that have 2 parallel hydrocarbon chains linked by much shorter chains at each end (figure 4.3). The long chains can be modified by the bacteria by adding small side chains called methyl groups (methylation) or by inserting ring shaped molecules called cyclopentane (cyclisation) into the long chains. There is a positive correlation between the number of methyl groups on the long chain and mean air temperature and a negative correlation between the number of cyclopentane rings in the long chain and soil pH (Bianchi & Canuel, 2011 and references therein). These correlations allow the degree of methylation and cyclisation to be used as proxies for soil temperature and pH.

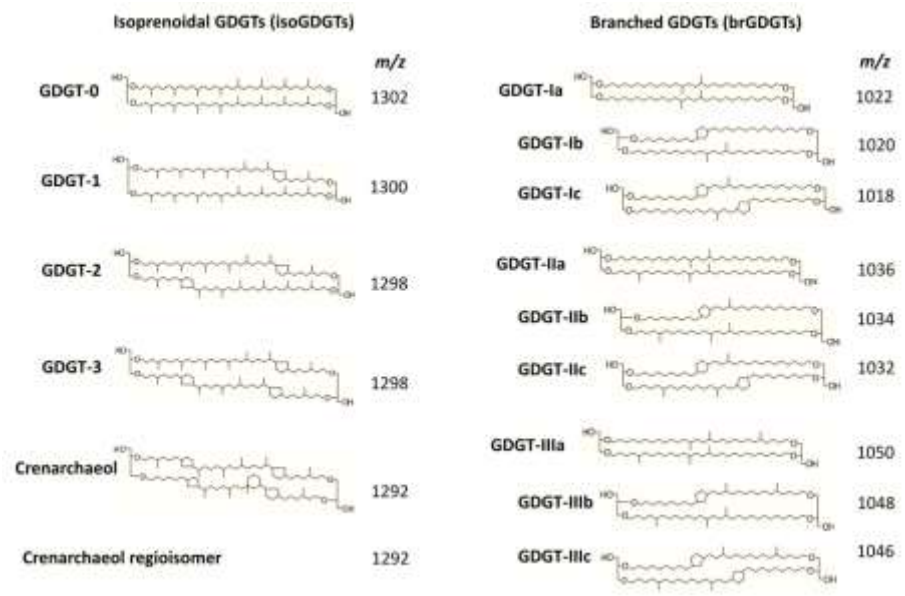

Figure 4.3. Molecular structure of the various GDGTs used to infer soil temperature and pH. m/z is the molecular mass to charge ratio. Naeher (2018).

4.3 Paleoflow indicators

4.3.1 Cave passage wall scalloping

Flowing water can erode asymmetric spoon-shaped pockets called scallops into the walls of a cave passage (figure 4.4).

Figure 4.4. An example of passage wall scalloping in the Wildcat Series, Bulmer Cavern.

In profile, these scallops resemble current ripples, and the orientation of the scallops can be used to infer the direction of flow of the stream that formed them (figure 4.5). There is also an inverse relationship between the lengths of the scallops and flow velocity (Ford & Williams, 2007; Curl, 1974).

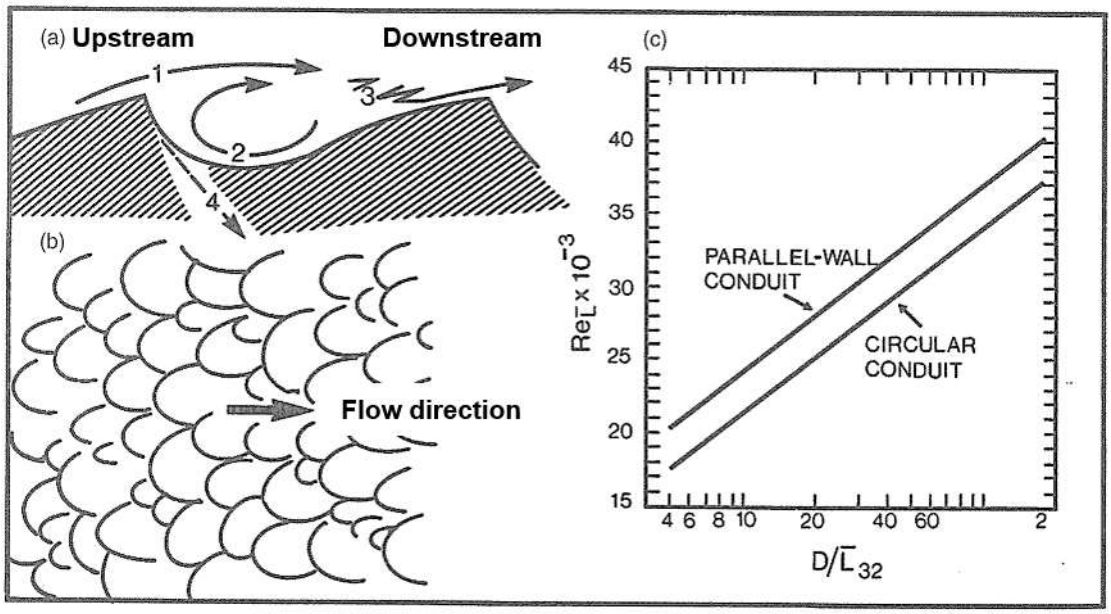

Figure 4.5. Cave passage wall scalloping. (a) Cross section through a scallop. (b) Fully developed scallop pattern. (c) The relationship between Reynold's number and the ratio of passage size to scallop length. Curl (1974).

Scallops range in size from ~0.5cm to ~2m in length, and form when the boundary layer of the stream flowing in a cave passage detaches from the passage wall (item 1 in figure 4.5a). A turbulent eddy then forms between the detached boundary layer and the passage wall, resulting in a zone of increased dissolution (item 2 in figure 4.5a). The primary control on the rate of limestone dissolution is the concentration of calcium ions in the water that is in contact with the passage wall (Palmer, 1991 and references therein), and the increased dissolution is a result of the increased turbulence transporting calcium enriched water away from the passage wall and replacing it with fresh water. Downstream of the zone of maximum dissolution, the eddy recombines with the boundary layer and reattaches to the passage wall (item 3 in figure 4.5a). The frequency of boundary layer detachment increases with flow velocity, resulting in a reduction in scallop length with increasing flow velocity (Curl, 1966; 1974). Flow velocity can be estimated by using the ratio of passage size to mean scallop length to determine the Reynold's number of the flow at the boundary between the stream and

the passage wall (figure 4.5c). Reynold's number is a measure of the amount of turbulence in a flowing fluid, and is a function of flow velocity and fluid viscosity. Once the Reynold's number has been determined, flow velocity can be calculated using the equation $V=v(Re/L_{32})$ where V=flow velocity, v=kinematic viscosity (a measure of a fluid's resistance to flow), Re=Reynold's number and L_{32} is Sauter mean scallop length (Ford & Williams, 2007). Sauter mean length is used to suppress the effect of very small scallops on the calculation of mean scallop length.

4.3.2 Sediment clast imbrication

Streams generally transport larger clasts (cobble to boulder sized) as bedload, where the clasts roll or slide along the stream bed. Elongated clasts tend to roll about their longest or a-axis, resulting in a preferred alignment where their a-axis is perpendicular to the flow direction of the stream. Rolling clasts also tend to come to rest leaning up against the clasts that are in front of them, resulting in an alignment where the clast's intermediate or b-axis is inclined, with the higher end pointing downstream (figure 4.6).

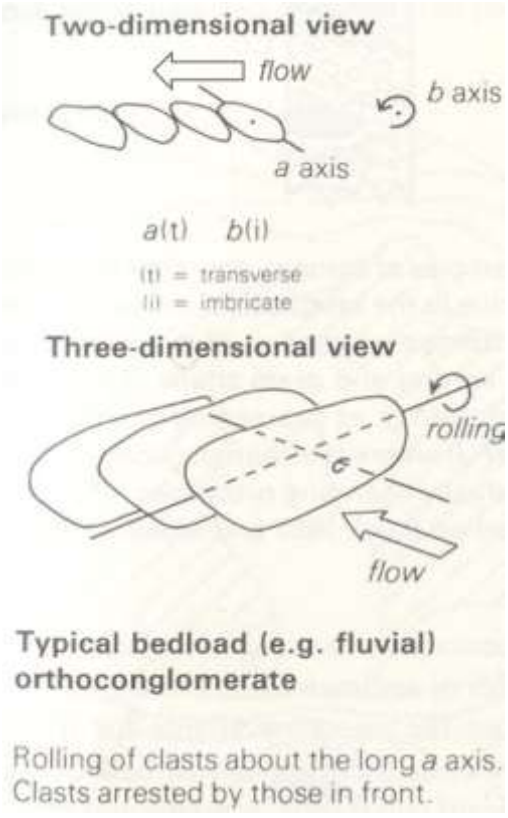

Figure 4.6. How elongated clasts align themselves when transported as bedload by a stream. Colinson & Thompson (1989).

4.4 Selection of sampling sites

Samples from multiple sites within the cave where we can be confident that the sediments have not been disturbed since emplacement will allow the construction of an age model that can be combined with an elevation model to determine uplift rates over the life of the cave. The collection of a range of clast sizes and lithologies may allow the identification of potential source areas and recovery of secondary age or environmental indicators such as volcanic ash or pollen.

Samples were collected from sites that are sufficiently quartz rich to be able to recover enough quartz for dating (about 100g) while allowing a sample size that is practical to carry out of the cave (about 1kg). To be as sure as possible that the sediments have not been disturbed since emplacement the sediments should be well consolidated and paleoflow indicators in the sediment such as clast imbrication should match paleoflow indicators such as passage wall scalloping. Where possible, two sites in the same passage were sampled. The use of multiple sampling sites from different levels of the cave will allow the construction of an age model that may be able to resolve changes in uplift rates over the life of the cave. 11 sediment sampling sites within the cave have been identified that meet these criteria, and their locations are shown in figure 4.7. The highest level sampled was the Castle Keep tube. Because the Castle Keep tube is so short, only one sample was collected from this level.

Three samples have been collected from the main Upper Levels passages. One was collected from the Cobble Passage, another from a site in the main Upper Levels Passage that is in between the Eurus Rift and the Panorama Ledge Entrance. A third sample was collected from the Road to Nowhere, from a site just before the sediment choke at the end of the passage.

Two samples have been collected from the Eye in the Sky Passage. One was collected from the sediment choke at the northern end of the passage, and the other from the Bear Pit, which is a section of canyon where sediment infill has been eroded away leaving a pit about 8m deep in the passage floor.

Two samples have been collected from the Wildcat Series. One was collected from a sediment deposit in the Wind in the Willows, and the other from the Octopus Room.

Two samples have been collected from the Soupmix Series. One was collected from a small tube that links the Soupmix Series to the International Stream. The other was collected from the Midnight Express tube from a site about 50m north of the junction with the Soupmix Series.

One sample has been collected from the Spaghetti Junction area from a sediment deposit in the Yelsgup passage.

In addition to the samples were collected from the cave, two samples of chert were collected from the summit plateau of Mt. Owen. These samples will allow for the measurement of the present-day $^{26}Al/^{10}Be$ production ratio at Mt. Owen. This measurement will provide a production ratio calibration since there is a lack of production rate data for ^{26}Al for the southern hemisphere. In addition to the production ratio measurement, the surface samples may allow the estimation of the age of the surface landscape or erosion rates.

4.5 Sampling methodology

Samples have been collected by excavating the surface of the sediment deposits, and enough material will be collected to fill a 1 litre screw top plastic jar. This size and type of container was chosen because a 1 litre container holds about 1-1½kg of river gravel, the size of the container allows for the collection of up to ~5cm sized clasts, and the containers are robust enough to survive transport out of the cave.

In addition to the collection of the samples, information on clast lithology, size range, fabric, and passage size and scalloping has been collected. This may allow for the reconstruction of paleoflow direction and velocity.

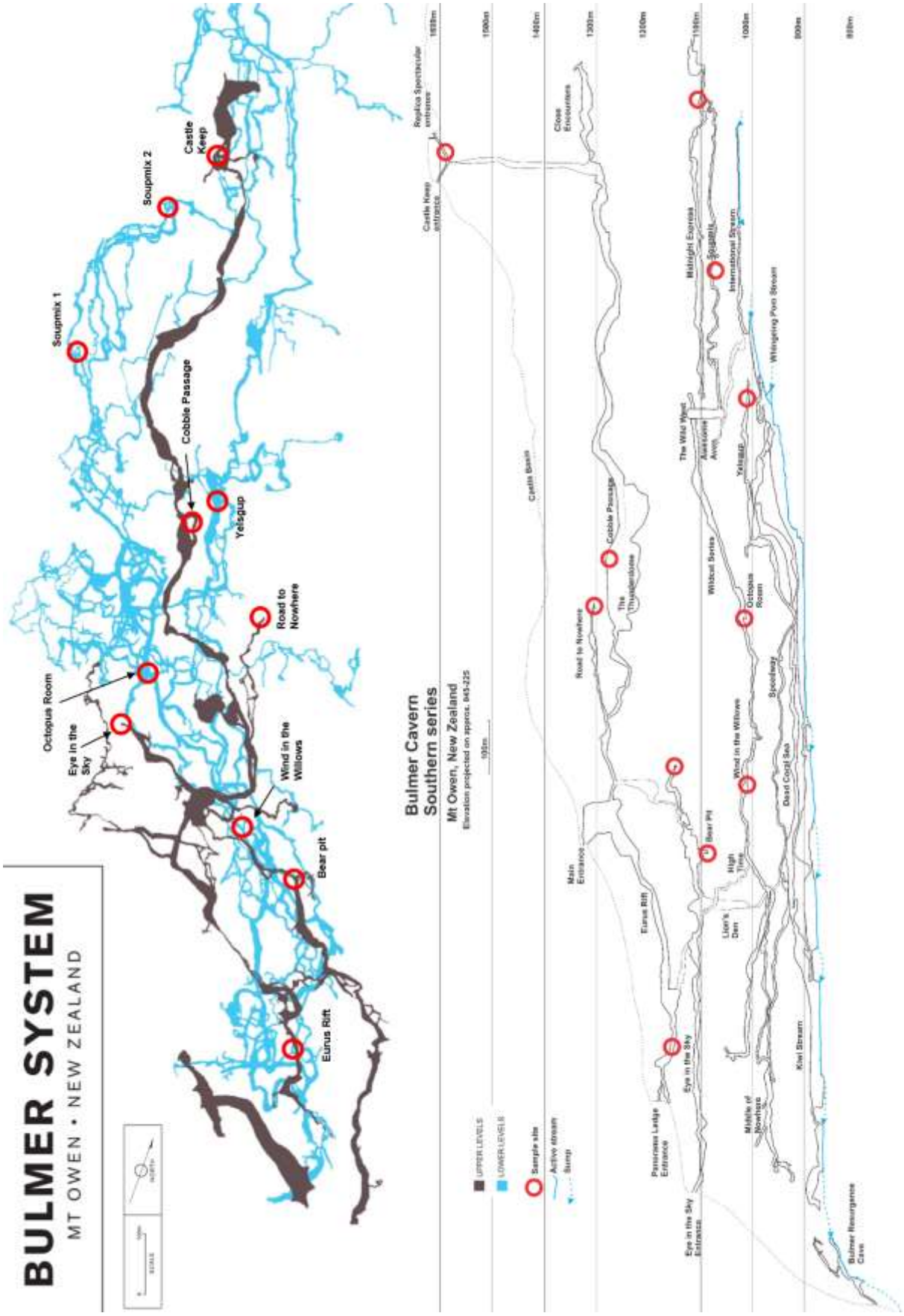

Figure 4.7. Map showing the location of the sample sites in Bulmer Cavern. Map supplied by Marcus Thomas (personal communication).

Chapter 5: Sample processing: cosmogenic nuclides

The cosmogenic nuclide extraction and purification process described here follows the Victoria University of Wellington (VUW) cosmogenic nuclide laboratory standard method. This method was initially developed by von Blankenburg et al (1996; 2004), and has since been modified by Jones (2012). The method has been further modified by myself for use with mixed lithology sediments. AMS analysis was carried out by the Purdue Rare Isotope Measurement Laboratory (PRIME Lab) at Purdue University Indiana USA.

5.1 Quartz extraction

All of the samples contained moisture, so were placed in pre weighed stainless steel bowls and dried at 50^{o}C for at least 24 hours. The dried samples were then reweighed to allow the calculation of sample moisture content. The samples were then dry sieved using a 2mm aperture sieve to remove the fine fraction. The fine fraction was retained to allow for further processing to extract material that could be used as secondary age indicators, or provide paleoenvironmental information. After dry sieveing, the coarse fraction was washed to remove any adhering silt particles, placed into pre weighed bowls and dried at 50^{o}C for at least 24 hours. After drying, the samples were reweighed to allow for the calculation of coarse fraction content.

After washing and drying, the coarse fraction was inspected and photographed. The largest and smallest clasts were measured to obtain a clast size range, and clast lithology, form and degree of rounding were also noted. A representative selection of clast lithilogies were set aside for petrographic and x-ray fluorescence (XRF) analysis, and any clasts of marble or chert were removed and discarded. The marble and chert were removed because of the high probability that they may have been sourced from within the cave system. Because the marble and chert have a much greater age compared to the half-lives of ^{10}Be and ^{26}Al, it is very unlikely that the marble or chert would have any cosmogenic nuclide content. The marble and chert would however dilute the ^{26}Al and ^{10}Be in the sample.

5.1.1 Physical quartz separation

Weighed aliquots of each sample were crushed down to medium sand (~1mm) size particles using a jaw crusher. Because this type of crusher produces a range of particle sizes, and the quartz extraction process works best with sand sized particles, the crushed samples were dry sieved at 90µm and washed to remove the fine fraction. After washing, the samples were dried at 50°C for at least 24 hours and reweighed to allow for the quantification of sample loss during the crushing process.

To remove magnetic minerals, the samples were then passed through a Frantz® isodynamic magnetic separator, with the current set to 1.2A, chute angle set to 15° and chute side tilt set to 10°. The non-magnetic fraction was examined with an optical microscope for the presence of magnetic minerals, and magnetic separation was repeated as required. After magnetic separation, the non-magnetic fraction was weighed to allow for the quantification of sample loss during the magnetic separation process.

5.1.2 Chemical quartz separation

To remove metal oxides and any residual carbonates, weighed aliquots of no more than 100g of the non-magnetic fraction were placed into pre-weighed 1 litre screw top high-density polyethylene jars and ~500ml of 10% hydrochloric acid (HCl) was added. The jars were left uncapped until visible reaction had ceased, then capped and placed in a waterbath at 50° C and allowed to leach for ~2 days with occasional agitation. After leaching, the samples were rinsed with deionised (18MΩ) water and the HCl leach was repeated.

To remove any remaining non-quartz minerals, after the HCl leaching process the samples were reacted with a mixture of 5% hydrofluoric acid (HF) and 2% nitric acid (HNO_3). After any initial reaction had ceased, the acid volume was topped up to ~700ml and the jars were capped and placed in the waterbath at 50°C for ~1 day with occasional agitation. After leaching, the samples were rinsed with deionised water and the HF+HNO_3 leach was repeated. After the second HF+HNO_3 leach, the samples were rinsed with deionised water until fluoride test strips indicated that there was no

detectable free fluorine, and dried in an oven set to 50°C. The samples were then weighed to allow for the quantification of sample loss during the acid leaching process, and a small aliquot of the cleaned quartz was taken for optical microscope and XRF analysis to assess the effectiveness of the leaching process.

5.2 Extraction of cosmogenic nuclides

5.2.1 Removal of meteoric ^{10}Be

To remove any meteoric ^{10}Be that is present in the sample, aliquots of between ~25g (the minimum amount of clean quartz needed for a reliable burial date) and ~100g (the practical maximum amount of quartz that can be processed) were placed into pre-weighed Savillex® screw-top Teflon beakers. The samples were then etched with 7 mole/litre (7M) HF in capped beakers for 1 hour on a hotplate set to 120°C. After 1 hour on the hot plate, the samples were allowed to cool, and the HF was decanted and the samples were rinsed with deionised water. The samples were then etched with aqua-regia (1 part 16M HNO_3: 3 parts 12M HCl) for at least 1 hour in capped beakers on the hot plate at 120°C. After the aqua-regia etch, the samples were rinsed thoroughly with deionised water and dried to constant weight. The final weight of the sample was then noted.

In order to check for and quantify any addition of cosmogenic nuclides to the samples as a result of processing, it is necessary to run a process blank. This was done by subjecting an empty beaker to the same reagents and processes as the ones used for the samples.

5.2.2 Beryllium (and aluminium) carrier addition

Because of the very low concentration of beryllium in quartz, it is necessary to add a known amount of ^{9}Be to the sample to allow for the measurement of the ^{10}Be/^{9}Be ratio. AMS analysis at Purdue University Rare Isotope Measurement Laboratory (PRIME Lab) requires the addition of about 300µg of ^{9}Be and this was done by adding a precisely weighed 1ml aliquot of an in-house carrier solution (VUW PK2) containing 305ppm ^{9}Be to the samples and the process blank. The carrier solution was prepared from a deep-mined phenacite.

Most quartz contains enough ^{27}Al for the total aluminium concentration to be measurable with other analytical methods such as atomic absorption spectrometry (AAS) or inductively-coupled plasma mass spectrometry (ICP-MS) so it was not necessary to add aluminium carrier to the samples. However, because the blank contains no aluminium, 2mg of aluminium carrier was added. This was done by adding a precisely weighed 2ml aliquot of a commercial aluminium standard solution containing 1000ppm aluminium.

5.2.3 Sample dissolution

Quartz dissolves in 28M HF to form silica tetrafluoride and water, which are both volatile, and hence can be evaporated off. Any metallic elements that are present in the quartz form fluoride salts, which are not volatile. The samples were dissolved by adding small quantities of 28M HF to the samples, and after the initial strongly exothermic reaction had finished allowed to dry on a hotplate set to 120^{o}C. The 28M HF addition process was repeated until all of the quartz had been dissolved.

5.2.4 Sample conversion

Because the fluoride salts that are formed during the quartz dissolution process are not readily soluble in the relatively dilute acids that are used in the remaining steps in the cosmogenic nuclide extraction and purification process, it is necessary to convert them to more soluble chloride salts. This was done by dissolving the residue from the quartz dissolution in aqua-regia (1 part 16M HNO_3: 2 parts 6M HCl) and evaporating to dryness. The samples were then redissolved with 10 ml of 6M HCl and transferred to 15ml polypropylene centrifuge tubes and centrifuged for 5 minutes at 3000rpm. The centrifuging step is necessary to prevent any insoluble material from contaminating the chromatography columns used in the purification process.

5.2.5 Total aluminium aliquot

In order to determine the total aluminium content of the sample, it is necessary to take a small aliquot of the dissolved sample for total aluminium analysis using AAS or ICP-MS before cosmogenic nuclide purification. This was done by transferring the redissolved sample into a pre-weighed centrifuge tube that is labelled Al-TSS, taking

care not to transfer any solid residue and reweighing the now full tube. A 500µl aliquot was taken out of the Al-TSS tube and transferred to a pre weighed 60ml low density polyethylene bottle. The bottle was then reweighed and the aliquot weight noted. To prevent the loss of aluminium by diffusion into the bottle, 5ml of 3M HNO_3 was added and the bottle was reweighed and the weight noted.

5.3 Cosmogenic nuclide purification by ion-exchange chromatography and selective precipitation

5.3.1 Removal of iron by ion-exchange chromatography

Iron was removed from the samples by passing the samples through 2ml of Bio-Rad® AG1-X8 anion resin loaded into 5ml Eichrom® columns. The resin was conditioned with 6M HCl. Under these conditions any Fe^{3+} iron in the sample forms a complex anion with chlorine and is therefore retained in the column. Beryllium and aluminium do not complex with chlorine, so stay as cations and pass through the column, and were eluted using 6M HCl.

The eluent was collected in Savillex® beakers and evaporated to dryness on a hotplate set to 120^{o}C.

5.3.2 Separation of beryllium by using ion-exchange chromatography

Separation of beryllium was done by dissolving the samples in 20ml of 0.4M oxalic acid and passing them through 5ml of Bio-Rad® AG50-X8 cation resin loaded into 15ml Eichrom® columns. The samples were dissolved in oxalic acid because oxalic acid forms an anionic complex with trivalent cations such as aluminium. This means that aluminium is not retained in the column. Mono and divalent cations do not from complexes with oxalic acid, and are retained in the column. The resin was conditioned with 0.4M oxalic acid, then the samples were loaded and the aluminium eluted using 0.4M oxalic acid. Sodium was then eluted using 0.5M HNO_3, then beryllium was eluted using 1M HNO_3. The beryllium eluent was collected in Savillex® beakers and evaporated to dryness on a hotplate set to 120^{o}C. All of the other eluents were collected in acid cleaned centrifuge tubes.

5.3.3 Purification of beryllium by selective precipitation

Because it is not possible to achieve perfect separation of beryllium from other divalent cations using column chromatography, it is necessary to use selective precipitation to further purify the beryllium fraction. Beryllium forms an insoluble hydroxide between pH 6 and pH 12, and other divalent cations such as magnesium and calcium stay in solution in this pH range (Ochs & Ivy-Ochs, 1997).

The selective precipitation was done by dissolving the dried beryllium eluent with 5ml of 1M HNO_3, transferring the solution into 15ml centrifuge tubes and alkalising to pH ~11 with 25% ammonia solution. The precipitate was then centrifuged and the supernate was discarded. The precipitate was then redissolved with 5ml of 1M HNO_3, and the selective precipitation was then repeated. The precipitate was then washed 3 times with deionised water.

5.3.4 Beryllium oxidation and AMS target packing

In order to make the extracted beryllium suitable for AMS analysis, it is necessary to transform the precipitated beryllium hydroxide into beryllium oxide. This was done by dissolving the beryllium hydroxide in ~0.3ml of 5M HNO_3 and transferring the solution into pre-weighed quartz crucibles. The solution was then dried on the hotplate at 120^{o}C and calcined over a Bunsen burner flame. The calcined samples were then reweighed to allow the calculation of beryllium percentage yield, which is a measure of extraction efficiency. Typical oxidised sample weights are about 1mg. The oxidised samples were then mixed with powdered niobium (1 part oxidised sample: ~3 parts niobium by weight) and packed into the AMS targets supplied by PRIME Lab. For maximum ionisation efficiency, the sample needs to be as close to the front of the target as possible. Because the PRIME targets hold about 10mg of material, about 6mg of copper was packed into the targets before the sample was loaded.

5.3.5 Separation of aluminium using ion-exchange chromatography

Separation of aluminium was done by passing the aluminium eluent from the beryllium columns through 1ml of Bio-Rad®AG1-X8 anion resin loaded into 7.5ml columns. The resin was conditioned with 0.4M oxalic acid. Under these conditions, the oxalate complexes are stable and hence retained in the column. The aluminium was eluted with a mixture of 0.05M oxalic acid and 0.5M HCl. Under these conditions, the aluminium oxalate complex breaks down and the aluminium is no longer retained in the column. The aluminium eluent was collected in Savillex® beakers and evaporated to dryness on a hotplate set to 120^{o}C. To remove the oxalic acid, the samples were dissolved in aqua-regia (1 part 16M HNO_3:1 part 6M HCl) and evaporated to dryness. This step was repeated twice. After treatment with aqua-regia, the samples were reacted with a mixture of 1 part 16M HNO_3 and 1 part 32% hydrogen peroxide (H_2O_2) and allowed to evaporate to dryness. The HNO_3+H_2O_2 treatment was repeated until there were no visible oxalic acid crystals in the dried samples.

5.3.6 Purification of aluminium by selective precipitation

Because magnesium can cause isobaric interference with the measurement of aluminium in an AMS, it is necessary to use selective precipitation to ensure complete removal of magnesium from the sample. Aluminium forms an insoluble hydroxide between pH 5 and pH 8 whereas magnesium stays in solution at pH<9 (Ochs & Ivy-Ochs, 1997).

The selective precipitation was done by dissolving the samples in 5ml of 1M HNO_3, transferring the dissolved samples into 15ml centrifuge tubes and alkalising to pH 7–8 with 25% ammonia solution. After centrifuging, the supernatant was discarded and the precipitate was washed with deionised water.

5.3.7 Aluminium oxidation and AMS target packing

In order to make the extracted aluminium suitable for AMS analysis, it is necessary to transform the precipitated aluminium hydroxide into aluminium oxide. This was done by dissolving the aluminium hydroxide in ~0.3ml of 5M HNO_3 and transferring the solution into pre-weighed quartz crucibles. The solution was then dried on the

hotplate at 120°C and calcined over a Bunsen burner flame. The calcined samples were then reweighed to allow the calculation of aluminium percentage yield. Typical oxidised sample weights were between 1-5mg. The oxidised samples were then mixed with powdered niobium (1 part oxidised sample: ~3.5 parts niobium by weight) and packed into the AMS targets supplied by PRIME Lab. Where necessary, the targets were packed with the appropriate amount of copper to ensure the sample was as close to the front of the target as possible to maximise ionisation efficiency.

5.4 Determination of quartz total aluminium concentration by ICP-MS

The aluminium content of the total aluminium aliquot was measured using a Thermo-Fisher Element-2 magnetic sector mass discriminator ICP-MS at the VUW geochemistry laboratory. The aliquots were diluted by a factor of ~23 000 and spiked with a known amount of caesium to use as an internal standard before analysis. The diluted aliquots were analysed alongside a set of aluminium standards for calibration.

5.5 Modification of the separation method for processing dirty quartz

To increase the purity of the quartz recovered from the heavily metamorphosed lithologies found in the sediments of Bulmer cavern, it was necessary to crush the samples to a grain size that was similar to the modal grainsize of the sampled material. The modal grainsize was determined by petrographic examination of thin sections of the sampled material, and most of the lithologies sampled were fine sandstones.

After initial crushing using the jaw crusher, the grainsize of the samples was further reduced by using a tungsten carbide ring mill. Because the ring mill is designed to crush rock to powder, it was necessary to adapt the standard operating procedure for the mill to produce fine sand size particles. This was done by running aliquots of sample in the mill for ~5 seconds at a time on the low speed setting, and sieveing the crushed samples at 63µm and 250µm between each run. The <63µm fraction was discarded and the >250µm fraction was put back into the mill and the process repeated. This approach minimised the amount of sample crushed to powder.

The samples were then put through the standard chemical separation process, and the efficiency of the chemical process was assessed by analysing aliquots of the cleaned

quartz using XRF. XRF analysis was carried out at VUW using an Olympus Vanta® portable XRF analyser on aliquots of sample packed into sample cups with 4µm polypropylene windows.

Chapter 6: Sample processing: pollen and other paleoenvironmental proxies

6.1 Pollen extraction

This method for extracting pollen from samples with very low pollen abundances has been developed using information from Xun Li (personal communication), Ryan et al (2012), and Traverse (2007).

6.1.1 Physical separation

Approximately 100g of the fine (<2mm) fraction of sediment sample was wet sieved through 90µm and 1.4mm sieves. The >1.4mm and 90µm–1.4mm fraction were then dried at 50°C and bagged for storage. The <90µm fraction was then sieved using 6µm sieve cloth to remove the clay fraction, and the 6µm-90µm fraction was transferred into 50ml polypropylene centrifuge tubes.

6.1.2 Carbonate removal

To remove any carbonates, the 6µm-90µm fraction was reacted with 10% HCl. To allow for the quantification of relative pollen abundances, a lycopodium tablet was added to the sample at this point. After any visible reaction had stopped, the samples were centrifuged, the acid decanted, and rinsed three times with deionised water.

6.1.3 Humic acid removal

To remove humic acids, the samples were reacted with hot 10% potassium hydroxide (KOH) solution. This reaction was carried out in a waterbath set to 98°C. After 10 minutes, the samples were centrifuged and the KOH decanted. The samples were then washed with deionised water until pH indicator strips indicated that all traces of KOH were removed.

6.1.4 Heavy liquid separation

Pollen grains were separated by mixing the samples with a solution of sodium polytungstate (SPT) with a density of 2.2g/cm^3. After mixing with SPT, the samples

were allowed to settle and then centrifuged at 2000rpm for 10 minutes, and the supernatant was decanted and filtered through 6µm sieve cloth to collect the pollen grains.

The pollen was then rinsed off the filter cloth with deionised water and collected in 15ml centrifuge tubes.

6.1.5 Acetolysis

To remove any traces of cellulose from the surface of the pollen grains, the samples were treated with a mixture of acetic anhydride and 18M sulphuric acid (H_2SO_4) (9 parts acetic anhydride:1 part 18M H_2SO_4) for 10 minutes in a waterbath set to 90^{o}C. The samples were dehydrated prior to the acetolysis procedure by rinsing them with glacial acetic acid. After the acetolysis procedure, the samples were washed with glacial acetic acid and centrifuged for 5 minutes at 2000rpm to remove the acetolysis mixture, then washed with deionised water until all traces of acetic acid were removed.

6.1.6 Pollen identification and quantification

For identification and quantification, pollen grains were mounted onto glass microscope slides using gelatine. The slides were then examined using a transmitted-light optical microscope, and observed pollen grains were identified by comparison to reference material.

6.2 Plant lipid extraction by solvent extraction

This method for extracting plant lipids has been adapted from a method described by Marlow et al (2001) for extracting plant lipids from marine sediment cores.

Approximately 3g of the fine fraction was mixed with approximately 3ml of a 3:1 mix of dichloromethane and methanol and sonicated for 15 minutes in an ultrasonic bath. The solvent was then decanted and the extraction process repeated three times. The solvent from each extraction was recombined, and the solvent evaporated off. Because the extracts contained large amounts of clay, they were redissolved using the

extraction solvent and vacuum filtered using 1.2µm glass fibre filter paper into pre-weighed vials, and the solvent was evaporated off.

Chapter 7: Sampling results

Samples were collected from both of the sites in the main Upper Levels Passage, both of the sites in the Eye in the Sky Passage, both of the sites in the Wildcat Series, both of the sites in the Soupmix Series and from the site in Spaghetti Junction during the New Zealand Speleological Society supported summer expedition of 2017. The samples from Castle Keep and the Road to Nowhere, and the two surface samples from the summit of Mt. Owen were collected during the 2018 expedition.

With the exception of the site at the southern end of the main Upper Levels Passage and the two surface samples, approximately 1-1½kg of gravel was collected from each site. At the site at the southern end of the Upper Levels Passage, there was insufficient material to collect a ~1kg sample, so only 800g was collected. Because the chert sampled on the summit of Mt. Owen was almost pure quartz, only ~300g of material was collected.

7.1 Sample site and sample descriptions

7.1.1 Castle Keep

The sample was collected approximately 10m north of the lowest point in the passage. At this point, the passage is oval in cross section, 6m wide and 3m high and runs north-south. The altitude of the Castle Keep entrance was measured at 1605m asl using a handheld GPS receiver, and the Bulmer Cavern survey shows that the sample site is located 15m below the Castle Keep entrance. Therefore the sample site has an elevation of 1590m asl. Exfoliation of the passage walls has removed any passage wall scalloping at the sampling site. However, poorly developed scalloping at other points in the passage indicate north-south paleoflow. No clast imbrication was observed in the sampled sediments.

The sediment deposit sampled is located against the true right wall of the passage, and consists of sub-angular to rounded pebble to small cobble-sized clasts in a sandy mud matrix (figure 7.1). There are also some sub-rounded small boulder-sized clasts. The coarse fraction, which made up 71% of the sampled material had a size range of 2mm to 60mm along the longest axis. Most of the clasts were disc or blade shaped and there

were some roller-shaped clasts as well. Some of the clasts had thin and patchy deposits of secondary carbonate. Most of the clasts were grey fine to medium-grained well indurated sandstone and laminated black shale. There were also some clasts of what initially appeared to be white limestone. When these clasts were cut for the preparation of thin sections, they were found to be grey indurated sandstone covered with a ~2mm thick coating of secondary carbonate.

Figure 7.1. The sediment deposit sampled in the Castle Keep passage.

There was also 1 angular clast of Arthur Marble in the sample.

After the removal of material that was not suitable for further processing, 62% of the sampled material was processed for quartz extraction, yielding 3% recoverable quartz.

7.1.2 The Road to Nowhere

The sample was collected approximately 10m south of the sediment choke that marks the known end of the passage. At this point, the passage is a round tube approximately 3m in diameter (figure 7.2) that runs north-south. The altitude of the sampling site was measured at 1330m asl using a barometric altimeter. This is about 20m higher than the

elevation indicated by the Bulmer Cavern survey, which indicates an elevation of 1310m asl.

Figure 7.2. The Road to Nowhere Passage. The sample site is located behind and to the right of the caver.

Weakly developed scalloping at the sample site indicates north-south paleoflow (figure 7.3). No discernible trend in clast imbrication was noted.

Figure 7.3. Weakly developed scalloping indicates paleoflow from right to left. The sample was collected from the area below the notebook.

The sediment deposit sampled is located against the true right wall of the passage, and consists of muddy coarse sand, pebbles and some small cobbles (figure 7.4).

Figure 7.4. Close up of the sediment deposit sampled in the Road to Nowhere.

The coarse fraction, which makes up 77% of the sampled material consists of mostly small to large sub-rounded to rounded pebbles of grey indurated fine to medium grained sandstone. The largest clasts measure up to 60mm long along their longest axis. The sample also contained 7 pebbles of porous pale yellow sandstone and 1 pebble of chert. Some of the grey sandstone clasts have mm-scale lamination. After the removal of material that was to be kept for petrographic analysis or was not suitable for further processing, 74% of the sample was processed for quartz extraction, yielding 9% recoverable quartz.

7.1.3 The Cobble Passage

The sample was collected from the upper part of a sediment deposit located approximately halfway along the Cobble Passage from its northern junction with the main Upper Levels Passage. At this point the passage is a round tube that runs north-

south and is approximately 5m in diameter (figure 7.5). The Bulmer cavern survey indicates that the Cobble Passage has an elevation of 1270m asl. No barometric altimeter reading was taken this site.

Figure 7.5. The Cobble Passage looking north from the sample site. The sample was collected from the deposit on the left of the picture.

Any passage wall scalloping at this site has been obscured by the abundant anthodite speleothems growing on the walls, and in places on the sediment deposit. Clast imbrication in the sediment deposit suggests north-south paleoflow.

The sediment deposit is located against the true right wall of the passage, and consists of rounded pebble to cobble-sized clasts in a muddy sand matrix. On the surface of the deposit is a layer of large cobble to small boulder-sized clasts that are partially cemented with secondary carbonate deposits (figure 7.6).

Figure 7.6. The sediment deposit sampled in the Cobble Passage. North is to the right of the picture.

The coarse fraction, which makes up 84% of the sample consists of disc and blade shaped clasts of grey indurated sandstone, phyllite or black shale. The largest clasts collected measure up to 80mm along their long axis. Some of the larger clasts are broken, and the broken faces have weathered to an orange-brown colour. Some of the clasts show mm-scale lamination. There was also 1 pebble-sized clast of orange indurated sandstone, 1 pebble-sized clast of chert and 1 large angular clast of Arthur Marble. On the floor of the Thunderdome immediately below the southern end of the Cobble Passage were a number of well-rounded cobbles of very pure quartzite.

After the removal of material that was to be kept for petrographic analysis or was not suitable for further processing, 68% of the sample was processed for quartz extraction, yielding 11% recoverable quartz.

7.1.4 Southern main Upper Levels Passage (Eurus Rift)

The sample was collected from a point approximately half way between the end of the Eurus Rift section of the main Upper Levels Passage and the intersection with the side

passage that leads to the Panorama Ledge Entrance. At this point, the passage is oval in cross section, 7m wide and 5m high and runs from northwest to southeast (figure 7.7). According to the Bulmer Cavern survey, the site is at 1160m asl. A barometric altimeter reading taken at the time the sample was collected indicated an elevation of 1220m asl.

Figure 7.7. The southern end of the main Upper Levels Passage looking south. The sample site is on the right hand side of the picture.

Any passage wall scalloping at the sample site has been obscured by either exfoliation of the passage wall or encrustations of cave coral and no clast imbrication was observed in the sampled sediment.

The sediment deposit sampled is located on the presumed true right wall of the passage underneath a crust of secondary carbonate cemented mud and pebbles (figure 7.8), and consists of small to large sub angular to rounded pebbles in a yellow clay-rich matrix.

Figure 7.8. Close up of the sample site. The sample was collected from where the hammer is located.

The coarse fraction makes up 64% of the sampled material, and consists of disc and blade shaped clasts of well-indurated grey fine to medium-grained sandstone. The largest clasts sampled measure up to 50mm along their longest axis. There was also 1 clast of porous yellow sandstone.

After the removal of material that was to be kept for petrographic analysis or was not suitable for further processing, 39% of the sample was processed for quartz extraction, yielding 12% recoverable quartz.

7.1.5 Northern end of Eye in the Sky Passage

The sample was collected from the surface of the sediment choke that marks the northern end of the passage (figure 7.9).

Figure 7.9. The sediment choke at the northern end of Eye in the Sky Passage.

At the point where the sample was collected, the passage is a round tube approximately 5m in diameter that runs west-east. The Bulmer Cavern survey shows that the sampling site is at an elevation of 1160m asl, and barometric altimeter measurements of the elevation of the sample site range from 1159m asl to 1174m asl. Well-developed passage wall scalloping (figure 7.10) indicates west-east paleoflow. Imbrication of clasts on the surface of the sediment deposit also indicate west-east drainage.

The sediment deposit occupies the whole width of the passage, and consists of sub-angular to rounded pebble to small boulder-size clasts with a sandy matrix (figure 7.11). Some of the clasts on the surface of the deposit are cemented with secondary carbonate deposits, and there are a number of small stalagmites growing on the sediment deposit. There is also a thin layer of pale grey glass-shard like material amongst the cobbles in the uppermost part of the deposit.

Figure 7.10. Passage wall scalloping on the true left wall of the northern end of Eye in the Sky passage. Hammer pick is facing upstream.

Figure 7.11. Close up of the sediment deposit at the northern end of Eye in the Sky Passage. Hammer pick is facing downstream. Glass shard like material was found in the circled area.

The coarse fraction, which makes up 85% of the sampled material consists of spherical, disc and blade-shaped clasts of fine to medium-grained grey indurated sandstone. Some of the clasts have patchy orange weathering rinds. Some of the clasts also contain quartz veins. The sample also contained 1 clast of black shale with mm-scale lamination. The largest clasts sampled measure up to 85mm along their longest axis. No marble was present in the sampled material.

After the removal of material that was to be kept for petrographic analysis, 56% of the sample was processed for quartz extraction, yielding 12% recoverable quartz.

7.1.6 The Bear Pit

The Bear Pit is located in the floor of the canyon section of the Eye in the Sky Passage approximately 100m west of the Lion's Den. The Bear Pit formed as a result of the erosion of sediment that infills the lower part of the canyon, leaving a hole about 8m deep in the floor of the passage (figure 7.12). The canyon is about 3m wide at this point.

Figure 7.12. The Bear Pit looking east (downstream). The sample was collected from the bottom of the pit at the eastern end (Lower centre in this picture).

The Bulmer Cavern survey indicates that the point where the sample was collected is at 1080m asl. No barometric altimeter readings were taken at this site. In this part of the cave, the passage runs west-east and passage wall scalloping in the bottom of the Bear Pit indicates west-east paleoflow (figure 7.13).

Figure 7.13. Scalloping on the south side of the Bear Pit indicating drainage to the east. Hammer pick is pointing in direction of drainage.

There are 2 distinct sediment lithologies exposed in the Bear Pit. The upper layer is about 6m thick at the eastern end, and consists of cm-scale bedded fine sands and silts, and contains sparse pebbles. The lower layer consists of pebble to small cobble-sized clasts in a sandy matrix. There is an abrupt contact between the 2 layers, and clast imbrication in the lower layer indicates drainage to the east. The sample was collected from the lower layer.

The coarse fraction, which makes up 91% of the sampled material consists of mostly disc and blade shaped clasts of pale yellow-brown to dark grey indurated fine to medium-grained sandstone. The largest clasts sampled measure up to 80mm along

their longest axis. Some of the clasts sampled show faint mm-scale lamination. There was also 1 clast of vein quartz and 1 clast of foliated schist in the sample.

After the removal of material that was to be kept for petrographic analysis or was not suitable for further processing, 62% of the sample was processed for quartz extraction, yielding 13% recoverable quartz.

7.1.7 The Wildcat Series - Wind in the Willows

The sample was collected from the top of a ~1.5m thick deposit of sub-angular to rounded pebbles, cobbles and small boulders with a sandy matrix located about 400m north of High Time. At the point where the sample was collected the passage is an oval-shaped tube that is about 3m wide, 4m high and runs northwest-southeast (Figures 7.14 and 7.15).

Figure 7.14. The Wildcat Series looking northwest. The sample was collected from the sediment bank in the bottom right of the picture.

Figure 7.15. Close-up of the sediment deposit.

The Bulmer Cavern survey indicates that the sampled site is at an elevation of 1000m asl, and barometric altimeter readings at the sample site range from 1029m to 1076m. Well-developed passage wall scalloping indicates northwest-southeast paleoflow.

The coarse fraction makes up 92% of the sampled material, and consists of disc and blade shaped clasts of light yellow-brown to grey indurated fine to medium-grained sandstone. The largest clasts sampled measure up to 60mm along their longest axis. There was also 1 clast of moderately indurated fine to medium-grained laminated green sandstone, 2 clasts of vein quartz, 1 clast of white fine sandstone and 1 clast of foliated schist in the sample.

After the removal of material that was to be kept for petrographic analysis or was not suitable for further processing, 61% of the sample was processed for quartz extraction, yielding 11% recoverable quartz.

7.1.8 The Wildcat Series - Octopus Room

The sample was collected from a sediment deposit on the floor of the southern end of the Octopus Room. The point where the sample was collected is an alcove that is 5m wide and 1.5m high. There is stalagmite in growth position that does not show signs of recent growth on the sediment deposit (figure 7.16). No paleoflow indicators were observed at this site. The Bulmer Cavern survey indicates that the Octopus Room is at an elevation of 1020m asl. Barometric altimeter readings taken at the Octopus Room range from 1022m to 1070m.

Figure 7.16. The Octopus Room looking south. The sample was collected from the area by the red tape at the left of the picture.

The sediment deposit is about 10cm thick and consists of rounded pebbles and small cobbles in a sandy mud matrix (figure 7.17). The coarse fraction, which makes up 90% of the sampled material consists of disc, blade and roller shaped clasts of light yellow-

brown to grey indurated fine to medium-grain sandstone. There were also a few clasts of black shale. Some clasts show mm-scale lamination and others contain quartz veins. The largest clasts sampled measure up to 80mm along their longest axis.

Figure 7.17. Close up of the sediment deposit in the Octopus Room.

After the removal of material that was to be kept for petrographic analysis or was not suitable for further processing, 61% of the sample was processed for quartz extraction, yielding 13% recoverable quartz.

7.1.9 The Soupmix Series - Soupmix 1

The sample was collected from a gravel deposit in a small tube that links the main Soupmix tube to the International Stream. At the point where the sample was collected, the passage is a round tube 1.2m in diameter that runs west-east. Well-developed passage wall scalloping indicates drainage to the east (figure 7.18). The Bulmer survey indicates that the sample site is at an elevation of 1070m asl. Barometric altimeter readings taken at the site range from 1045m to 1105m.

Figure 7.18. The small tube leading off the Soupmix looking upstream from the sample site.

The gravel deposit consists of sub-rounded to rounded pebbles and small cobbles with a sandy matrix. The uppermost layer of the gravel is cemented with secondary carbonate and clast imbrication indicates that the stream that deposited the sediment flowed from west to east (figure 7.19). The coarse fraction makes up 78% of the material sampled, and consists of disc, roller and blade-shaped clasts of light yellow-brown to dark grey indurated fine to medium-grained sandstone. The largest clasts sampled measure up to 65mm along the longest axis. Some clasts also show mm-scale lamination. There was also 1 clast of yellow poorly indurated fine sandstone that contained some lithic fragments.

Figure 7.19. The gravel deposit sampled in the small tube leading off the Soupmix.

After the removal of material that was to be kept for petrographic analysis or was not suitable for further processing, 57% of the sample was processed for quartz extraction, yielding 10% recoverable quartz.

7.1.10 The Soupmix Series - Soupmix 2

The sample was collected from a gravel deposit that is at least 1m thick located underneath a secondary carbonate false floor in the Midnight Express tube at a point about 50m north of the junction with the Soupmix Series. At the sampling site, the passage is an oval-shaped tube that is 5m wide and 2m high running north-south. Well-developed passage wall scalloping on the true left wall indicates north-south paleoflow (figure 7.20). The Bulmer Survey indicates that the altitude of the sample site is at 1100m asl. Barometric altimeter readings at the site range from 1079m to 1152m.

Figure 7.20. The Midnight Express tube where Soupmix 2 was collected looking north. The hole in the floor where the sample was collected is in the middle foreground.

The gravel deposit consists of rounded pebbles and occasional small cobble-sized clasts in a muddy sand matrix (figure 7.21). It was not possible to observe any clast imbrication at this site. The coarse fraction makes up 85% of the sampled material, and consists of disc and blade-shaped clasts of fine to medium grained grey indurated sandstone, phyllite or black shale. Some clasts show weakly developed mm-scale lamination, and the largest clasts sampled measure up to 110mm along their long axis. There was also 1 clast of sandstone that contains quartz veins and 1 clast of soft green siltstone.

Figure 7.21. Close up of the sediment underneath the false floor at the Soupmix 2 sample site.

After the removal of material that was to be kept for petrographic analysis or was not suitable for further processing, 50% of the sample was processed for quartz extraction, yielding 7% recoverable quartz.

7.1.11 Yelsgup

The sample was collected from a cobble deposit in the main Yelsgup tube about 50m south of survey station 50. At the sampling site, the passage is a round tube about 3m in diameter that runs north-south, and the cobble deposit occupies the bottom quarter of the tube. The tube carries a north-flowing ephemeral stream that has cut a channel into the cobble deposit. Cave coral has obscured any evidence of passage wall scalloping at the sample site. However, clast imbrication in the cobble deposit suggests that the stream that deposited the cobbles flowed north-south (figure 7.22). The Bulmer survey indicates that the sample site is located at an elevation of 1010m asl. No barometric altimeter readings were taken at this site.

Figure 7.22. The cobble deposit in the Yelsgup passage. The hammer pick is facing in the paleoflow direction as indicated by clast imbrication.

The coarse fraction, which makes up 82% of the sampled material consists of sub-angular to sub-rounded disc and blade-shaped pebbles and small cobbles of fine to medium-grained grey indurated sandstone. The largest clasts sampled measure up to 65mm along their long axis. There was also 1 clast of pale yellow-pink recrystallized sandstone in the sample.

After the removal of material that was to be kept for petrographic analysis or was not suitable for further processing, 57% of the sample was processed for quartz extraction, yielding 9% recoverable quartz.

7.2 Surface samples

7.2.1 Surface samples – Mt. Owen 1

The sample was collected from a chert nodule exposed in an outcrop of marble on the summit plateau of Mt. Owen (41.552543°S, 172.540744°E, 1869m) approximately 50m southeast of the trig beacon. The outcrop dips to the south at an angle of about 30°,

and has an unobstructed view of the horizon to the south (figure 7.23). The chert nodule protrudes about 30mm out of the outcrop face.

Figure 7.23. The outcrop where Mt. Owen 1 was collected looking east. The chert nodule is by the hammer pick.

7.2.2 Surface samples – Mt. Owen 2

The sample was collected from a chert nodule exposed in a northwest facing outcrop of marble on the summit plateau of Mt. Owen (41.551638°S, 172.539551°E, 1865m) approximately 150m south of the trig beacon Figure 7.24). The outcrop dips to the northwest at an angle of about 30°, and has an unobstructed view of the horizon to the northwest. The chert nodule protrudes approximately 50mm out of the outcrop face.

Figure 7.24. The outcrop where Mt. Owen 2 was collected looking southeast. The chert nodule is next to the hammer pick.

Chapter 8. Results

8.1. Cosmogenic nuclide analysis

Because a number of samples still appeared to be dirty after the quartz separation process, two samples were put through the VUW cosmogenic nuclide lab standard extraction process initially, to test the method. Approximately 30g aliquots of cleaned quartz were taken from the Eye in the Sky and Wind in the Willows samples.

A quantity of very fine black material was released from the samples during the meteoric ^{10}Be removal process, and after dissolution with 28M HF, there was a black residue coating the inside of the beakers. After the sample conversion and transfer process, there was approximately 0.05ml of grey residue in the bottom of the centrifuge tubes and a black coating on the inside of the tubes. The transferred solution was also a dark yellow colour. The colour of the transferred solution suggested that the samples still contained substantial amounts of iron and other impurities, so the samples were split over multiple columns for the separation of beryllium and aluminium.

After the separation and purification process, isotope ratio measurements were successfully carried out by PRIME Lab, and the results for the Eye in the Sky sample are presented in tables 8.1 and 8.2. Total aluminium was successfully measured, and the results for the Eye in the Sky sample are presented in table 8.2.

The successful measurements of both isotope ratios and total aluminium concentrations suggested that the standard cosmogenic nuclide extraction process could be used with highly metamorphosed quartz.

In order to improve the measurement precision of the isotope ratios, and hence reduce the uncertainty in burial ages, aliquots of approximately 100g of cleaned quartz from the Bear Pit, Cobble Passage, Eye in the Sky and Octopus Room samples were processed next. Only 24g of quartz was recovered from the Eurus Rift sample so all of the Eurus Rift sample was processed. During the meteoric ^{10}Be removal process, large amounts of fine black material was released from the samples, and there was a noticeable reduction in the grainsize of the sample. After dissolution, there were large

amounts of black residue coating the insides of the beakers and large cake of white residue in the beakers (figure 8.1).

Figure 8.1. The residue after sample dissolution. Anticlockwise from top right: Eye in the Sky, Cobble Passage, Octopus Room, Bear Pit, Eurus Rift. Also shown are some vein quartz samples from another project that were processed at the same time. The beaker in the bottom centre is the process blank.

After the sample conversion process, a high pH precipitation process was tried to remove iron and titanium. This process is based in the principle that iron and titanium form insoluble hydroxides at pH 14, whereas beryllium and aluminium remain in solution (Ochs & Ivy-Ochs, 1997). This process was carried out by dissolving the sample with up to 5ml of 6M HCl and transferring the dissolved sample into 50ml centrifuge tubes containing 25ml of 12.5% sodium hydroxide (NaOH). The samples were then vortexed and allowed to stand for 1 hour before centrifuging. The supernatant, which now contains the aluminium and beryllium was then decanted into a new 50ml centrifuge tube. The precipitate was then redissolved with the minimum amount of 6M HCl necessary, and the precipitation process repeated. The Bear Pit, Cobble Passage, Eye in the Sky and Octopus Room samples needed substantially more than 5ml of 6M HCl to dissolve before precipitation, which necessitated a proportional

increase in the amount of NaOH used for precipitation. This resulted in the production of impractically large volumes of supernatant. Furthermore, another user of this this high pH precipitation method had very low beryllium yields, so the decision was made to abandon this method.

The precipitate and supernate from the high pH precipitation were recombined, the excess NaOH neutralised with HCl and the samples were allowed to dry down. The samples were then redissolved in aqua-regia. After 2 days, the Eurus Rift sample and the process blank (blank 1) had redissolved. However, there was still a substantial amount of undissolved material in the Bear Pit, Cobble Passage, Eye in the Sky and Octopus Room samples. All samples were then allowed to dry down, and the Bear Pit, Cobble Passage, Eye in the Sky, and Octopus room samples discarded. To remove the sodium added in the high pH precipitation, the Eurus Rift and process blank were dissolved in 1M HNO_3, transferred to 50ml centrifuge tubes and alkalised with 25% NH_4OH to precipitate out the beryllium and aluminium. The samples were then centrifuged and the supernate discarded. The precipitate was redissolved with 1M HNO_3, transferred back into savillex beakers and allowed to dry down. The samples were then redissolved with 10ml of 6M HCl and the beryllium and aluminium were successfully extracted using the VUW cosmogenic nuclide lab standard process.

Aluminium and beryllium isotope ratios were successfully measured, and the results for the Eurus Rift sample are recorded in tables 8.1 and 8.2. The Eurus Rift isotope ratios were blank corrected using blank 1. The high blank $^{26}Al/^{27}Al$ ratio meant that it was not possible to calculate a ^{26}Al concentration for the Eurus Rift sample.

Total aluminium concentrations were successfully measured, and the results for the Eurus Rift sample are recorded in table 8.2. However, the total aluminium concentrations for this batch of samples were much higher than the concentrations of the Eye in the Sky and Wind in the Willows samples that were processed to test the method. This suggests that the standard quartz cleaning process did not satisfactorily clean the quartz prior to dissolution

After subjecting all of the remaining samples to the modified quartz separation process as described in chapter 5.5, XRF analysis indicated that the modified separation

method was much more efficient at removing unwanted material. There was no detectable iron or aluminium present compared to the standard method, where significant quantities of iron and aluminium were present.

Aliquots of between 25g and 55g of cleaned quartz were taken from the Bear Pit, Castle Keep, Cobble Passage, Mt Owen 1, Octopus Room, Road to Nowhere, Soupmix 2, Wind in the Willows and Yelsgup samples. Due to time and funding constraints, the Soupmix 1 and Mt. Owen 2 samples were not processed for cosmogenic nuclide extraction. Both beryllium and aluminium were successfully extracted, the aluminium and beryllium isotope ratios and total aluminium concentrations successfully measured. The results are recorded in tables 8.1 and 8.2. The Bear Pit, Castle Keep, Cobble Passage, Mt Owen 1, Octopus Room, Road to Nowhere, Soupmix 2, Wind in the Willows and Yelsgup isotope ratios were blank corrected using blank 2.

^{10}Be concentrations range from 2347±859 atoms/g to 74200±1450 atoms/g and ^{26}Al concentrations range from 9741±9807 atoms/g to 247000±24900 atoms/g for the Bulmer Cavern samples. These concentrations are low compared to other burial dating studies (e.g. Granger et al, 2001; Hoblier et al, 2011). Burial ages were calculated using equation 1 and constants described in sections 1.7 and 1.8 of chapter 1, and are recorded in table 8.3. Burial ages range from 0.37±0.70Ma to 2.76± 0.42Ma. Due to the low measured cosmogenic nuclide concentrations and large uncertainties in the measured ^{26}Al/^{27}Al ratios, it was not possible to calculate meaningful burial ages for the Castle Keep and Road to Nowhere samples.

For the Mt. Owen surface sample, exposure ages were calculated using both version 2.0 of the CRONUS Earth online calculator (Marrero et al, 2016) and version 2.3 of the online calculators formerly known as CRONUS (Balco et al, 2008). The topographic shielding factor for the Mt. Owen 1 site is 0.977239, and this value was calculated using the online topographic shielding calculator that is part of the Balco online calculators. Both calculators indicate that the samples have reached saturation. Erosion rates were calculated using version 2.3 of the Balco online erosion rate calculator, and the results are reported in table 8.3.

Table 8.1. Quartz weights, amounts of ^{9}Be carrier added, ^{10}Be/^{9}Be ratios and quartz ^{10}Be concentrations. Isotope ratios measured by AMS at PRIME Lab. Analytical uncertainties are reported at 1σ precision.

Sample	Quartz weight (g)	^{9}Be carrier added (mg)	^{10}Be/^{9}Be (x 10^{-15})	Quartz [^{10}Be] (atoms/g)
Bear Pit	27.1897	0.3047	21.5±1.1	10142±959
Castle Keep	25.3414	0.3039	10.9±0.8	2347±859
Cobble Passage	54.1893	0.3021	207±4	74200±1450
Eurus Rift	24.2788	0.3008	74.5±2.2	60510±1870
Eye in the Sky	27.0796	0.2280	60.6±3.1	33290±1760
Mt Owen 1	50.5443	0.3012	460±11	180100±4500
Octopus Room	32.1905	0.3013	49.4±1.9	25950±1250
Road to Nowhere	45.8233	0.3004	18.4±1.0	4563±539
Soupmix 2	41.3809	0.3001	73.8±2.2	31930±1120
Wind in the Willows	46.0690	0.3002	66.8±1.9	25637±896
Yelsgup	45.9406	0.3000	29.5±1.8	9399±829
Blank 1		0.3000	1.38±0.59	
Blank 2		0.2995	7.93±0.69	

Table 8.2. Quartz weights, quarts ^{27}Al concentrations, ^{26}Al/^{27}Al ratios and quartz ^{26}Al concentrations. ^{27}Al concentrations measured by ICP-MS at VUW, isotope ratios measured by AMS at PRIME Lab. Analytical uncertainties are reported at 1σ precision.

Sample	Quartz weight (g)	[^{27}Al] (ppm)	^{26}Al/^{27}Al (x 10^{-15})	Quartz [^{26}Al] (atoms/g)
Bear Pit	27.1897	259±1	11.8±3.0	57340±17760
Castle Keep	25.3414	326±1	3.23±1.02	9741±9807
Cobble Passage	54.1893	281±2	41.2±3.9	247000±24900
Eurus Rift	24.2788	820±1	1.27±0.67	
Eye in the Sky	27.0796	79±1	35.5±3.4	59140±6150
Mt Owen 1	50.5443	54±0.1	995±117	1198800±141700
Octopus Room	32.1905	362±1	19.9±2.9	146000±24560
Road to Nowhere	45.8233	432±1	3.30±1.78	13530±18970
Soupmix 2	41.3809	401±3	14.1±2.8	108800±26000
Wind in the Willows	46.0690	234±1	17.8±2.9	92660±15190
Yelsgup	45.9406	222±2	10.6±2.1	43310±11100
Blank 1		2.025mg	3.36±4.84	
Blank 2		2.010mg	1.89±0.85	

Table 8.3. Cosmogenic nuclide concentrations, burial ages and erosion rates. Burial ages calculated using local production rates of P_{26} = 68.09 atoms/g/a and P_{10} = 10.05 atoms/g/a (Balco et al, 2008) and decay constants of τ_{26} = 9.83 x 10^{-7} (Nishiizumi, 2004) and τ_{10} = 4.99 x 10^{-7} (Chemeleff et al, 2009; Korschinek et al, 2009). Erosion rates calculated using the online calculators formerly known as CRONUS. Analytical uncertainties are reported at 1σ precision.

Sample	[^{26}Al] (x10^3 atoms/g)	[^{10}Be] (x10^3 atoms/g)	[^{26}Al/^{10}Be]	Burial age (Ma)	Erosion rate (mm/a)
Bear Pit	57.3±17.8	10.14±0.96	5.65±1.83	0.37±0.70	
Castle Keep	9.74±9.81	2.35±0.86	4.15±4.44	1.01±2.27	
Cobble Passage	247±25	74.2±1.5	3.33±0.34	1.47±0.33	
Eurus Rift		60.5±1.9			
Eye in the Sky	59.1±6.2	33.3±1.8	1.78±0.21	2.76±0.42	
Mt Owen 1	1120±142	180±5	6.66±0.80	N/A	0.06±0.01
Octopus Room	146±25	26.0±1.3	5.63±0.98	0.38±0.41	
Road to Nowhere	13.5±19.0	4.56±0.54	2.96±4.17	1.71±3.00	
Soupmix 2	109±26	31.9±1.1	3.40±0.82	1.42±0.60	
Wind in the Willows	92.7±15.2	25.6±0.9	3.61±0.61	1.30±0.44	
Yelsgup	43.3±11.1	9.40±0.83	4.61±1.24	0.80±0.62	

8.2. Passage dimensions and elevation data

The passage dimensions and elevation data for the sample sites in Bulmer Cavern are presented in table 8.4. The primary source of the sample site elevation data was the Bulmer Cavern survey (figure 4.7 in chapter 4). The difference in elevation between sample sites and base level streams was obtained by projecting vertically down from the sample site to the base level stream, reading off the elevation of the base level stream at that point and subtracting the elevation of the base level stream from the elevation of the sample site. Barometric altimeter readings of the elevation of some of the sample sites were recorded at the time of sampling. Additional altimeter readings of the elevations of the sample sites in the Wildcat and Soupmix Series were taken on a subsequent visit to the area.

Where there were multiple elevation readings for a particular site, the readings were averaged, and the average value will be used as the elevation of that site. The standard deviation of the average elevation will be used as an estimate of the uncertainty of the elevation of the site. For sites with only 1 elevation reading, the mean value of the differences between the elevations for the sample sites indicated by the Bulmer

Cavern survey and the barometric altimeter readings taken at those sites could be used as an estimate of the uncertainty of the elevation at that site. This approach gives an elevation uncertainty of 20m. However, the Bulmer Cavern survey data are known to contain errors that may not have been fully corrected (Main, 1990), so it was decided to use a more conservative value of 30m as the estimate of elevation uncertainty for sites where the only elevation data is from the Bulmer Cavern survey.

Table 8.4. Elevation data for the sample sites in Bulmer Cavern. Uncertainties in elevation measurements are reported at 1σ precision.

Sample site	Site elevation (m asl)	Base level elevation (m asl)	Elevation of site above base level (m)	Passage diameter (m)	Passage cross section area (m^2)
Bear Pit	1080±30	878±30	202±42	-	-
Castle Keep	1590±30	1024±30	566±42	4.5	14
Cobble Passage	1270±30	900±30	370±42	5	20
Eurus Rift	1190±42	866±30	294±52	-	-
Eye in the Sky	1164±8	884±30	276±31	5	20
Mt.Owen 1	1870±5	N/A	N/A	N/A	N/A
Octopus Room	1021±1	896±30	124±30	-	-
Road to Nowhere	1320±14	896±30	434±33	-	-
Soupmix 1	1058±18	1000±30	70±35	-	-
Soupmix 2	1090±15	1024±30	76±33	3.5	10
Wind in the Willows	1000±6	900±30	100±31	3.5	10
Yelsgup	1010±30	960±30	50±42	3	7

8.3. Analysis of the glass shard-like material

The glass shard-like material recovered from the end of Eye in the Sky passage was initially analysed using XRF to determine bulk composition. Analysis was carried out using an Olympus Vanta® portable XRF analyser on the geochem 2 mode to analyse 3 spots on the surface of a clump of the material. The average major element content was found to be 51.5 weight% SiO_2, 11.4 weight% Al_2O_3, 0.33 weight% TiO_2, 2.00 weight% Fe_2O_3, 2.66 weight% MgO, 0.04 weight% MnO_2, 17.4 weight% CaO, and 2.07 weight% K_2O. Plotting the SiO_2 and K_2O values on a total alkali silica (TAS) diagram (figure 2) suggests the material has a basaltic to basaltic andesite composition (Le Maitre, 1984).

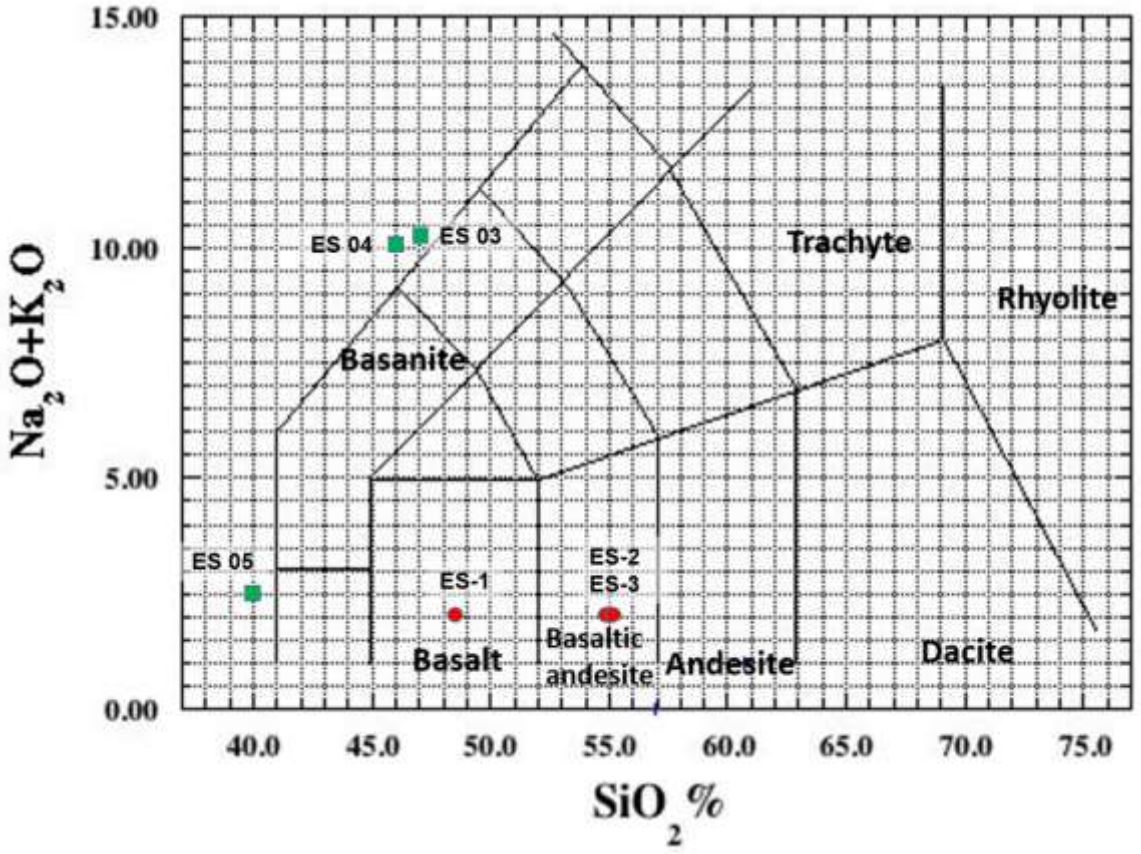

Figure 8.2. TAS plot of the glass shard-like material recovered from the end of the Eye in the Sky passage. ES-1, ES-2 and ES-3 (red circles) are the results from bulk sample XRF analysis. ES 03, ES 04 and ES 05 are the results from electron microprobe analysis of individual grains of the material.

A sub sample was taken from the clump of material that was analysed using XRF and individual grains of material were separated and mounted in epoxy resin for major element analysis with an electron microprobe. Analysis was carried out at VUW using a JEOL® 733 electron microprobe on EDS mode with an accelerating voltage of 15kV, beam current of 8nA and a beam diameter of 10µm. The results are presented in table 8.5, and a selection of those results are plotted in figure 8.2.

Table 8.5. Results of electron microprobe analysis of selected grains of the glass shard-like material from the end of Eye in the Sky passage. ES 03, ES 04 and ES 05 are plotted in figure 2. Measurements are reported in weight%.

Sample	SiO_2	CaO	Al_2O_3	K_2O	FeO	MgO	Na_2O	TiO_2	MnO	Cr_2O_3
ES 01	98.4	0.13	1.30	0.40	0.21	0.10	0.02	0.00	0.00	0.01
ES 02	91.5	0.06	4.19	1.23	0.27	0.33	0.02	0.03	0.00	0.00
ES 03	47.1	0.04	31.9	10.3	1.97	1.80	0.25	0.27	0.02	0.00
ES 04	46.2	0.11	30.7	9.78	1.46	1.87	0.29	0.74	0.02	0.04
ES 05	40.7	0.11	8.29	2.41	1.06	2.11	0.10	0.03	0.02	0.00
ES 06	79.0	0.04	9.62	2.15	2.94	2.56	0.08	0.07	0.00	0.03
ES 07	100	0.06	0.17	0.05	0.04	0.00	0.01	0.00	0.00	0.04
ES 08	21.1	23.4	10.5	1.90	3.30	4.74	0.07	0.02	0.01	0.01

8.4. Pollen

The pollen separation method described by Xun Li (personal communication) was tried on a ~1g aliquot of the fine fraction of the sample collected from the Cobble Passage. No pollen was recovered, and the only identifiable material present in the processed sample were the *lycopodium* spores that were added at the start of the process.

The method was then scaled up and tried with a ~100g aliquot of the fine fraction of the Cobble Passage sample. After processing, a trace amount of light fraction was recovered, and microscope examination of the light fraction revealed identifiable pollen grains. The abundance of identifiable pollen was less than the abundance of the added *lycopodium* spores, suggesting that there is very little pollen in the samples.

The method was then modified into the form that is described under Sample preparation: pollen in chapter 6, and this method was used to successfully extract pollen from the Bear Pit, Castle Keep, Cobble Passage, Eurus Rift, Eye in the Sky, Soupmix 2, Wind in the Willows, and Yelsgup samples. 3 slides from each extracted sample were prepared for microscope examination.

Initial examination of the slides showed that podocarp pollen and fern spores were the most abundant identifiable palynomorphs present in all of the samples. Due to time constraints, only 2 samples were examined in detail. Pollen abundances were calculated relative to total identifiable pollen counted in the slides.

Tall tree species make up 26% of the identifiable palynomorphs in the Wind in the Willows sample. The dominant taxa are of the conifer-broadleaf zone, and include the

genus *Podocarpus,* which generally prefer moist forest environments in lowland to montane altitude ranges (McGlone et al, 2017). There are also small amounts of *Dacrydium cupressinum*, and *Prumnopitys spp* present. These species also prefer moist lowland to montane environments. Also present are small amounts of the beech forest zone taxa *Fuscospora spp*, which prefer montane to sub-alpine environments (Wardle, 1991).

Tall trees make up 50% of the identifiable palynomorphs in the Castle Keep sample. Of these, 17% are conifer-broadleaf zone taxa and *Dacrydium cupressinum* is the dominant species. Beech forest zone taxa make up 33% of the tall trees, of which *Fuscospora spp* is the dominant taxa. There is also a small amount of *Lophozonia menziesii* present.

Shrubs and small tree species make up 6% of the identifiable palynomorphs in the Wind in the Willows and Castle Keep samples. *Coprosma spp*, which can be found in lowland to montane environments (Wardle, 1991) is the dominant genus.

Herb species make up 5% of the identifiable palynomorphs in the Wind in the Willows sample and 16% in the Castle Keep sample. *Poaceae* is the only genus present.

Tree ferns make up 21% of the identifiable palynomorphs in the Wind in the Willows sample. The dominant genus is *Cyathea*, which generally prefer lowland environments (Wardle, 1991; Dawson & Lucas, 2000). However, *Cyathea colensoi*, which is a very small species compared to other species of *Cyathea* can be found close to the treeline (Brownsey & Smith-Dodsworth, 2000). There are also some *Dicksonia spp* spores present in the sample. *Dicksonia* are most commonly found in lowland forests (Dawson & Lucas, 2000).

Tree ferns make up 18% of the identifiable palynomorphs in the Castle Keep sample, and only *Cyathea spp* are present.

Wetland and aquatic species make up 42% of the identifiable palynomorphs in the Wind in the Willows sample. *Gleichenia* is the dominant family in the sample. Various species of *Gleichenia* can be found in lowland to subalpine environments, usually close

to water (Brownsey & Smith-Dodsworth, 2000). There are also some *Cyperaceae* present.

Wetland and aquatic taxa make up 4% of the identifiable palynomorphs in the Castle Keep sample and *Leptospermum* is the dominant taxa.

Fern taxa make up 6% of the identifiable palynomorphs in the Castle Keep sample,

8.5. Petrographic analysis

Examination of thin sections prepared from a representative selection of clasts from each sample site showed that the sandstones consist of 70% to 90% sutured quartz grains, up to 5% feldspars, small amounts of detrital and metamorphic biotite and muscovite, iron oxide and zircon. Matrix, where present is sericite. Some of the sandstones have a foliation defined by deformed quartz grains. This foliation can be crosscut by a secondary crenulation or cleavage, which can be infilled with iron oxide (figure 8.3). The shales are carbonaceous, and some clasts contain pyrite crystals that have been replaced by haematite (figure 8.4). The quartzite cobbles found in the Thunderdome contain ~98% sutured quartz with small amounts of feldspar, biotite and muscovite. Detrital zircons are also present (figure 8.5).

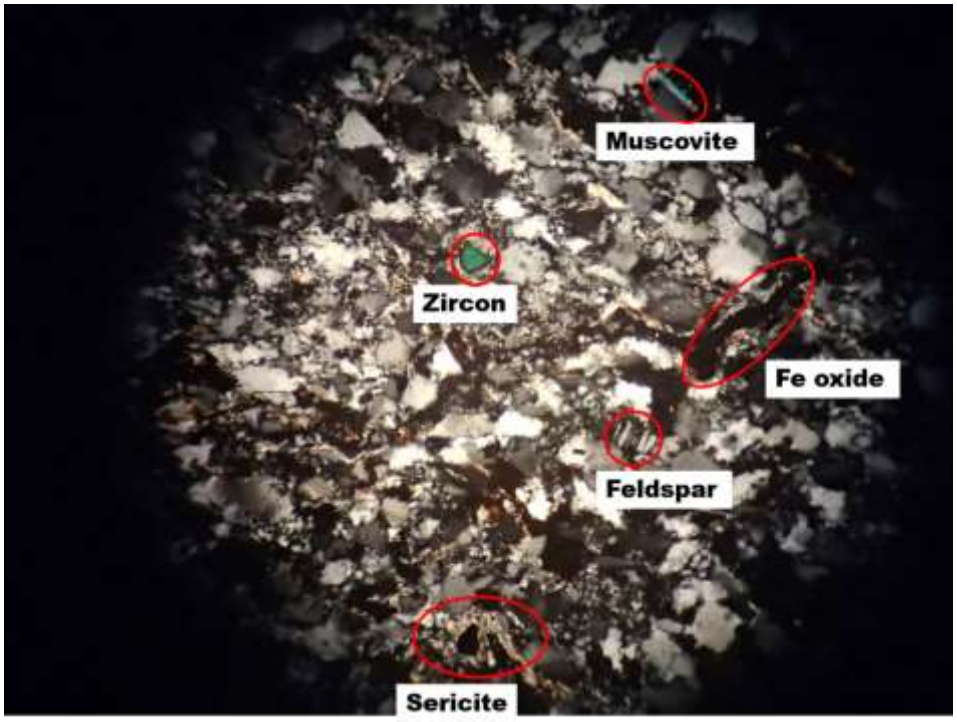

Figure 8.3. Thin section of an indurated sandstone cobble from the Bear Pit. Image is approximately 2.5mm across. X-polarised light.

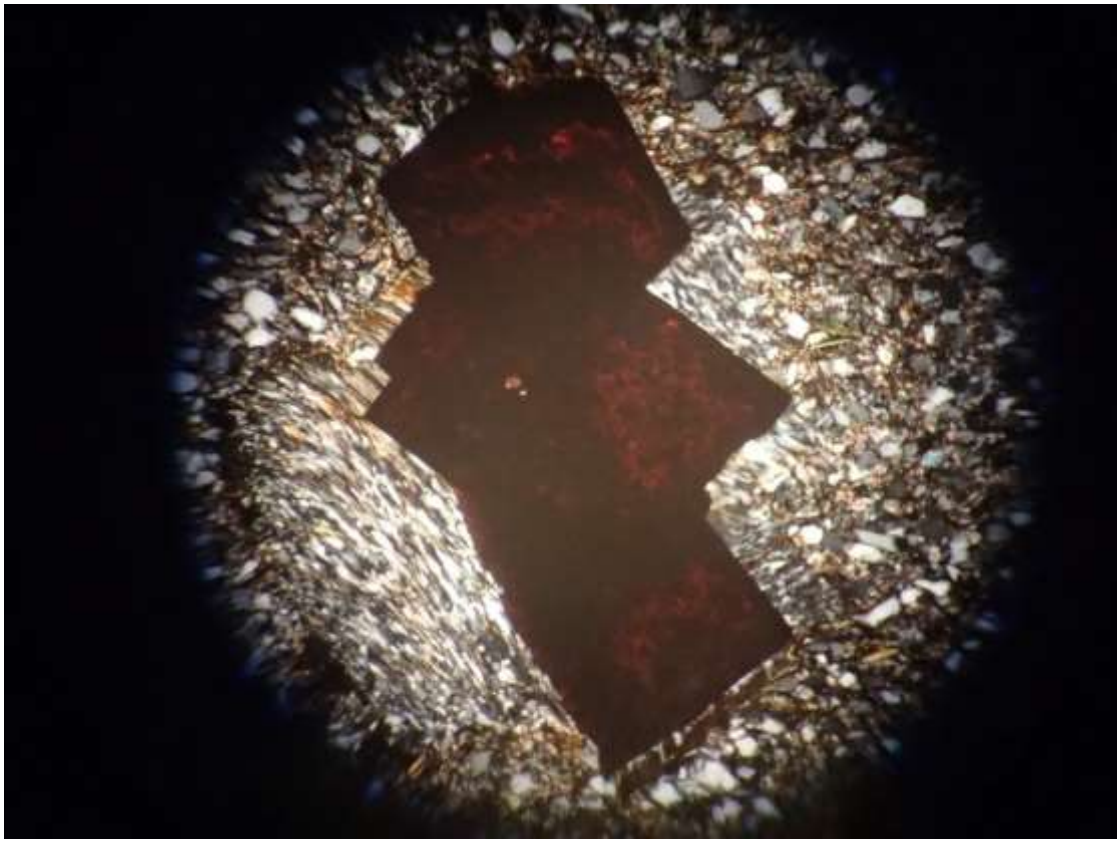

Figure 8.4. Pyrite grains that have been replaced by haematite in a shale cobble from the Octopus Room. Image is approximately 2.5mm across. X-polarised light.

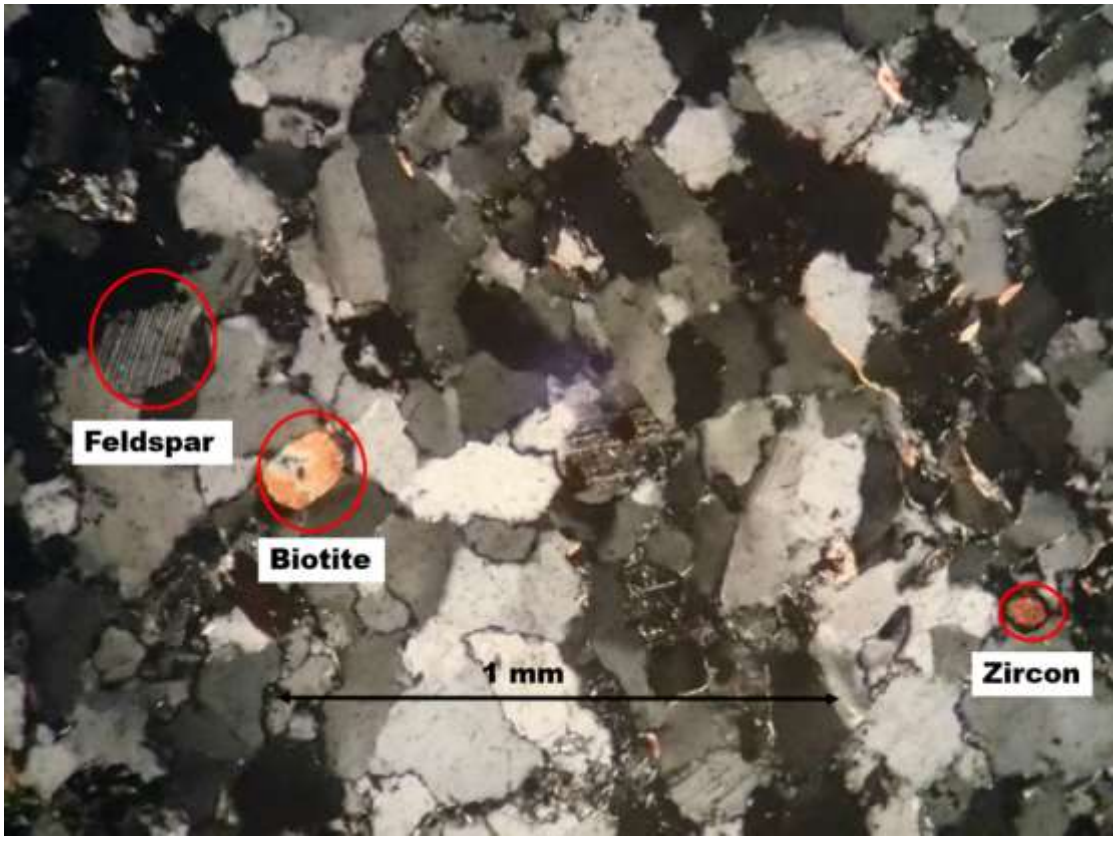

Figure 8.5. Thin section of a quartzite cobble from The Thunderdome showing sutured quartz grains, feldspar, biotite and zircon. X-polarised light.

Chapter 9. Discussion

9.1. Cosmogenic nuclide analysis

9.1.1. Surface exposure age

Because the ^{10}Be and ^{26}Al concentrations in the Mt. Owen 1 sample had reached saturation it is not possible to determine a surface exposure age for the summit of Mt. Owen beyond the fact that it must be older than the saturation age. The saturation or apparent age for a surface that can be assumed to be undergoing steady-state erosion can be calculated using the equation

$$t = \frac{1}{\left(\lambda + \left(\frac{\rho\varepsilon}{\Lambda}\right)\right)} \qquad \text{Equation 2}$$

t is the time to reach saturation, λ is the decay constant for a radioactive cosmogenic nuclide, ρ is the density of the eroding surface, ε is the surface erosion rate and Λ is the neutron mean path length (Lal, 1991). Using the surface erosion rate calculated for the summit of Mt. Owen of 0.06mm/a, a rock density of 2.7g/cm^3 and a neutron mean path length of 170g/cm^2 gives an apparent age of 10 439a. This apparent age implies that Mt. Owen is resurfaced every ~10ka.

9.1.2. Local production ratio

The local ^{26}Al/^{10}Be production ratio measured from the Mt. Owen 1 sample was 6.66 ± 0.80. Most of the uncertainty in the production ratio is due to the uncertainty in the measurement of the ^{26}Al/^{27}Al ratio. The measured ratio is indistinguishable within error from the value predicted by the Balco calculators (Balco et al, 2008) of 6.75. Even though the calculators have few southern hemisphere ^{10}Be production rate calibration sites (Putnam et al, 2010; Kaplan et al, 2010), the measured production ratio suggests that the production rate models used in the calculators give production ratios that are accurate for the study area, and therefore the predicted production ratio can be used with confidence when calculating burial ages.

It may be possible to reduce the uncertainty in the measured production ratio by processing the remaining material from the Mt. Owen 1 sample and the Mt. Owen 2 sample and using the averaged $^{26}Al/^{10}Be$.

9.1.3. Surface erosion rates

The erosion rate calculated from the measured ^{10}Be concentration in the Mt. Owen 1 sample is similar to the speleothem and cosmogenic nuclide-derived uplift rates for Paturau and Takaka (figure 2.4 in chapter 2). This suggests that the Northwest Nelson area is at, or close, to a state of equilibrium between uplift and erosion, and the speleothem basal dates and cosmogenic nuclide burial age from Paturau suggest that the Northwest Nelson area has been in a state of equilibrium for most of the Pleistocene. The higher uplift rate observed at Nettlebed cave could be explained by the fact that Nettlebed is located on the upthrown side of the Karamea Fault, and there is evidence to suggest that the Karamea Fault is still active (Grindley, 1980).

Plotting the ^{10}Be concentrations and ratios of ^{26}Al to ^{10}Be of the samples on a log-log plot of the ratio of ^{26}Al to ^{10}Be vs ^{10}Be concentration suggests that erosion rates in the catchments that fed Bulmer cavern have varied significantly over the life of the system (figure 9.1). No overall trend is evident, but the higher levels of Bulmer cavern tend to have higher observed erosion rates. All of the sampled sites in the lower levels have ^{10}Be concentrations that suggest erosion rates in the range of 0.04mm/a to 0.4mm/a. These rates are similar to basin-averaged erosion rates for the Wangapeka River catchment of 0.149±0.016mm/a (Burdis, 2014).

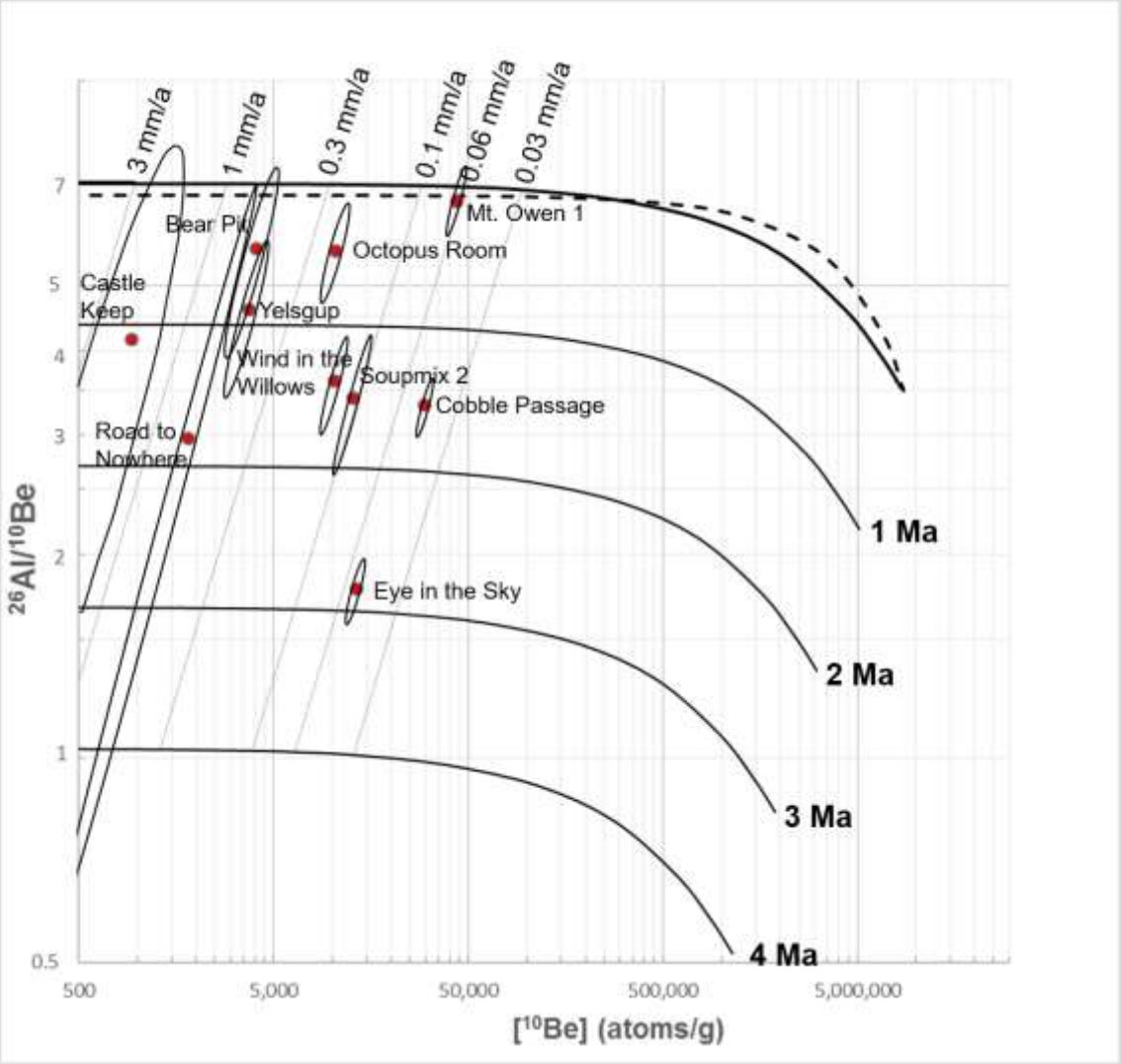

Figure 9.1. $^{26}Al/^{10}Be$ vs. $[^{10}Be]$ plot for the Bulmer cavern and Mt. Owen 1 samples. ^{10}Be concentrations have been normalised to SLHL to allow for direct comparison of erosion rates. The solid curve represents a surface undergoing steady-state erosion, the dashed curve represents a surface that is suddenly exposed to cosmic rays. Burial isochrones are plotted at 1 Ma increments. ^{10}Be concentration and $^{26}AL/^{10}Be$ uncertainties are indicated by the ellipses and are reported at 1σ precision.

9.1.4. Sediment burial ages

When sediment burial ages are plotted against elevation above modern stream level, there is wide variability in the data (figure 9.2). The large uncertainties in the burial ages of the Castle Keep and Road to Nowhere sample sites mean that they cannot be used. The Yelsgup, Soupmix 2, Wind in the Willows and Eye in the Sky sample sites follow the expected trend of increasing elevation with burial age. The Octopus Room, Bear Pit, Cobble Passage, Road to Nowhere and Castle Keep sample sites all have younger burial ages than their elevation above modern stream level would suggest.

The Bear Pit and Cobble Passage sample sites also appear to show a trend of increasing elevation with burial age.

There is no feasible way to make a cosmogenic nuclide burial age older than the true age, as this is dependent on radioactive decay of the target nuclides. Therefore, it is most likely that the burial ages for The Yelsgup, Soupmix 2, Wind in the Willows and Eye in the Sky sample sites are true abandonment ages, and the burial ages for the Octopus Room, Bear Pit and Cobble Passage are too young. There is also evidence for multiple episodes of sediment deposition at the Bear Pit sample site, which suggests that the burial age does not represent the initial abandonment age.

The main source of uncertainty in the burial ages is the uncertainty in the measurement of the ^{26}Al concentrations, which ranges from 10% for the Eye in the Sky and Cobble Passage to 100% for Castle Keep and 140% for the Road to Nowhere. The very large uncertainties in the Castle Keep and Road to Nowhere aluminium concentrations are due to very low ^{26}Al concentrations in the samples. Uncertainties in ^{10}Be concentrations range from 2% for the Cobble passage to 12% for the Road to Nowhere and 37% for Castle Keep, and again these large uncertainties are due to very low ^{10}Be concentrations in the samples from these sites.

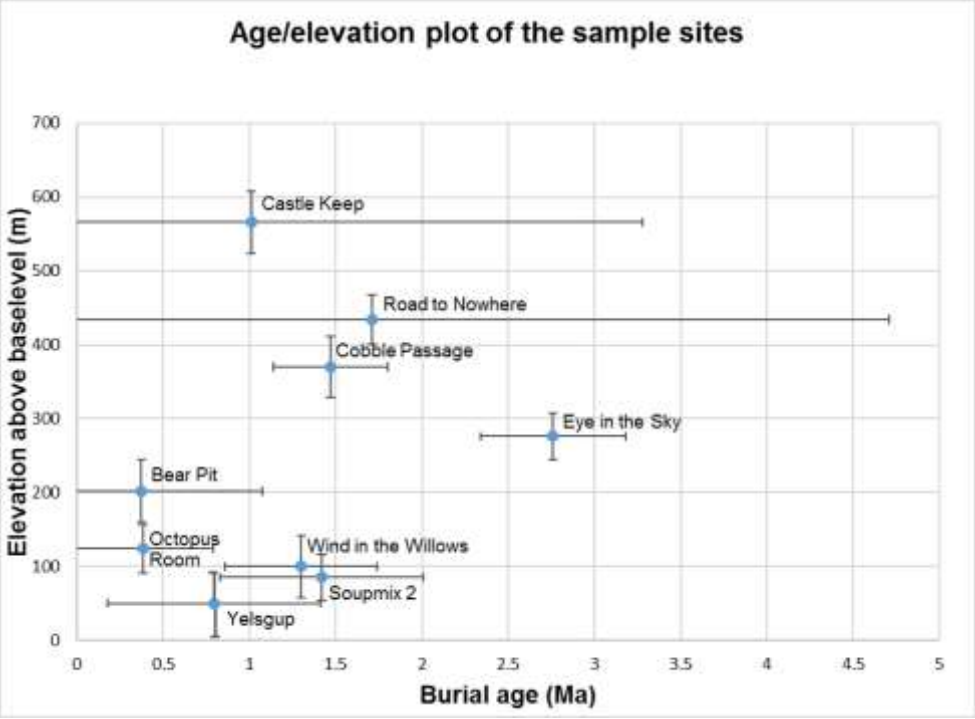

Figure 9.2. Sediment burial ages plotted against elevation above modern stream level. Burial age and elevation uncertainties are reported at 1σ precision.

9.1.5. Possible explanations for younger than expected burial ages

The Bear Pit sample site is located in the same level as the Eye in the Sky sample site and the Octopus Room sample site is located in the same level as the Wind in the Willows sample site. However, the Bear Pit sample was collected from the bottom of the canyon section of the Eye in the Sky passage whereas the Eye in the Sky sample was collected from the tube at the top of the canyon and the Octopus Room sample was collected from a blind alcove off the side of the main passage. The much younger burial ages for the Bear Pit and Octopus Room samples suggest that the Eye in the Sky and Wind in the Willows passages were reactivated after a period of abandonment.

The elevations of the Road to Nowhere, Cobble Passage and Castle Keep passages relative to the Eye in the Sky passage suggest that they should be significantly older than the Eye in the Sky passage. The Bulmer survey indicates that the Road to Nowhere and Cobble Passage are located at least 100m below the surface, which means that post-burial cosmogenic nuclide production by fast muons will be negligible even over Ma timescales. This suggests that reactivation of the Road to Nowhere and Cobble Passage after a period of abandonment is the most likely explanation for the younger than expected burial ages. Exploration of the Road to Nowhere subsequent to the collection of the sample has revealed a sediment deposit that is covered by a ~5cm thick deposit of secondary carbonate and another layer of sediment, providing further evidence for reactivation of the Road to Nowhere after a long period of abandonment.

The Bulmer Cavern survey indicates that the Castle Keep sample site is located about 30m below the surface. At this depth, cosmogenic nuclide production by spallation is in the order of 10^{-6} atoms/g/a for ^{10}Be and 10^{-5} atoms/g/a for ^{26}Al, which is insignificant even over long burial periods. However, the production of ^{10}Be by fast muons is in the order of 10^{-3} atoms/g/a and the production of ^{26}Al is in the order of 10^{-2} atoms/g/a at this depth. These production rates will make a significant contribution to cosmogenic nuclide concentrations over Ma timescales.

Using the surface erosion rate calculated from the Mt. Owen 1 sample, it would take about 1.1 Ma to erode 70m of material from the surface above the Castle Keep

passage. The production of cosmogenic nuclides by muons at depth can be estimated by using the equation

$$P_{\mu}(d) = A_1\, e^{\frac{-d}{l1}} + A_2\, e^{\frac{-d}{l2}} + A_3\, e^{\frac{-d}{l3}} \qquad \text{Equation 3}$$

d is the depth at which the production rate is being estimated, A_1 is the production rate coefficient for stopped muons, A_2 and A_3 are the production rate coefficients for fast muons, and L_1, L_2 and L_3 are the mean path lengths for stopped and fast muons (Granger & Muzikar, 2001).

Using values of $A_1 = 0.72$, $A_2 = 0.16$ and $A_3 = 0.19$ as the production rate coefficients for ^{26}Al and $A_1 = 0.09$, $A_2 = 0.02$ and $A_3 = 0.02$ as the production rates for ^{10}Be, $L_1 = 2.84$m, $L_2 = 10.34$m and $L_3 = 16.77$m for the mean path lengths (Granger & Muzikar, 2001), integrating over 10m increments with exposure times of 167ka during each increment and allowing for losses due to radioactive decay gives post-burial addition of 1450 atoms/g of ^{10}Be and 12 300 atoms/g of ^{26}Al. These values are significant compared to the measured ^{10}Be and ^{26}Al concentrations in the Castle Keep sample. This indicates that post-burial production could account for over half of the ^{10}Be and all of the ^{26}Al in the Castle Keep sample.

It may be possible to calculate a more accurate burial age for the Castle Keep sample by measuring the concentration of a stable cosmogenic nuclide such as ^{21}Ne, and using the ^{10}Be/^{21}Ne ratio to calculate the burial age.

9.1.6. Incision rate models

Using the burial age and elevation data for the sample sites that followed the expected trend of increasing burial age with elevation above modern stream level it is possible to calculate the rate of stream incision. There are two possible models for the rate of stream incision. The first model is that stream incision rates have remained constant between the time that the Eye in the Sky passage was abandoned and the present day (figure 9.3). The second model is that stream incision rates have varied between the time of abandonment of the Eye in the Sky passage and the present day (figure 9.4).

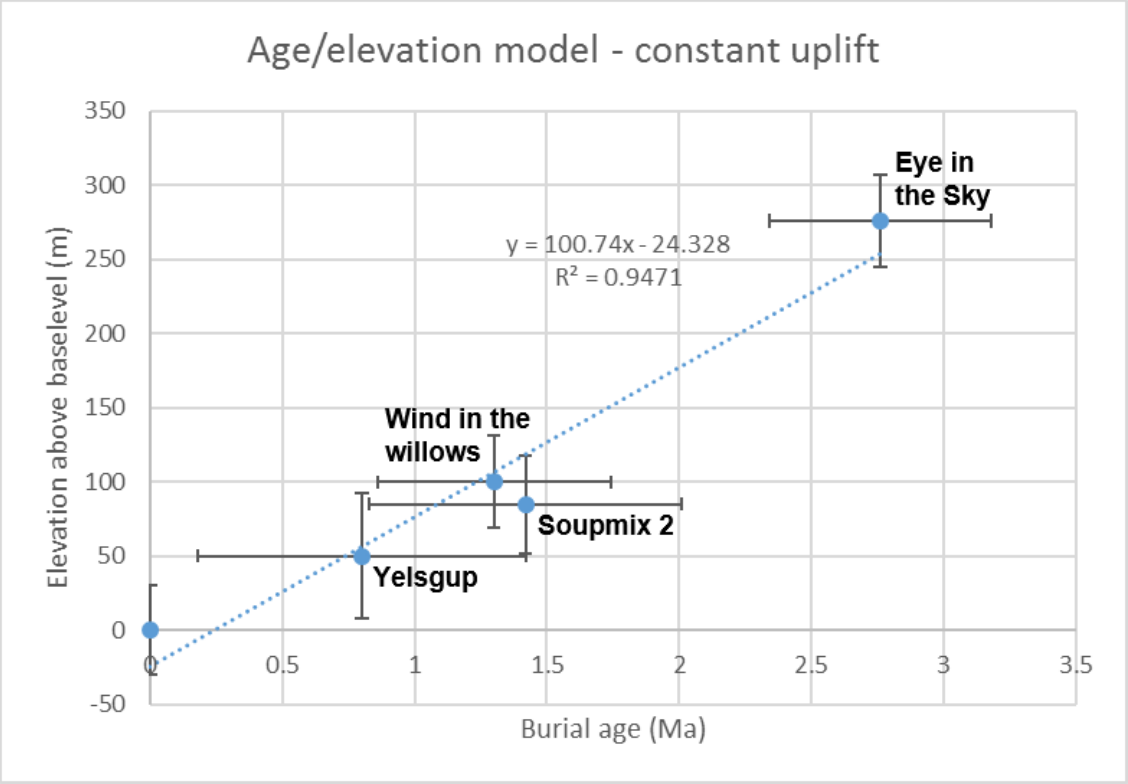

Figure 9.3. Age/elevation model for Bulmer Cavern assuming constant incision rates. Uncertainties in burial age and elevation are reported at 1σ precision.

For the constant incision model, applying least squares regression to all of the data points gives an incision rate of 0.10mm/a, and the regression coefficient of 0.95 suggests that the constant incision model is a good fit to the data. However, the regression line only passes through the Yelsgup and Wind in the Willows data points, and is only just inside the 1σ uncertainty envelope for the elevation data for the modern stream level, Soupmix 2 and Eye in the Sky sample sites. Furthermore, the incision rate is higher than the cosmogenic nuclide-derived erosion rate for Mt. Owen, and for the speleothem and cosmogenic nuclide-derived uplift rates for Northwest Nelson.

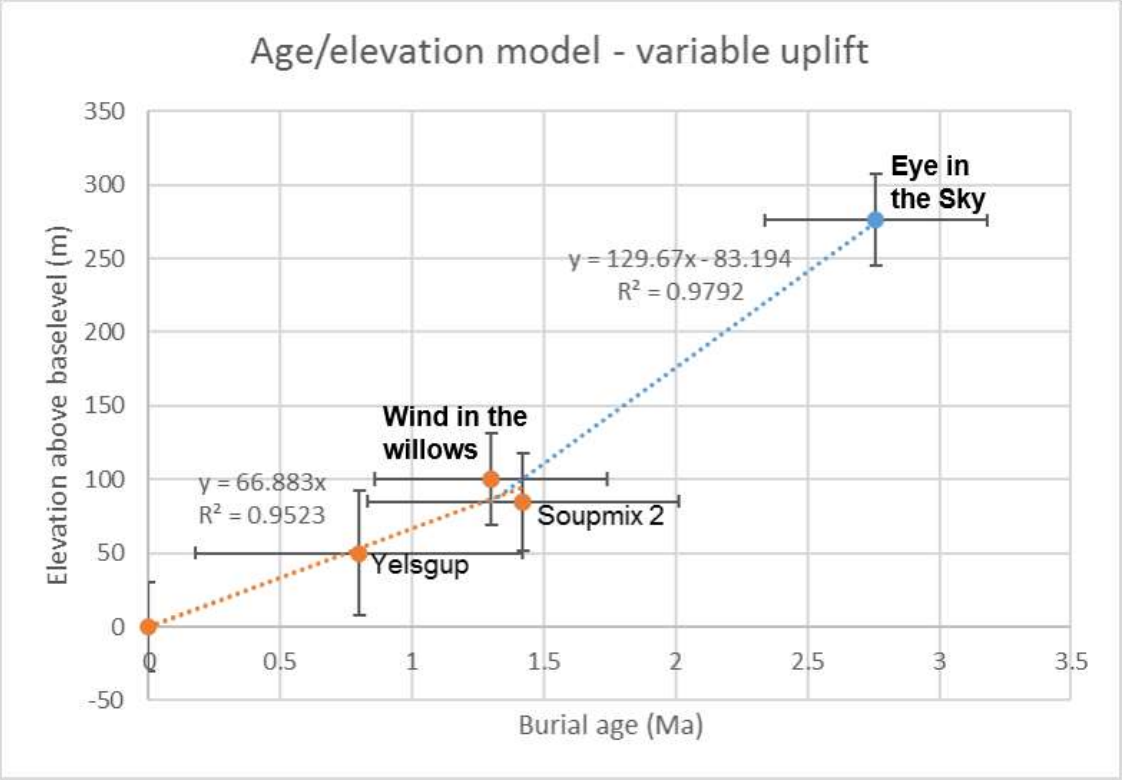

Figure 9.4. Age/elevation model for Bulmer Cavern assuming variable incision rates. Uncertainties in burial age and elevation are reported at 1σ precision.

For the variable incision rate model, applying least squares regression to the data points for the modern stream level, Yelsgup, Soupmix 2 and Wind in the Willows gives an incision rate of 0.067mm/a, and a regression coefficient of 0.95 for the time-period that covers 1.40Ma to the present-day. Applying least squares regression to the data points for Soupmix 2, Wind in the Willows and Eye in the Sky gives an incision rate of 0.13mm/a, and a regression coefficient of 0.98 for the time period that covers 1.40Ma to 2.76Ma. The higher regression coefficients and the fact that the regression lines pass through or are very close to all of the data points suggest that the variable incision rate model is a better fit to the data. However, given the large uncertainties in the data, the constant incision rate model is also a valid fit to the data.

The incision rate for the period 1.40Ma to the present-day is similar to the cosmogenic nuclide-derived erosion rate for Mt. Owen, and for the speleothem and cosmogenic nuclide-derived uplift rates for Northwest Nelson. This suggests that Northwest Nelson has been in a state of equilibrium between uplift and erosion since the mid-Pleistocene, and therefore, the stream incision rates in Bulmer cavern can be used as an estimate of uplift rates.

Even though the variable incision rate model appears to be a better fit to both the age/elevation data for Bulmer Cavern, and for the erosion and uplift rates for other parts of Northwest Nelson, the large uncertainties in the data mean it is not possible to conclusively exclude the possibility that incision rates in Bulmer Cavern have been constant. The age/elevation model can be improved by reducing the uncertainties in both the age and elevation data. The uncertainties in the elevation data can be reduced by collecting more data as discussed in chapter 8. The uncertainties in the burial age data could be reduced by measuring the concentration of ^{21}Ne in the samples, and using the ^{10}Be/^{21}Ne ratio to calculate the burial ages. This can be done without having to collect new samples because there is sufficient leftover material from all of the sample sites for measurement of ^{21}Ne concentrations.

9.2. Elevation data

With the exception of the Eurus Rift site, barometric altimeter readings are in good agreement with the elevations indicated by the Bulmer Cavern survey, and this is reflected by the fact that the relative uncertainty in the site elevations relative to sea level is less than 2%. However, the relative uncertainty in the elevation of the base level streams is at least 3.5% based on the estimate of the uncertainty in the elevation of the base level streams. Further uncertainty in the elevation of the base level streams is due to the fact that the Colonial Stream sump, which was considered to be the deepest point in the cave at an elevation of 881m asl has been connected to the Kiwi Stream (Thomas & Main, 2018). The Bulmer survey has the altitude of the connection point at an altitude of 890m asl.

When calculating the elevations of the sample sites relative to base level, the uncertainties in the elevations of the sites become significant relative to the change in elevation, adversely affecting the accuracy of the age/elevation model of Bulmer Cavern. The accuracy of the elevation data could be improved by the collection of more altimeter readings, especially from the base level streams, and from the sample sites where the only elevation data available is from the Bulmer Cavern survey.

9.3. Analysis of the glass shard-like material

Initial XRF analysis of the material suggested a basaltic to basaltic-andesitic composition. However, the colour of the material was more like rhyolitic glass which is usually pale grey in colour, whereas basaltic glass is usually brown. Furthermore, the closest volcanic centres to Northwest Nelson that have been active during the life of Bulmer Cavern are the Taranaki and North Island Central Plateau volcanic centres, which are predominantly andesitic and are not considered capable of erupting enough material to deposit significant amounts of ash in Northwest Nelson (Townsend et al, 2008).

Examination of individual shards of material using the microprobe revealed that most of the material did not look like glass shards and the major element profile did not fit any volcanic material when plotted on a TAS diagram (figure 8.2 in chapter 8).

Both the XRF and microprobe analysis indicate that the glass shard-like material recovered from Eye in the Sky passage is not volcanic in origin.

9.4. Pollen data

9.4.1. Altitudinal vegetation zones in Northwest Nelson

The native forests of Northwest Nelson can be divided into two zones based on vegetation type and altitudinal extent (figure 9.5). The lowland conifer-broadleaf zone extends from sea level up to about 600m asl at the latitude of the study area, and beech forest occupies the zone between the conifer-broadleaf zone and the tree-line (Wardle, 1991).

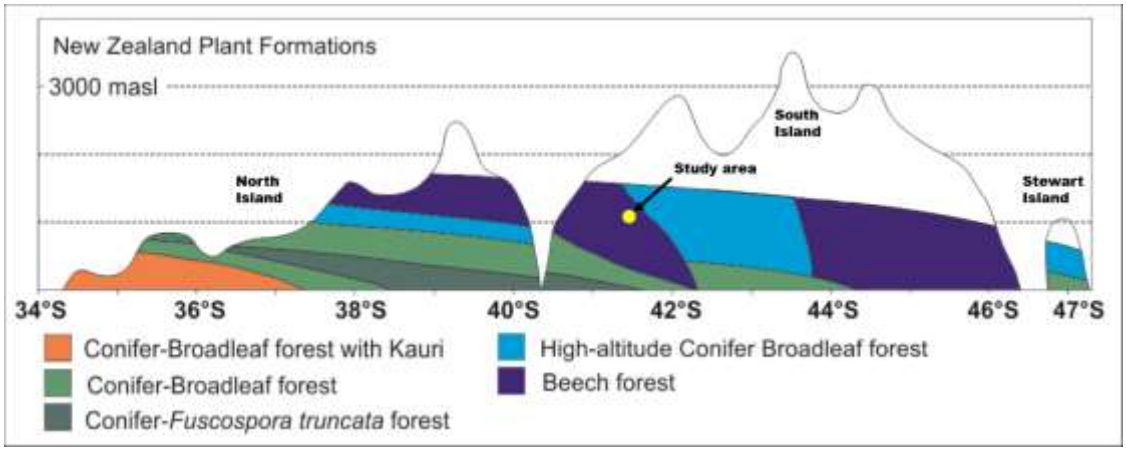

Figure 9.5 Altitudinal and latitudinal distribution of the vegetation zones of New Zealand. Modified from Schmitussen (1966) by Parra (2015).

The dominant tall tree taxa in the lowland conifer-broadleaf zone are *Dacrydium cupressinum, Prumnopitys spp, Podocarpus spp, and Darycarpus dacrydiodes.* The sub-canopy and understory consist of angiosperm trees, such as *Metrosideros spp, Weinmannia spp, Coprosma spp, Myrsine spp,* and tree ferns such as *Cyathea spp* and *Dicksonia spp.* The dominant tall tree taxa in the beech forest zone are *Fuscospora cliffortioides* in the lower parts and *Lophozonia menziesii* at the tree-line.

9.4.2. Relative pollen abundances at the sample sites

The pollen assemblage observed in the Wind in the Willows sample is consistent with a lowland conifer-broadleaf forest. The pollen assemblage observed in the Castle Keep sample is consistent with either a lowland conifer-broadleaf forest or a beech forest. However, *Fuscospora* pollen can be transported long distances by wind (McPhail & McQueen, 1983), and unlike all of the other sites sampled in Bulmer Cavern, the Castle Keep sample site is located very close to entrances. Therefore it is most likely that the *Fuscospora* pollen in the sample has been transported into the sample site by wind after the Castle Keep passage was exposed to the surface.

The pollen assemblages observed in the Castle Keep and Wind in the Willows sample suggests that the streams that formed the passage flowed through lowland conifer-broadleaf type forest before sinking underground. At the time that these passages were active, they would have been at an elevation of at least 1100m asl. In present-day Northwest Nelson, conifer-broadleaf forest is restricted to altitudes of less than 600m asl, suggesting that the treeline was at least 500m higher. A pollen-based

paleoclimate study at Adelaide Tarn, located about 50km north of Mt. Owen indicates that the elevation of the treeline has moved by a similar amount in response to climate change during the latest Pleistocene and Holocene (Parra, 2015). A speleothem-based study from Mt. Arthur, which is located about 30km north of Mt. Owen also indicates similar movements in the location of the treeline in response to climate (Hellstrom et al, 1998).

Using the present-day temperature lapse rate of 0.6^{o}C/100m (Parra, 2015), the pollen assemblages suggest that mean annual temperatures were at least 3^{o}C warmer than present during the Pliocene and early Pleistocene.

9.5. Sediment provenance

The most frequently occurring lithologies in the sediment samples are metamorphosed quartz sandstones, phyllites and black shales. Clasts of black shale recovered from the Octopus Room and Yelsgup contain pyrite crystals that have been replaced by haematite. Similar pyritic black shales occur in the Leslie, Douglas and Wangapeka Formations (Coleman, 1981; Grindley, 1980). The mineral assemblages in the sandstones are similar to the sandstone members of the Patriarch, Roaring Lion, Leslie, Douglas and Baton Formations (Coleman, 1981; Grindley, 1980). The Quartzite cobbles found in the Thunderdome have a mineral assemblage that is very similar to the Hailes Quartzite (Coleman, 1981; Grindley, 1980). Furthermore, XRF analysis of one of these cobbles prior to thin sectioning showed that it has a major and trace element profile that is very similar to what is recorded in the PETLAB database for samples of Hailes Quartzite from sites in the Rolling River, which is a tributary of the Wangapeka River that drains the northern part of the Mt. Owen massif, and at Hailes Knob, which is located north of the Karamea Fault.

The Roaring Lion, Leslie, Douglas and Baton Formations are only exposed north of the Wangapeka River. The Hailes Quartzite is exposed in the Wangapeka River valley, and there are also outcrops located as far north as Upper Takaka (figure 9.6). The closest outcrop of Roaring Lion Formation is located about 10km north of Bulmer cavern. This distance is consistent with the degree of clast roundness observed in the sediments within Bulmer cavern. Because the outcrops of Hailes Quartzite in the Wangapeka

River are at a lower elevation than the Cobble Passage, it is most likely that the quartzite cobbles found in the Thunderdome came from areas to the north of the Wangapeka River. Further evidence for a distal source for the quartzite cobbles is the fact that they are well rounded and very well indurated.

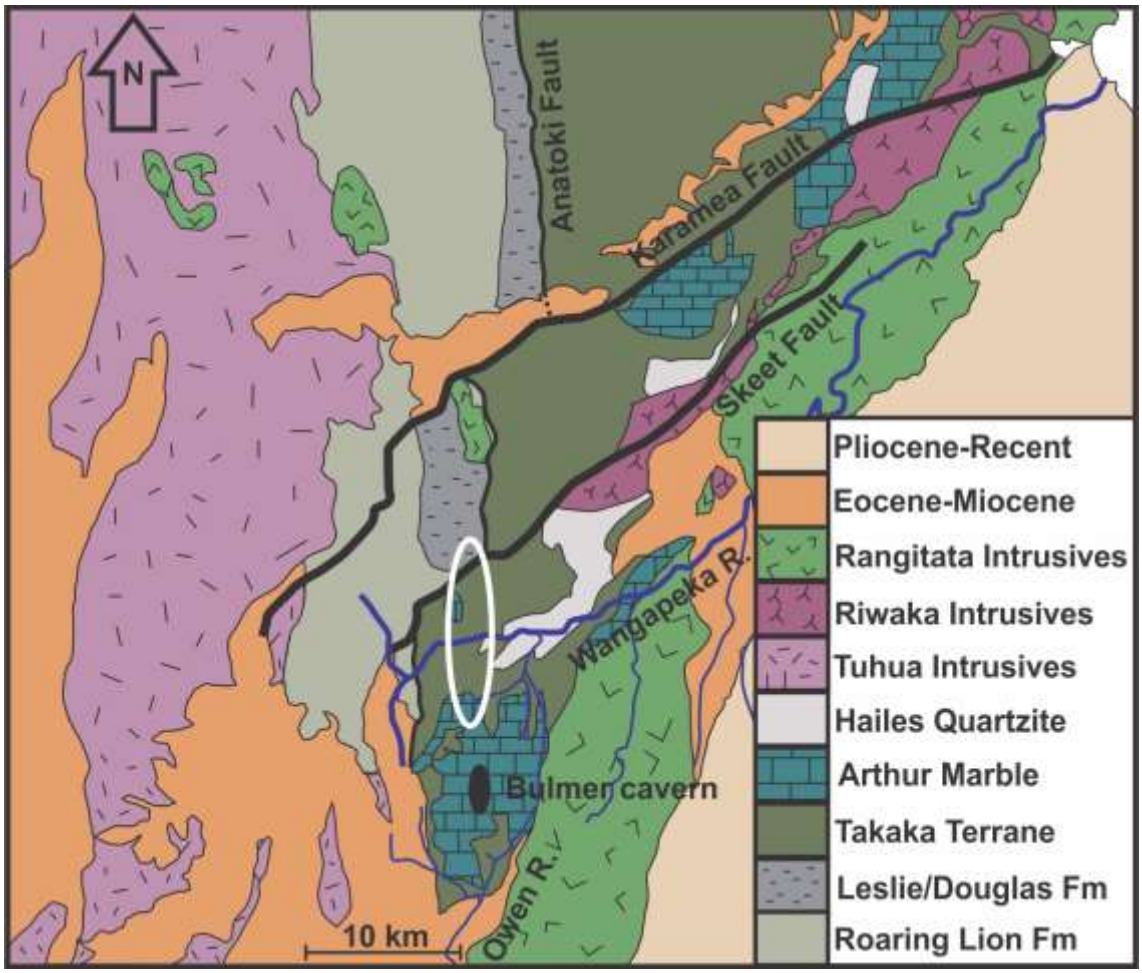

Figure 9.6. Simplified geological map of Northwest Nelson showing the location of Bulmer Cavern relative to the Wangapeka River and possible sediment source areas. The area inside the white ellipse is the potential catchment area that fed the main Upper levels and Eye in the Sky passages. Map simplified from Ratterbury et al (1998).

Due to the fact that the potential sources of the sediments found in Bulmer Cavern are widely distributed across the Northwest Nelson area it was not possible to identify a specific source area. However, some of the frequently occurring lithologies in the sediments of Bulmer Cavern are now only found north of the Wangapeka River. This suggests that the catchment that fed into Bulmer Cavern extended north of the Wangapeka River, and pre-dates the present-day surface drainage.

9.6. Paleohydrology of Bulmer cavern

9.6.1. Estimating paleoflow volumes

It is possible to use the size of the clasts present to estimate flood flow velocities by plotting the largest clast size observed in a sediment deposit on a Hjulstrom diagram Figure 9.7), and reading off the corresponding flow velocity (Boggs, 2011; Sundborg, 1956). The upper curve in figure 9.7 indicates the minimum flow velocity required to mobilise a sediment particle that is at rest. The lower curve indicates the minimum flow velocity required to keep a moving sediment particle in motion.

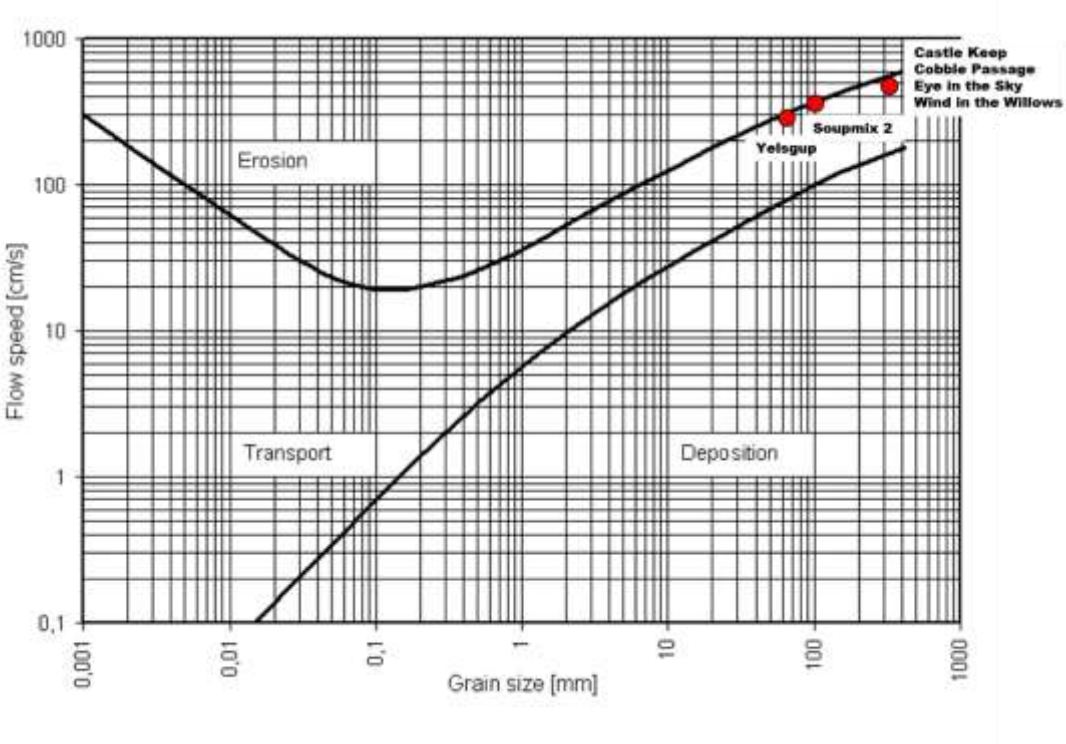

Figure 9.7. The Hjulstrom diagram with the largest clasts observed at sample sites where paleoflow velocities were estimated.

With the exception of the Wind in the Willows sample site, the largest clast sizes are found in the upper levels, suggesting that the streams that formed the upper levels were larger than the streams that formed the lower levels. Because the sediments in Bulmer Cavern are likely to have experienced multiple episodes of deposition and remobilisation, the upper curve in figure 9.7 will be used to estimate minimum flood flow velocities. Minimum flood flow velocities and flow volumes have been estimated at the Castle Keep, Cobble Passage, Eye in the Sky, Wind in the Willows, Soupmix 2 and

Yelsgup sample sites and are recorded in table 9.1. Minimum flood flow volumes were calculated by multiplying the minimum flood flow velocity by the cross section area of the passage at the sample site.

It is also possible to estimate maximum volumetric flow from measurements of passage size and hydraulic gradient because a completely flooded cave passage resembles a pipe, and volume flow in a completely full pipe is related to pipe size, hydraulic gradient and the amount of friction between the fluid in the pipe and the pipe walls. Volumetric flow in a pipe can be calculated by using the Darcy-Weisbach equation.

$$Q = \sqrt{\left(\frac{2dga^2}{f}\right)} \text{ x } \sqrt{\frac{dh}{dl}} \qquad \text{Equation 4}$$

Q is the volumetric flow, d is the pipe diameter, g is gravitational acceleration, a is pipe cross-sectional area, dh/dl is the hydraulic gradient and f is the Darcy-Weisbach friction factor (Ford & Williams, 2007; Thrailkill, 1968). In cave systems, there is a negative exponential relationship between the Darcy-Weisbach friction factor and volume flow, and at volume flows greater than about 20m^3/s the value of the friction factor becomes virtually constant at 0.116 (Lauritzen et al, 1985). If clast size indicates that flood flows exceed 20m^3/s, then f=0.116 can be used as the value of the Darcy-Weisbach friction factor for calculating maximum volume flow. The hydraulic gradient of the various levels of Bulmer Cavern can be estimated from the Bulmer Cavern survey (figure 4.7 in chapter 4).

Maximum flood flows were calculated using the Darcy-Weisbach equation with values of g=9.81m/s^2, f=0.116 and dh/dl=0.07 and the results are recorded in table 9.1.

Table 9.1. Clast size, minimum flood flow velocities, passage cross-section areas, minimum and maximum flood flow volumes.

Sample site	Max. clast size (mm)	Min. flood velocity (m/s)	Passage diameter (m)	Passage cross section area (m^2)	Min. flood volume (m^3/s)	Max. flood volume (m^3/s)
Castle Keep	300	5	4.5	14	70	102
Cobble Passage	300	5	5	20	100	154
Eye in the Sky	300	5	5	20	100	154
Wind in the Willows	300	5	3.5	10	50	64
Soupmix 2	110	4	3.5	10	40	64
Yelsgup	65	3	3	7	21	42

9.6.2. Modern analogues for the Bulmer paleocatchment

There are two other large cave systems located at similar altitudes to Bulmer Cavern in the Northwest Nelson area. The Ellis Basin-Stormy Pot-Nettlebed system is located on Mt. Arthur, and the Greenlink-Middle Earth system, which is located on Takaka Hill, approximately 60km north of Mt. Owen. The Greenlink-Middle Earth system is the only cave system in Northwest Nelson where the catchment area can be reliably estimated, and where rainfall and flow rates at the resurgence have been monitored, and this information is available on the Tasman District Council website (www.tasman.govt.nz).

The Ellis basin-Stormy Pot-Nettlebed system has a catchment area of approximately 14.5km^2, and the combined mean flow rate flow rate of the system has been estimated at 1.16m^3/s assuming a mean annual rainfall of 2750mm/a (Kahl, 2016). This gives a specific discharge of 0.08$m^3/s/km^2$. This value is consistent with the estimated flow at the Pearse Resurgence, which is the resurgence for the Ellis Basin-Stormy Pot-Nettlebed system.

The Greenlink-Middle Earth system has a catchment area of approximately 15km^2, with mean annual rainfall of approximately 2200mm/a, and at its resurgence, the mean flow rate is approximately 1m^3/s (Williams & Dowling, 1979) and flood flow rates can reach 93m^3/s (Thomas & Silverwood, 2017). The Greenlink-Middle Earth system has a mean specific discharge of 0.067$m^3/s/km^2$ and a maximum specific discharge that is approximately 90 times the mean value. Assuming that all of the large cave systems

in Northwest Nelson have similar hydrologic parameters, it may be possible to use the ratio of mean flow to flood flow as an empirical conversion factor for estimating mean annual flow in other cave systems where flood flows can be estimated.

The mean specific discharge of the Greenlink-Middle Earth system is approximately 80% of that estimated for the Ellis Basin-Stormy Pot-Nettlebed system, and this difference can be accounted for by the difference in mean annual rainfall in the catchments of the systems. This suggests that rainfall and catchment area are the primary controls on specific discharge.

The fact that both cave systems have similar specific discharges indicates that they respond in similar ways to changes in precipitation, and the fact that they are separated by 30km suggests that other cave systems at similar elevations in the Northwest Nelson area will respond in a similar way. Therefore, the Ellis Basin-Stormy Pot-Nettlebed and Greenlink-Middle Earth systems could be used as modern analogues of the paleocatchment that fed into the Bulmer system.

9.6.3. Estimated paleocatchment size of the various levels of Bulmer Cavern

Mean volume flows in the various levels in Bulmer Cavern were be estimated by dividing the maximum volume flow obtained from the Darcy-Weisbach equation by a factor of 90, and catchment area can then be estimated by dividing the estimated mean volume flow by the mean specific discharge. The results are recorded in table 9.2.

Table 9.2. Maximum flood flow, Mean annual flow and estimated catchment area for the various levels of Bulmer Cavern.

Passage	Max. flood flow (m^3/s)	Mean annual flow (m^3/s)	Catchment area (km^2)
Castle Keep	102	1.1	14
Upper Levels	154	1.7	21
Eye in the Sky	154	1.7	21
Wildcat Series	64	0.71	9
Midnight Express	64	0.71	9
Yelsgup	42	0.47	6

It must be noted that these estimates of paleocatchment size will be conservative because the empirical conversion between flood flow and mean annual flow is based on extreme (1 in 50 year) flood events. It must also be noted that these estimates are also conditional on the assumption that Bulmer Cavern had similar hydrologic parameters to the Greenlink-Middle Earth and Ellis Basin-Stormy Pot-Nettlebed systems being valid.

The estimated size of the paleocatchments of the Castle Keep, main Upper Levels and Eye in the Sky passages suggest that they extended far enough to the north to reach the Leslie and Douglas formations (figure 9.6), suggesting that the upper levels of Bulmer Cavern pre-date the Wangapeka River. The paleocatchments that fed into the Wildcat Series and the Midnight Express were small enough to have been located between the Mt. Owen massif and the Wangapeka River, suggesting that the Wangapeka River had captured a significant part of the catchment of Bulmer Cavern, and the sediment burial age from the Eye in the Sky passage indicates that this occurred sometime after 2.76Ma ago. The paleocatchment that fed into the Yelsgup passage could be accommodated entirely within the Mt. Owen massif, and is of similar size to the area of exposed karst on Mt. Owen that is located south of the present-day surface drainage divide (figure 9.8).

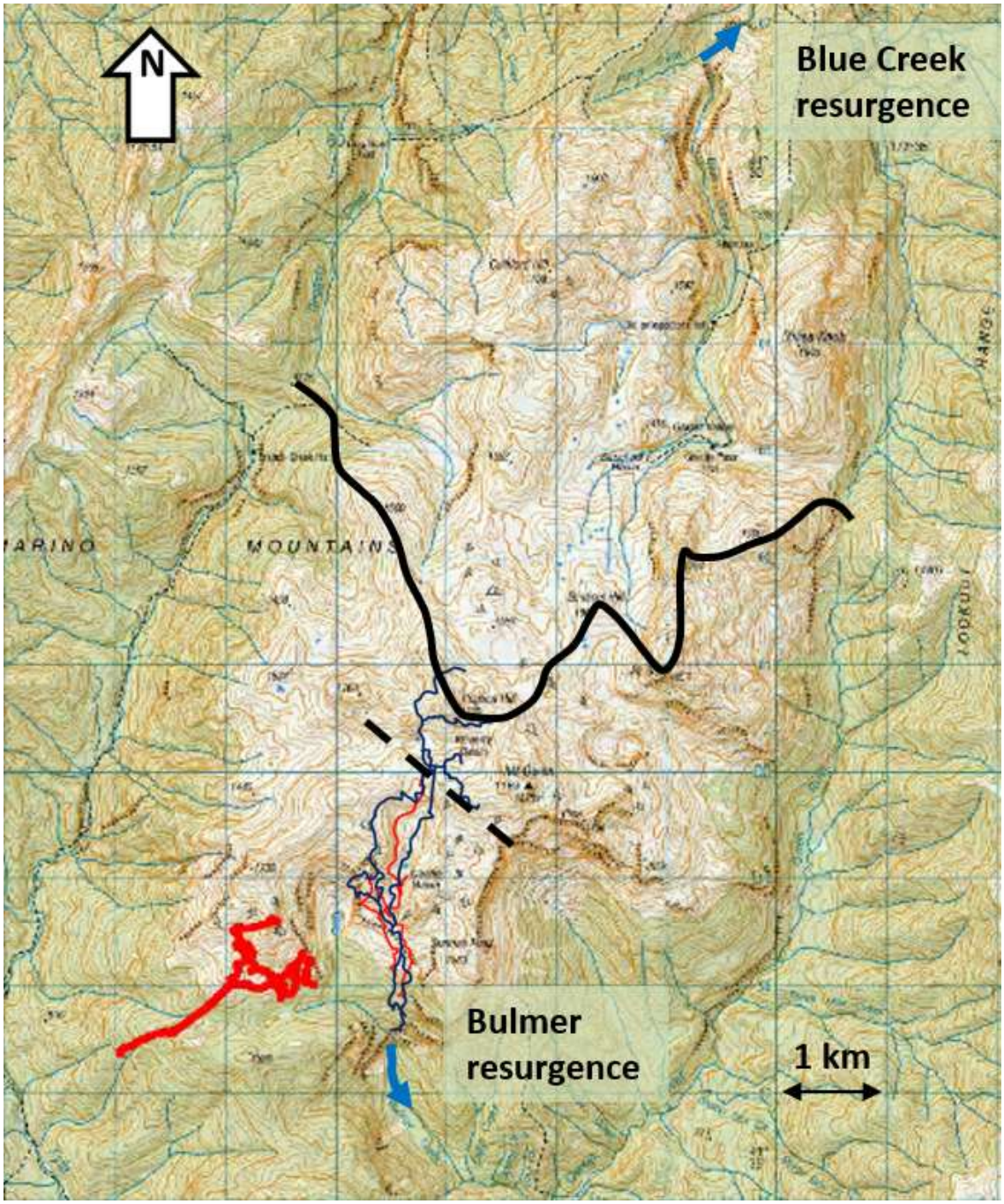

Figure 9.8. Map of the Mt. Owen massif showing the location of the surface (solid black line) and underground (dashed black line) drainage divides. Basemap: LINZ Topo50.

Chapter 10. Conclusions and opportunities for future work

10.1. Uplift rate history

The cosmogenic nuclide-derived erosion rate data from the highest and hence oldest parts of Bulmer Cavern suggest that uplift rates could have been at least an order of magnitude higher than the present day, which is consistent with the thermochronology-derived uplift rates for Northwest Nelson. The erosion rate data are also consistent with the erosion rates inferred for the Murchison Basin.

The cosmogenic nuclide-derived uplift rate for Bulmer Cavern for the period from 2.76Ma to 1.4Ma is about double the present-day uplift rate and less than a quarter of the thermochronology-derived uplift rates, indicating that there has been temporal variation in uplift rates. Because this is the only uplift rate data point in Northwest Nelson for this time period, it is not possible to say if there has been spatial variation in uplift rates. The cosmogenic nuclide-derived uplift and erosion rates for Bulmer Cavern and Mt. Owen that cover the period from 1.4Ma to the present indicate that there has been no spatial or temporal variation in uplift rates across Northwest Nelson for this time period. This study also suggests that the decrease in uplift rates in Northwest Nelson has been progressive, rather than episodic as has been suggested by Main (1988).

However, the strength of these conclusions are limited by the accuracy of the age/elevation model for Bulmer Cavern, which also allows the possibility that uplift rates have remained constant. The lack of accuracy is mostly due to the low concentration of ^{26}Al in the samples. The accuracy of the burial ages could be improved by using $^{10}Be/^{21}Ne$ burial dating. This approach may also extend the time period covered by the age/elevation model by giving a useable burial age for the Castle Keep sample. The accuracy of the elevation data can be significantly improved by collecting more altimeter readings at the sample sites and at appropriately chosen locations in the modern base-level streams.

Improving the accuracy of the burial ages will make the greatest contribution to improving the accuracy of the age/elevation model. However, this approach is also the most expensive, and will likely need additional funding. Improving the accuracy of the elevation data will make a smaller but still significant contribution to the accuracy of the age/elevation model, and this is likely to happen in the course of further exploration of Bulmer Cavern.

10.2. Paleohydrology and landscape evolution

It was not possible to identify a specific source area for the sediments found in Bulmer Cavern. However, clast lithology in the sediments of Bulmer Cavern indicate that at least some of the sediments in Bulmer Cavern are derived from source areas that were most likely north of the Wangapeka River. This suggests that the catchments that fed into Bulmer Cavern may pre-date the present-day surface drainage.

Estimates of the paleocatchment size of the various levels of Bulmer Cavern suggests that prior to 2.76Ma, these catchments could have extended north of the present-day location of the Wangapeka River. This is also consistent with the sediment provenance observations. The sediment burial ages and estimates of paleocatchment size from the Wildcat Series and Midnight Express suggest that after ~1.4Ma, the catchments may not have extended north of the present-day location of the Wangapeka River.

10.3. Paleoclimate reconstruction

All of the sediment samples processed for pollen extraction yielded identifiable pollen grains. Even though most of the samples had low pollen abundances, it was still possible to infer vegetation zones, and hence paleotemperatures for the samples that were examined in detail. More detailed examination of the samples will greatly extend the knowledge of the vegetation history of Northwest Nelson from at least the mid-Pliocene.

It was also possible to extract sufficient plant lipids from the sediment samples for further analysis. Analysis of the plant lipids may be able to provide information on paleotemperature, vegetation type and rainfall that is independent of the pollen data. Using multiple proxies for paleoclimate reconstruction can give more reliable

reconstructions than those based on single proxies. It may also be possible to use the paleoclimate data from the sediment samples to reduce the uncertainties in the cosmogenic nuclide burial ages.

10.4. ^{26}Al production rate calibration

A high precision measurement of the Mt. Owen $^{26}Al/^{10}Be$ production ratio could be combined with the ^{10}Be production rate measured at Macaulay Glacier (Putnam et al, 2010) to give an estimate of the local ^{26}Al production rate. This could make a valuable contribution to the global ^{26}Al calibration dataset.

References

Alloway, B. Lowe, D. Larsen, G. Shane, P. Westgate, J. 2013. Tephrochronology. In: Elias, S. Mock, C. (Eds) Encyclopaedia of Quaternary Science, 2nd edition vol 4. Elsevier Amsterdam p277-304

Balco, G. Rovey, C. 2008. An isochron method for cosmogenic nuclide dating of buried soils and sediments. American Journal of Science 308 p1083-1114

Balco, G. Schaefer, J. 2006. Cosmogenic-nuclide and varve chronologies for the deglaciation of southern New England. Quaternary Geochronology 1 p15-28

Balco, G. Shuster, D. 2009. ^{26}Al-^{10}Be-^{21}Ne burial dating. Earth & Planetary Science Letters 286 p570-575

Balco, G. Stone, J. Lifton, N. Dunai, T. 2008. A complete and easily accessible means of calculating surface exposure ages or erosion rates from ^{10}Be and ^{26}Al measurements. Quaternary Geochronology 3 p 174-195

Bell, C. 1970. A study of soils and vegetation on marble and on schist in the Owen Range, Nelson. Unpublished MSc thesis. Victoria University of Wellington

Bianchi, T. Canuel, E. 2011. Chemical Biomarkers in Aquatic Ecosystems. Princeton University Press Princeton

Bierman,P. 1994. Using in-situ produced cosmogenic isotopes to estimate rates of landscape evolution: a review from the geomorphic perspective. Journal of Geophysical Research 99 p13885-13896

Boggs, S. 2011. Principles of Sedimentology and Stratigraphy. Pearson Prentice Hall New Jersey

Borchers, B. Marrero, S. Balco, G. Caffee, M. Goehring, B. Lifton, N. Nishiizumi, K. Phillips, F. Schaefer, J. Stone, J. 2016. Geological calibration of spallation production rates in the CRONUS-Earth project. Quaternary Geochronology 31.p188-198

Brown, E. Trull, W. Jean-Baptiste, P. Raisbeck, G. Bourles, D. Yiou, F. Marty, B. 2000. Determination of cosmogenic production rates of ^{10}Be, ^{3}He, and ^{3}H in water. Nuclear Instruments and Methods in Physics Research B 172 p873-883

Brown, R. Brook, E. Raisbeck, G. Yiou, F. Kurz, M. 1992. Effective attenuation length of cosmic rays producing ^{10}Be and ^{26}Al in quartz: implications for exposure dating. Geophysical Research Letters 19 p369-372

Brownsey, P. Smith-Dodsworth, J. 2000. New Zealand Ferns and Allied Plants 2nd edition. David Bateman Ltd. Auckland, New Zealand

Burdis, A. 2014. Denudation rates derived from spatially-averaged cosmogenic nuclide analysis in Nelson/Tasman catchments, South Island, New Zealand. Unpublished MSc thesis. Victoria University of Wellington

Cerling, T. Craig, H. 1994a. Cosmogenic 3He production rates from 39° N to 46° N latitude, western USA and France. Geochimica et Cosmochimica acta 58 p249-255

Cerling, T. Craig, H. 1994b. Geomorphology and in-situ cosmogenic isotopes. Annual review Earth & Planetary Science 22 p273-317

Chemeleff, J. von Blankenburg, F. Kossert, K. Jakob, D. 2009. Determination of the ^{10}Be half-life by Multi Collector ICP-Mass Spectrometry and Liquid Scintillation Counting. Geochimica et Cosmochimica acta 73 A221

Coleman, A. 1981. Geological Map of New Zealand 1:63 360 part sheets S18, S19, S25 & S26 Wangapeka. Department of Scientific and Industrial Research. Wellington, New Zealand

Colinson, J. Thompson, D. 1989. Sedimentary Structures 2nd ed. Chapman & Hall London

Curl, R. 1974. Deducing flow velocity in cave conduits from scallops. National Speleological Society Bulletin 36/2 p1-5

Curl, R. 1966. Scallops and flutes. Transactions of the Cave Research Group of Great Britain 7/2 p121-160

Darville,C . 2013. Chapter 4 section 2.10 Cosmogenic nuclide analysis. In: Cook, S. Clarke, L. & Nield, J. (Eds.) Geomorphological Techniques (online edition). British Society for Geomorphology, London. ISSN: 2047-0371

Dawson, J. Lucas, R. 2000. Nature guide to the New Zealand Forest. Random House. Auckland, New Zealand

Desilets, D. Zreda, M. 2003. Spatial and temporal distribution of secondary cosmic-ray nucleon intensities and applications to in-situ cosmogenic dating. Earth & Planetary Science Letters 206 p21-42

Douka, K. Jacobs, Z. Lane, C. Grun, R. Farr, L. Hunt, C. Inglis, R. Reynolds, T. Albert, P. Aubert, P. Aubert, M. Cullen, V. Hill, E. Kinsley, L. Roberts, R. Tomlinson, E. Wulf, S. Barker, G. 2014. The chronostratigraphy of the Haua Fteah cave (Cyrenaica, northeast Libya). Journal of Human Evolution 66 p39-63

Dreybrodt, W. 2003. Viewpoints and comments on feasibility of condensation processes in hypogenic caves. Speleogenesis 1/2

Dunai, T. 2010. Cosmogenic nuclides: Principles, Concepts and Applications in the Earth Surface Sciences. Cambridge University Press, Cambridge

Dunai, T. 2001a. Influence of secular variation of the geomagnetic field on production rates if in-situ produced cosmogenic nuclides. Earth & Planetary Science Letters 193 p197-212

Dunai, T. 2000. Scaling factors for production rates of in-situ produced cosmogenic nuclides: a critical reevaluation. Earth & Planetary Science Letters 176 p157-169

Dunai, T. Wijbrans, J. 2000. Long-term cosmogenic ^{3}He production rates (152 ka-1.35 Ma) from ^{40}Ar/^{39}Ar dated basalt flows at 29^{o} N latitude. Earth & Planetary Science Letters 176 p147-156

Dunne, J. Elmore, D. Muzikar, P. 1999. Scaling factors for the rates of production of cosmogenic nuclides for geometric shielding and attenuation at depth on sloped surfaces. Geomorphology 27 p3-11

Elmore, D. Phillips, F. 1987. Accelerator Mass Spectometry for Measurement of Long-Lived Radioisotopes. Science 236 (4801) p543-550

Fairchild, I. Frisia, S. Borsato, A. Tooth, A. 2006. Speleothems. In: Nash, D. McLaren, S. (Eds) Geochemical Sediments and Landscapes. Blackwells, Oxford

Ford, D. Williams, P. 2007. Karst Hydrology and Geomorphology. John Wiley & Sons Ltd. Chichester, England

Fyfe, H. 1968. Geology of the Murchison Subdivision. New Zealand Geological Survey Bulletin 36

Ghisetti, F. Sibson, R. Woperis, P. 2017. In: Baker, J. & Rowe, M. (eds). Abstracts, Geosciences 2017, Auckland. Geoscience Society of New Zealand Miscellaneous Publication 134A p39

Gosse, J. Phillips, F. 2001. Terrestrial in-situ cosmogenic nuclides: theory and application. Quaternary Science Reviews 20 p1475-1560

Gosse, J. Evanson, E. Klein, J. Lawn, B. Middleton, R. 1995. Precise cosmogenic ^{10}Be measurements in western North America: support for a global Younger Dryas cooling event. Geology 23 P877-880

Granger, D. Fabel, D. Palmer, A. 2001. Pliocene-Pleistocene incision of the Green River, Kentucky, determined from radioactive decay of cosmogenic ^{26}Al and ^{10}Be in Mammoth Cave sediments. Geological Society of America Bulletin 113/7

Granger, D. Kirchner, J. Finkel, R. 1997. Quaternary downcutting rate of the new River, Virginia, measured from differential decay of cosmogenic ^{26}Al and ^{10}Be in cave deposited alluvium. Geology 25/2 p107-110

Granger, D. Muzikar, P. 2001. Dating sediment burial with in-situ produced cosmogenic nuclides: theory, techniques and limitations. Earth & Planetary Science Letters 188 p269-281

Grindley, G. 1980. Geological Map of New Zealand 1:63 360 sheet S13 Cobb. Department of Scientific and Industrial Research. Wellington, New Zealand

Heisinger, B. Lal, D. Jull, A. Kubik, P. Ivy-Ochs, S. Knie, K. Nolte, E. 2002a. Production of selected cosmogenic nuclides by muons: 2. Capture of negative muons. Earth & Planetary Science Letters 200 p357-369

Heisinger, B. Lal, D. Jull, A. Kubik, P. Ivy-Ochs, S. Neumann, S. Knie, K. Lazarn, V. Nolte, E. 2002b. Production of selected cosmogenic nuclides by muons: 1. Fast muons. Earth & Planetary Science Letters 200 p357-369

Hellstrom, J. McCulloch, M. Stone, J. 1998. A detailed 31,000-Year Record of Climate and Vegetation Change from the Isotope Geochemistry of Two New Zealand Speleothems. Quaternary Research 50 p167-178

Hoblier, F. Hauselmann, P. Kubik, P. 2011. Cosmogenic nuclide dating of cave deposits of Mount Granier (Hauts de Chartreuse Nature Reserve, France): morphogenic and paleogeographical implications. Geomorphologie: relief, processus, environment 17/4 p395-406

Hoffmann, H. Beer, J. Bonani, G. von Gunten, H. Raman, S. Suter, M. Walker, R. Wolfli, W. Zimmermann, D. 1987. ^{10}Be: half-life and AMS-standards. Nuclear Instruments and Methods in Physics Research B 29 p32-46

Hyatt, O. Shulmeister, J. Smart, C. 2007. A Reconnaissance Study of Glaciation on the Owen Massif, Northwest Nelson, New Zealand. Quaternary Australasia 24/2 p11-18

Jones, R. 2015. Late Cenozoic behaviour of two Transantarctic Mountain outlet glaciers. Unpublished PhD thesis. Victoria University of Wellington

Kahl, F. 2016. Observations on the hydrology of caves under Mt. Arthur: a caver's perspective. New Zealand Speleological Bulletin 11/211 p218-221

Kaplan, M. Strelin, J. Schaefer, J. Denton, G. Finkel, R. Schwartz, R. Putnam, A. Vandergoes, M. Goehring, B. Travis, S. 2011. In-situ cosmogenic ^{10}Be production rate at Lago Argentino, Patagonia: Implications for late-glacial climate chronology. Earth & Planetary Science Letters 309 p21-32

King, P. 2000. Tectonic reconstructions of New Zealand: 40Ma to the present. New Zealand Journal of Geology and Geophysics 43/4 p611-638

Klein, J. Giegengack, R. Middleton, R. Sharma, P. Underwood, J. Weeks, W. 1986. Revealing histories of exposure using in-situ produced ^{26}Al and ^{10}Be in Libyan desert glass. Radiocarbon 28 p547-555

Klimchouk, A. 2004. Speleogenesis. In Gunn, J. (Ed) Encyclopedia of Caves and Karst Science. Taylor and Francis Inc. New York

Kohl, C. Nishiizumi, K. 1992. Chemical isolation of quartz for measurement of in-situ-produced cosmogenic nuclides. Geochimica et Cosmochimica acta 56 p3583-3587

Korschinek, G. Bergmaier, A. Dillmann, I. Faestermann, T. Gerstmann, U. Knie, K. von Gostomski, C. Maiti, M. Poutivtsev, M. Remmert, A. Rugel, G. Wallner, A. 2009. Determination of the ^{10}Be half-life by HI-IRD and liquid scintillation counting. Geochimica et Cosmochimica acta 73 A685

Kubik, P. Ivy-Ochs, S. Masarik, J. Frank, M. Schluchter, C. 1998. ^{10}Be and ^{26}Al production rates deduced from an instantaneous event within the dendro-calibration curve, the landslide of Kofels, Otz Valley, Austria. Earth & Planetary Science Letters 161 p231-241

Kurz, M. Colodner, D. Trull, T. Morre, R. O'Brien, k. 1990. Cosmic ray exposure dating with in-situ produced ^{3}He: results from young Hawaiian lava flows. Earth & Planetary Science Letters 97 p177-189

Lal, D. 1991. Cosmic ray labelling of erosion surfaces: in-situ nuclide production rates and erosion models. Earth & Planetary Science Letters 104 p424-439

Lal, D. Arnold, J. 1985. Tracing quartz through the environment. Proceedings of the Indian Acedemy of Science, Earth and Planetary Science 94 p1-5

Lauritzen, S-E. Abbot, J. Arnesen, R. Crossley, G. Grepperud, D. Ive, A. Johnson, S. 1985. Morphology and Hydraulics of an Active Phreatic Conduit. Cave Science 12/3 p139-146

Le Maitre, R. 1984. A proposal by the IUGS subcommission on the systematics of igneous rocks for a chemical classification of volcanic rocks based on total alkali silica (TAS) diagram. Australian Journal of Earth Science 31 p243-255

Leonard, G. Begg, J. Wilson, C. 2010. Geology of the Rotorua Area. Institute of Geological and Nuclear Sciences 1:250 000 geological map 5. 1 sheet + 67p Institute of Geological and Nuclear Sciences Ltd. Lower Hutt, New Zealand

Leya, I. Buselmann, H. Baur, H. Wieler, R. Gloris, M. Neurmann, S. Michel, R. Sudbrock, F. Herpers, U. 1998. Cross sections for the proton-induced production of He and Ne isotopes from magnesium, aluminium, and silicon. Nuclear Instruments and Methods in Physics Research B 145 p449-458

Leya, I. Lange, H-J. Neumann,S. Wieler, R. Michel,R. 2000. The production of cosmogenic nuclides in stony meteoroids by galactic cosmic ray particles. Meteorics & Planetary Science 35 p259-286

Lifton, N. Bieber, j. Clem, J. Duldig, M. Evanson, P. Humble, J. Pyle, R. 2005. Addressing solar modulation and long-term uncertainties in scaling secondary cosmic rays for in-situ cosmogenic nuclide applications. Earth & Planetary Science Letters 239 p140-161

Lihou, J. 1993. The structure and deformation of the Murchison Basin, South Island, New Zealand. New Zealand Journal of Geology and Geophysics 36/1 p95-105

Lihou, J. 1992. Reinterpretation of seismic reflection data from the Moutere Depression, Nelson region, South Island, New Zealand. New Zealand Journal of Geology and Geophysics 45/4 p477-490

Lyons, R. 1988. Dating of Bulmer Speleothems. New Zealand Speleological Bulletin 8/144-145 p146-149

Lyons, R. 1983. A Study of Paleomagnetism in New Zealand Cave Deposits. Unpublished MSc thesis. Auckland University Geography Department.

McGlone, M. Richardson, S. Burge, O. Perry, G. Wilmshurst, J. 2017. Palynology and the Ecology of the New Zealand Conifers. Frontiers in Earth Science 5/94

McKay, K. 1990. Mt. Owen Expedition, New Year 1989 – 27 Kilometers and… New Zealand Speleological Bulletin 8/154-156 p422-429

McPhail, M. McQueen, D. 1983. The value of New Zealand pollen and spores as indicators of Cenozoic vegetation and climate. Tuatara 26/12 p37-59

Main, L. 2017. New Zealand Cave statistics. New Zealand Speleological Bulletin 11/212-213 p265

Main, L. 1988. Speleogenesis of Bulmer Cavern. New Zealand Speleological Bulletin 8/144-145 p141-145

Main, L. 1990. The Bulmer survey – Order out of Chaos. New Zealand Speleological Bulletin 8/154-156 p455-458

Marlow, J. Farrimond, P. Rosell-Mele. A. 2001. Analysis of lipid biomarkers in sediments from the Benguela Current coastal upwelling (Site 1084). In: Wefer, G. Berger, W. Richter, C. (Eds) Proceedings of the Ocean Drilling Program, Scientific Results 175 p1-26

Marreno, S. Phillips, F. Borchers, B. Lifton, N. Aumer, R. Balco, G. 2016. Cosmogenic nuclide systematics and the CRONUScalc program. Quaternary Geology 31 p160-187

Masarick,J. Beer, J. 1999. Simulation of particle fluxes and cosmogenic nuclide production in the Earth's atmosphere. Journal of Geophysical Research 104D p12099-12111

Masarick, J. Reedy, R. 1994. Effects of bulk composition on nuclide production processes in meteorites. Geochimica et Cosmochimica acta 58 p5307-5317

Masarick, J. Reedy,R. 1995. Terrestrial cosmogenic nuclide production systematics calculated from numerical simulations. Earth & Planetary Science Letters 136 p381-395

Masarick, J. Reedy, R. 1996. Monte Carlo simulations of in-situ produced cosmogenic nuclides. Radiocarbon 38 p163-164

Mildenhall, D. Suggate, R. 1981. Palynology and age of the Tadmore Group (late Miocene-Pliocene) and Porika Formation (early Pleistocene), South Island, New Zealand. New Zealand Journal of Geology and Geophysics 24 p515-528

Niedermann, S. 2002. Cosmic-ray-produced noble gases in terrestrial rocks: dating tools for surface processes. Reviews of Mineral Geochemistry 47 p731-784

Nishiizumi, K. 2004. Preparation of ^{26}Al AMS standards. Nuclear Instruments and Methods in Physics Research B 223 p388-392

Nishiizumi, K. Imamura, M. Caffee, M. Southon, J. Finkel, R. McAninch, J. 2007. Absolute calibration of Be- 10 AMS standards. Nuclear Instruments and Methods in Physics Research B 258 p403-413

Nishiizumi, K. Finkel, R. Klein, J. Kohl, C. 1996. Cosmogenic production of ^{7}Be and ^{10}Be in water targets. Journal of Geophysical Research 101 p22225-22232

Norris, R. Cooper, A. 2001. Late Quaternary slip rates and their significance for slip partitioning on the Alpine fault, New Zealand. Journal of Structural Geology 23/2-3 p507-520

Norton, K. 2008. Response of the landscape in the Swiss Alps to the late glacial to Holocene climate transition. Unpublished PhD thesis. University of Hannover.

NZMS. 1973. Rainfall normal for New Zealand 1941-1970. New Zealand Meteorological Service Miscellaneous publication 145. Government Printer, Wellington New Zealand

Ochs, M. Ivy-Ochs, S. 1997. The chemical behaviour of Be, Al, Fe, Ca, and Mg during AMS target preparation from terrestrial silicates modelled with chemical speciation calculations. Nuclear Instruments and Methods in Physics Research B 123 p235-240

Palmer, A. 1991. Origin and morphology of limestone caves. Geological Society of America Bulletin 103 p1-21

Parra, I. 2015. Using pollen records from New Zealand and southern Chile to reconstruct New Zealand climate variability. Unpublished PhD thesis. Victoria University of Wellington

Patterson, J. 1988. Discovery of Bulmer Cavern, Mt. Owen, January 1985. New Zealand Speleological Bulletin 8/144-145 p105-112

Peterson, G. 1976. Pollen Analysis and the Origin of Cave Sediments in the Central Kentucky Karst. National Speleological Society Bulletin 38/3 p53-58

Placzek, C. Granger, D. Caffee, M. 2007. Radiogenic Al-26 chronometry of evaporates. Geochimica et Cosmochimica acta 71 A765

Putnam, A. Schaefer, J. Barrell, D. Vandergoes, M. Denton, G. Kaplan, M. Finkel, R. Schwartz, R. Goehring, B. Kelley, S. 2010. In situ cosmogenic ^{10}Be production-rate calibration from the Southern Alps, New Zealand. Quaternary Geochronology 5 p392-409

Rattenbury, M. Townsend, D. Johnston, M. (Compilers). 2006. Geology of the Kaikoura Area. Institute of Geological and Nuclear Sciences 1:250 000 geological map 13. 1 sheet + 70p. Institute of Geological and Nuclear Sciences Ltd. Lower Hutt, New Zealand

Rattenbury, M. Cooper, R. Johnston, M. (Compilers) 1998. Geology of the Nelson Area. Institute of Geological and Nuclear Sciences 1:250 000 geological map 9. 1 sheet + 102p. Institute of Geological and Nuclear Sciences Ltd. Lower Hutt, New Zealand

Richards, D. Dorale, J. 2003. Uranium-series Chronology and Environmental Applications of Speleothems. Reviews in Mineralogy and Geochemistry 52/1 p407-460

Ryan, M. Dunbar, G. Vandergoes, M. Neil, H. Hannah, M. Newnham, R. Bostock, H. Alloway, B. 2012. Vegetation and climate in Southern Hemisphere mid-latitudes since 210 ka: new insights from marine and terrestrial pollen records from New Zealand. Quaternary Science Reviews 48 p80-98

Seward, D. 1989. Cenozoic basin histories determined by fission-track dating of basement granites, South Island, New Zealand. Chemical Geology: Isotope Geoscience section 79/1 p31-48

Sharma, P. Middleton, R. 1989. Radiogenic production of ^{10}Be and ^{26}Al in uranium and thorium ores: implications for studying terrestrial samples containing low levels of ^{10}Be and ^{26}Al. Geochimica et Cosmochimica acta 53 p709-716

Schmithusen, J. 1966. Problems of vegetation history in Chile and New Zealand. Plant Ecology 13 p189-206

Sisterson, J. 2005. Cross-section measurements for proton and neutron induced reactions needed to understand cosmic ray interactions on Earth and in space. In: Haight, R. Chadwick, M. Kawano, T. Talou, P. (Eds) International conference on nuclear data for science and technology 769, Santa Fe: AIP conference proceedings p1596-1599

Staiger, J. Gosse, J. Toracinta, R. Oglesby, B. Fastook, J. Johnson, J. 2007. Atmospheric scaling of cosmogenic nuclide production: Climate effect. Journal of Geophysical Research 112

Stone, J. 2000. Air pressure and cosmogenic isotope production. Journal of Geophysical Research 105 p23573-23579

Suggate, P. 1984. Geological map of New Zealand 1:50 000 Sheet M29AC Mangles Valley. Department of Scientific and Industrial Research. Wellington, New Zealand

Suggate, R. 1978. Notes on the Murchison Depression and its hydrocarbon occurrences. New Zealand Geological Survey report M70

Suggate, R. 1974. Coal ranks in relation to depth and temperature in Australian and New Zealand oil and gas wells. New Zealand Journal of Geology and Geophysics 17 p149-167

Sundborg, A. 1956. The River Klaralven: a Study of Fluvial Processes. Geografiska Annaler Ser A 38 p197

Tasler, R. 1998. Speleothems of giant domes of Bohemia Cave. New Zealand Speleological Bulletin 10/188-192 p193-196

Tasler, R. Tomasek, J. Kracik, V. Sustek, B. Loskot, P. Fridrich, L. Tasler, P. Benes, L. Havlicek, D. 1997. The 1990 Czech Expedition to Mt. Owen, Northwest Nelson. New Zealand Speleological bulletin 10/182 p32-59

Thrailkill, J. 1968. Chemical and Hydrologic Factors in the Excavation of Limestone Caves. Geological Society of America Bulletin 79 p19-46

Thomas, M. 2016. One Stream/Two Coasts. New Zealand Speleological Bulletin 11/211 p227

Thomas, M. Main, L. 2018. Exploration news 2018. New Zealand Speleological Bulletin 11/215 p439

Thomas, M. Silverwood, N. 2017. Caves: Exploring New Zealand's Subterranean Wilderness. Whio Publishing. Wellington, New Zealand

Thomas, M. Silverwood, N. 2016. What Goes On In The Shadows: A Positive Dye Trace between Bulmer Cavern and Blue Creek. New Zealand Speleological Bulletin 11/211 p212-217

Townsend, D. Vonk, A. Kamp, P. 2008. Geology of the Taranaki Area. Institute of Geological and Nuclear Sciences 1:250 000 geological map 7. 1 sheet + 102p. Institute of Geological and Nuclear Sciences Ltd. Lower Hutt, New Zealand

Traverse, A. 2007. Paleopalynology. 2nd edition. Springer Dordrecht

Vermeesch, P. Heber, V. Strasky, S. Kober, F. Schaefer, J. Baur, H. Schluchter, C. Wieler, R. 2008. Cosmogenic ^{3}He and ^{21}Ne measured in artificial quartz targets after one year of exposure in the Swiss Alps. Geophysical Research Abstracts 10 p1607-7962

von Blankenburg, F. Belshaw, N. O'Nions, R. 1996. Separation of ^{9}Be and cosmogenic ^{10}Be from environmental materials and SIMS isotope dilution analysis. Chemical Geology 129 p93-99

Wardle, P. 1991. Vegetation of New Zealand. Cambridge University Press. Cambridge

Wellman, H. 1979. An Uplift Map for the South Island of New Zealand, and a Model for Uplift of the Southern Alps. In: Walcott, R. & Cresswell, M. (Eds) The Origin Of The Southern Alps. Royal Society of New Zealand Bulletin 18 p13-20

White, W. 1988. Geomorphology and Hydrology of Karst Terrains. Oxford University Press. Oxford

Williams, K. Smith, G. 1977. A Critical evaluation of the Application of Amino Acid Racemisation to Geochronology and Geothermometry. Origins of Life 8 p1-44

Williams, P. 2017. New Zealand Landscape: Behind the Scene. Elsevier Inc.

Williams, P 1992. Karst of New Zealand. In: Soons, J. & Selby, M. (Eds) Landforms of New Zealand (2nd edition). Commonwealth Printing Press Ltd, Hong Kong

Williams, P. 1991. Tectonic geomorphology, uplift rates and geomorphic response in New Zealand. CATENA 18 p439-452

Williams, P. Dowling, R. 1979. Solution of marble in the karst of the Pikikiruna Range, Northwest Nelson, New Zealand. Earth Surface Processes 4 p15-36

Wilson, C. The 26.5 ka Oruanui eruption, New Zealand: an introduction and overview. Journal of Volcanology and Geothermal Research 112 p133-174

Wopereis, P. 1988. Geology of the Southern Part of Mt. Owen. New Zealand Speleological Bulletin 8/144-145 p134-140

Yokoyama, Y. Reyss, J-L. Guichard, F. 1977. Production of radionuclides by cosmic rays at mountain altitudes. Earth & Planetary Science Letters 36 p44-50